HIGH ORDER PSEUDOHOLOGRAPHY USING ZONE PLATES

J. GUR

REPORT NO. 84
DECEMBER 1978

ABSTRACT

The reconstruction of pseudoholograms at high orders is investigated for the first time. The purpose of the work is to demonstrate the potential and the power of this new technique for obtaining high resolution x-ray images of imploded pellets in laser pellet-compression experiments. Considerable insight, to the high order focusing capability of zone plates, is gained by first studying the analogies between zone plates and diffraction gratings.

The formal mathematical framework of pseudoholography is then rederived, this time including the reconstructions at high orders. Generalized expressions for planar and tomographic resolution, transverse and axial point spread functions are derived. The theoretical study predicts a practical submicron resolution. The limitations and prospects of the technique are discussed, and expressions for determining the effects of diffraction in the recording step of a pseudohologram are derived. Unconventional zone plate designs are introduced and the possible improvement of the high order reconstructions is discussed.

The effects of speckle noise in the high order reconstructions are stutied. The granularity of the film as well as the serration introduced in the zone plate in the manufacturing process are treated. Three computer programs are used to investigate the transverse and axial performance of zone plates of different designs at various orders, and to simulate the recording and reconstruction of a pseudohologram. The dependence of the quality of the high order reconstructions on the object characteristics is demonstrated. By controlling the γ of the

film and the zone plate design, we can optimize the quality of the high order reconstructions of certain classes of objects. The possibility of using different coded apertures when the reconstruction is to be done digitally is discussed.

An optical simulation of imaging an x-ray source is described, which demonstrates the increase of resolution at higher orders. An extensive experimental study is described for investigating the effects of the γ of the recorded pseudohologram and of the imperfections in the zone plate mask on the quality of the reconstructions at high orders. The construction of an x-ray zone plate camera for laser pellet compression measurements is described. Results from some pellet compression experiments are shown demonstrating an increase of resolution at high orders. A resolution test for the zone plate camera is performed. 8μm resolution in the first order and 4μm resolution in the second order are demonstrated. The resolution in the third order is typically 3μm. Finally, an optical simulation of an x-ray experiment is described showing the feasibility of using a one dimensional zone plate coded aperture to spatially resolved spectra.

TABLE OF CONTENTS

TABLE OF CONTENTS, Cont.

TABLE OF CONTENTS, Cont.

TABLE OF CONTENTS, Cont.

TABLE OF CONTENTS, Cont.

LIST OF TABLES

LIST OF FIGURES

LIST OF FIGURES, Cont.

LIST OF FIGURES, Cont.

LIST OF FIGURES, Cont.

LIST OF FIGURES, Cont.

LIST OF APPENDICES

LIST OF SYMBOLS

LIST OF SYMBOLS , Cont.

LIST OF SYMBOLS, Cont.

LIST OF SYMBOLS, Cont.

LIST OF SYMBOLS, Cont.

LIST OF SYMBOLS, Cont.

LIST OF SYMBOLS, Cont.

LIST OF SYMBOLS, Cont.

LIST OF SYMBOLS, Cont.

LIST OF SYMBOLS, Cont.

LIST OF SYMBOLS, Cont.

CHAPTER I

INTRODUCTION

There are two basic approaches to pseudoholography which is frequently called incoherent holography in the literature ([1.1], [1.2], [1.3], [1.4]). In one approach (described in [1.1] and [1.2]) an optical instrument is used to form two images of every point in the object. These two images are coherent with respect to each other, hence they can form interference fringes on a photographic plate. The pseudohologram is thus built up of an incoherent superposition of interference fringes originating from all the points of the object.

In the second approach, which is referred to as coded aperture imaging ([1.5], [1.6], [1.7]), each point in the object casts a shadow of an aperture (a zone plate, an annular aperture, etc.) onto a piece of film (see Fig. 1.1). The pseudohologram in this case is built up of an incoherent superposition of shadows cast by all the points of the object.

In both approaches the object (which is illuminated by an incoherent* source, or is an incoherent source itself such as a plasma or a flame), is considered as a collection of point sources which are incoherent with respect to each other. Furthermore, in both methods the pseudohologram is sensitive to the distance of the object from the aperture, or the appropriate optical instrument, and therefore depth information is recorded as well as intensity information. Both methods are two step procedures in which the second step, the reconstruction step, may be performed either optically or digitally. So

*we will use the term incoherent source although it is rigorously a non physical entity

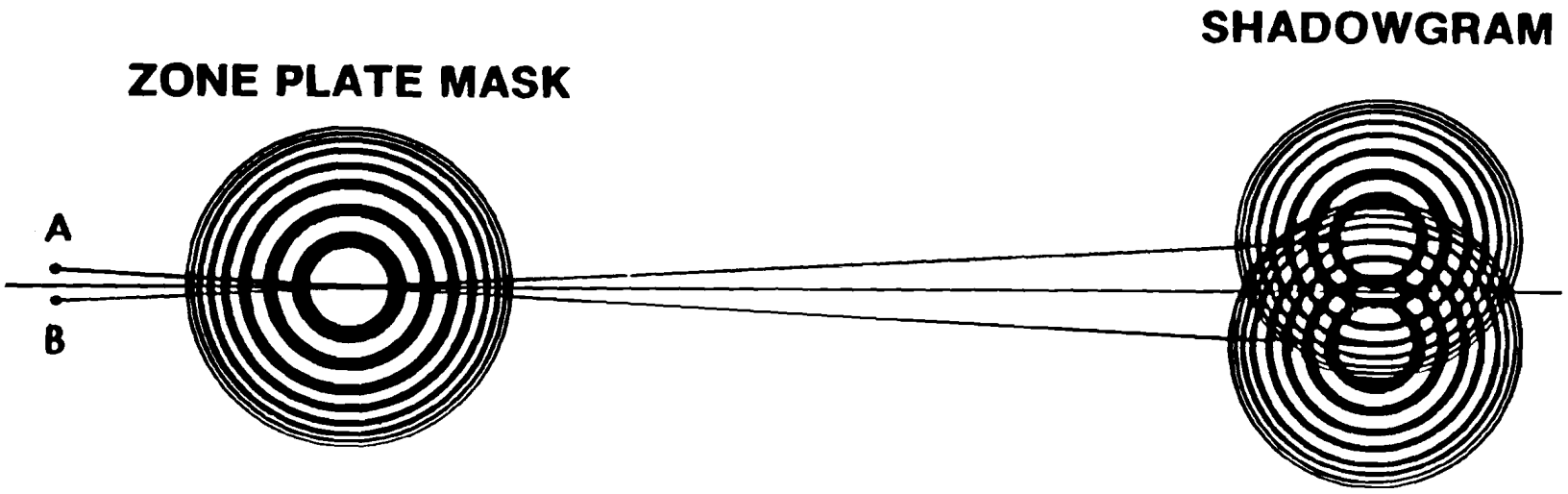

Fig. 1.1
Recording of a shadowgram of two point sources using a zone plate mask.

far, there has not been any practical application using the first method because of the limitation of being able to record only a small number of points. An improvement has been proposed (Ref. [2.2.11]) to increase the number of points considerably using, instead of the usual two beam interferometer, a lensless Fabry Perot interferometer. Further investigations should be carried out in order to determine whether high quality pseudoholograms can be obtained using this method. Since optical elements such as a beam splitter or a Fabry Perot etalon cannot be constructed for the x-ray region this technique is useless for x-ray investigations.

The second method, on the other hand, is not limited to the visible region; in fact, it is most useful in the x-ray region and with nuclear particles where no efficient imaging instrument exists. A useful application of this technique is imaging laser produced plasmas. At the University of Rochester there is a large program devoted to the Laser Fusion Feasibility Project. The experiments reported in this work were performed with a four beam Nd^{+3}:glass laser system (DELTA) that was in operation for four years for the purpose of producing high energy density plasmas by compressing gas filled microballoons. On typical shots, the laser delivered 7-10j on the target and the pulse width was typically 30 picoseconds. When the intense laser light hits the glass shell the surface evaporates immediately and the ablated material speeds outward. The associated reaction force drives the remainder of the shell and the gas fill inward and causes compression.

In proposed laser driven pellet compression experiments using a multibeam multi-kilojoule laser it is anticipated that the dimension of the high temperature compressed core will be of the order of 1μm. Three types of instruments are now being used to get spatial information on the x-ray radiation emitted from the core in such experiments:

(a) The pinhole camera

(b) The x-ray grazing incidence microscope

(c) The Fresnel zone plate.

(a) The pinhole camera (Fig. 1.2) is a standard diagnostic tool in laser produced plasma research because it is simple, insensitive to alignment, has a large field of view, is achromatic and relatively inexpensive. The resolution of the pinhole camera is of the order of the pinhole diameter. 5μm seems to be the smallest practical diameter. For a smaller diameter, in order to employ the pinhole optimally, see Tables 1.1 and 1.2, the pinhole would have to be located so close to the microballoon that it will interfere with the target illumination system. Furthermore, for imaging x-rays, the thickness of the foil, in which the pinhole is made, has to be of the order of 5μm and even thicker for hard x-rays to be sufficiently opaque. For high resolution such pinholes are not planar masks; for example 1μm pinhole in a 5μm thickness sheet of gold would be a very long tunnel, which will cause shadowing and scattering problems.

(b) The grazing incidence x-ray microscope is an extremely expensive instrument. It employs either two orthogonally oriented cylindrical mirrors [1.8] or a system of confocal coaxial ellipsoidal and hyper-

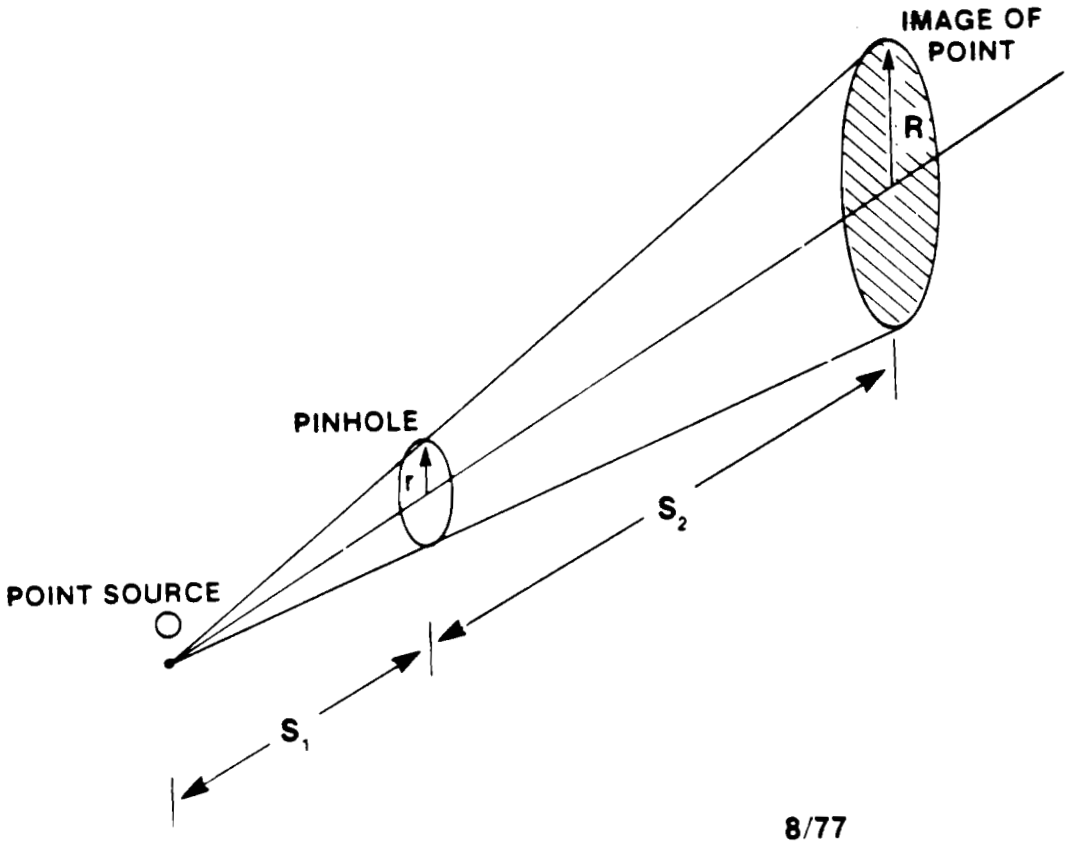

Fig. 1.2
PINHOLE CAMERA GEOMETRY UR LLE

Table 1.1
PINHOLE CAMERA: OPTIMIZATION

(Notation as in Fig. 1.2)
from ref [2.2.7]

$$r_{opt}^2 = 0.9\lambda \left(\frac{S_1 S_2}{S_1 + S_2}\right)$$

R set by resolution of recording medium,

$$R \geq 25\mu m$$

$$\frac{R}{r} \cong \frac{S_2}{S_1} = M, \qquad \text{magnification}$$

$$r_{opt}^2 = 0.9\lambda S_1 \left(\frac{S_2/S_1}{1 + S_2/S_1}\right)$$

$$= 0.9\lambda S_1 \left(\frac{M}{1+M}\right)$$

Typically, M≥5 so

$$S_{1_{opt}} > \frac{r_{opt}^2}{0.9\lambda}$$

Table 1.2

PINHOLE CAMERA : OPTIMIZATION

UR LLE

EXAMPLES :

$\lambda = 6$ Å ($h\nu \sim 2$ KeV)

2r (μm)	10	6	2	1
S_1 (cm)	4.6	1.7	0.2	0.05

$\lambda = 1$ Å ($h\nu \sim 12$ KeV)

2r (μm)	10	6	2	1
S_1 (cm)	25	9.1	1.0	0.25

NOTE : 2r IS APPROXIMATE RESOLUTION IN OBJECT SPACE

boloidal mirrors [1.9]. The resolution of this system seems to be limited by surface roughness. For reflecting surfaces with 50Å rms roughness, calculations show that the resolution is about 1-2μm [1.10]. A practical device [1.10], however, is reported to have 3-5μm resolution. The instrument is also limited to wavelengths >2Å, hence no hard x-ray image or α-particle image can be obtained in this way. The grazing incidence angle is of the order of 1° at this angle the aberrations become so severe that the field of view becomes exceedingly small and the alignment becomes very difficult. A summary of different x-ray grazing incidence microscopes is given in Table 1.3.

(c) The zone plate is being used in two modes of operation: 1. imaging mode and 2. shadowgraphy mode.

1. The imaging mode (see Fig. 1.3).

The zone plate has been used as a focussing device for imaging stellar x-ray sources [1.11]. In Ref. [1.12] a description of the use of a zone plate as an x-ray lens is given. Currently zone plates are made for imaging soft x-rays with resolution of the order of 0.5μm with quasi monochromatic radiation like synchrontron radiation [1.13]. They can be manufactured by an interferometric technique with extremely high number of zones (1000-2000) and can be corrected for spherical aberration by using an aspheric wavefront in the interferometer [1.14]. Furthermore, we do not need to make the zones completely opaque [1.15], because the phase shift introduced by partially transparent metallic zones will always improve image forming efficiency. We can also blaze the zones in an analogous manner to that of a grating, and get high

Table 1.3
STATUS OF GRAZING REFLECTION MICROSCOPES

UR LLE

FOCUSING SYSTEM	LIMITING ABERRATION	PRACTICAL RESOLUTION	PRACTICAL FIELD OF VIEW
ONE MIRROR :			
1. Spherical	Astigmatism	—	—
2 Ellipsoidal (Wolter)	Spherical	10μ x 40μ	—
TWO MIRROR :			
1. Kirkpatrick-Baez	Spherical	3μ	200μ
2. Aspherical (Wolter)	Coma	N.A.	300μ
3. Wolter-Schwarzschild	Field Curvature	N.A.	N.A.
COMPOUND MIRROR :			
1. 3-Mirror	N.A.	N.A.	N.A.
2. 4-Mirror	N.A.	N.A.	N.A.

8/77

$$\phi_{12} - \phi_{11} = \lambda$$

$$\phi_{32} - \phi_{31} = 3\lambda$$

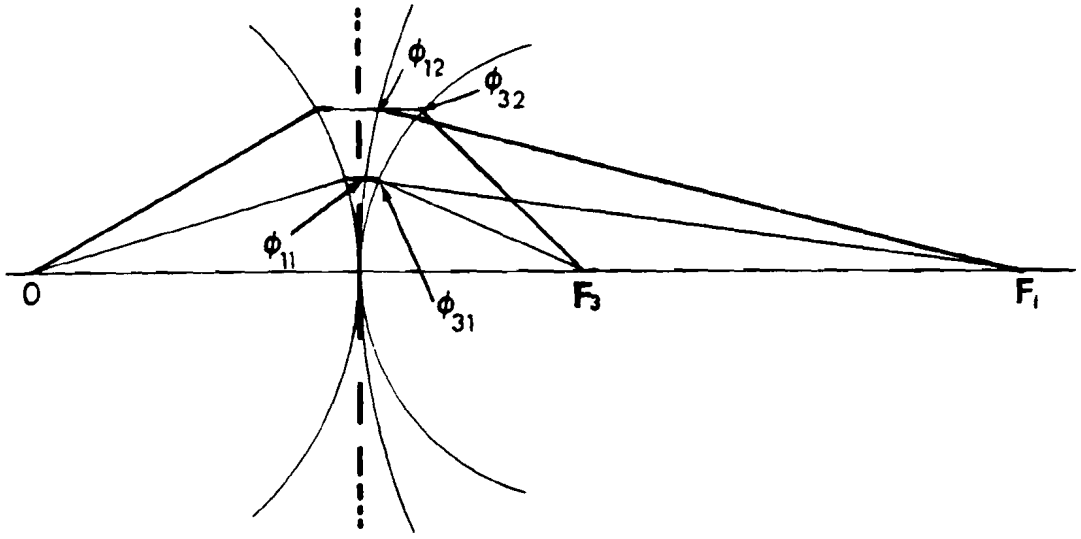

Fig. 1.3

FORMATION OF HIGHER ORDER IMAGES WITH A ZONE PLATE

efficiency at a specific order. Laser produced plasmas emit a broad spectrum; and since the zone plate focal length is inversely proportional to the focal length (as will be discussed later) the dispersion is so great that direct imaging is impractical. In addition, it is not useful for particles or hard x-rays, it is sensitive to alignment and has a limited field of view. In spite of a few claims for improving the resolution in higher order imaging [1.14], [1.16], it will be shown that this is not possible in the imaging mode and the resolution is determined by the width of the outermost zone.

2. Coded aperture mode. Merz [1.19] was the first to use the zone plate in the coded aperture mode for imaging stellar x-ray sources. This technique was then applied to nuclear medicine [1.20] by H. H. Barrett. However, the latter results were not very attractive because the imaged object was too large for the zone plate. (The limit on the object size is of the order of the size of the innermost zone.) Ceglio [1.21] applied this technique to the investigation of laser produced plasmas, the application of concern to us.

In our study we have analyzed various features of coded aperture imaging including the resolving power in higher order reconstructions, and the limitations of the method including grain noise in the film, diffraction effects, and fabrication defects in the zone plate mask. We find that improved resolution is achieved in high order reconstructions, and that contrary to a previous report [1.18] diffraction effects are not, in principle, the limitation in resolution when recording a soft x-ray spectrum.

In Table 1.4 a comparison between all the methods reviewed here

	PINHOLE CAMERA	GRAZING INCIDENCE MICROSCOPE	ZONE PLATE IMAGING	ZONE PLATE PSEUDO-HOLOGRAPHY
Pratical resolution	5μm	3-5μm	0.3μm	1μm
Resolution limited by	Pinhole size	surface roughness	outermost zone	speckle noise
Distance from target	$\lesssim$1 cm	$\gtrsim$10 cm	$\gtrsim$10 cm	$\lesssim$1 cm
Sensitivity to alignment	insensitive	very sensitive	very sensitive	insensitive
Field of view	large (1-3 mm)	small (200μm)	small (200μm)	large (1-3 mm)
Restriction on target diameter	none	$\gtrsim$field of view	$\gtrsim$ field of view	$\geq$innermost zone
Spectral region	$\lambda < 7\text{Å}$; Nuc. rad.	$\lambda > 2\text{Å}$; No nuc. rad.	$\lambda > 1\text{Å}$; No nuc. rad.	$\lambda \leq 7\text{Å}$; Nuc. rad.
Chrom. abberation	none	none	very severe	none
No. of steps in process	real time photog. image	real time photog. image	Real time photog. image	two-step process
Spectral region limited by	diffraction	materials for grazing incidence	manufacturing problems	diffraction
Tomographic capability	none	none	none	moderate tomographic resolution
Cost	$1,000	$250-500 K	$2,000	$2,000

Table 1.4
COMPARISON BETWEEN THE DIFFERENT X-RAY IMAGING TECHNIQUES

is given.

We will first present an analogy between zone plates and gratings. Then the coded imaging technique will be analyzed stressing its potential at higher order reconstructions. Also, the possibility of using different coded apertures when the reconstruction is to be done digitally will be discussed. An optical simulation of imaging an x-ray source is then described, which demonstrates the increase of resolution at higher orders. The construction of an x-ray zone plate camera for laser pellet compression measurements is described. Results from some pellet compression experiments are shown demonstrating an increase of resolution at higher orders. The potential of one dimensional zone plate coded aperture is then discussed. Finally, an optical simulation of an x-ray experiment is described, showing the feasibility of applying the idea to spatially resolved spectra.

1.1 REFERENCES

1.1 G. Cochran, "New Method of Making Fresnel Transformations with Incoherent Light", J. Opt. Soc. Am. 56, 1513 (1966).

1.2 A. W. Lohmann, "Wavefront Reconstruction for Incoherent Objects", J. Opt. Soc. Am. 55, 1555 (1965).

1.3 H. R. Worthington, Jr., "Production of Holograms with Incoherent Illumination", J. Opt.Soc. Am. 56,1937 (1966).

1.4 Tadao Tsuruta, "Holography with Extended Incoherent Source", J. Opt. Soc. Am. 60, 47 (1970).

1.5 H. J. Caulfield and A. D. Williams, "An Introduction to Holography by Shadow Casting", Opt. Eng. 12, 3 (1973).

1.6 H. H. Barrett and D. T. Wilson, G. D. "Fresnel Zone Plate Imaging in Radiology and Nuclear Medicine", Opt. Eng. 12, 8 (1973).

1.7 W. L. Rogers, L. W. Jones, W. H. Beierwalters, "Imaging in Nuclear Medicine with Incoherent Holography", Opt. Eng. 12, 13 (1973).

1.8 F. Seward, J. Dent, M. Boyle, L. Koppel, T. Harper, P. Stoerrmy, and A. Toor, "Calibrated 'Four Color' X-Ray Microscope for Laser Plasma Diagnostics", Sci. Instrum. 47, 464 (1976).

1.9 R. C. Chase, J. K. Silk, "Ellipsoid - Hyperboloid X-Ray Imaging Instrument for Laser Pellet Diagnostics", Appl. Opt. 14, 2094 (1975).

1.10 M. J. Boyle, "Grazing Incidence X-Ray Microscopy of Laser Fusion Targets", SPIE 106 X-Ray Imaging 86 (1977).

1.11 J. H. DijKstra, W. deGraaf and L. J. Lontwaard, "Construction of Apodised Zone Plates for Solar X-Ray Image Formation", in New Techniques in Space Astronomy, ed. F. Labuhn and R. Lust IAU Symposium (Reidel Dordrecht, Netherland) 41, 207 (1971).

1.12 N. M. Ceglio, "Tomography of Laser Fusion Plasmas", 8th International Conference on X-Ray Optics and Microanalysis and 12th Annual Conference of the Microbeam Analysis, Boston, Massachusetts (1977). p. 57A.

1.13 B. Niemann, D. Rudolph and G. Schmahl, "X-Ray Microscopy with Synchrontron Radiation", Appl Opt. 15, 1883 (1976).

1.14 G. Schmahl, D. Rudolf and B. Niemann, "X-Ray Microscopy of Biological Specimens with Zone Plates and Synchrontron Radiation", 8th International Conference on X-Ray Optics and Microanalysis and 12th Annual Conference of Microbeam Analysis, Boston, Mass. (1977). p. 57A.

1.15 J. Kirtz, "Thin Zone Plates for Soft X-Rays", 8th International Conference on X-Ray Optics and Microanalysis and 12th Annual Conference on Microbeam Analysis, Boston, Mass. (1977). p. 59A.

1.16 Germain Boivin, "Use of a Fresnel Zone Plate for Optical Image Formation with Short Wavelength Radiations", Appl Opt. 16, 1071 (1977).

1.17 N. M. Ceglio, "X-Ray Microscopy of Laser Fusion Plasmas Using Coded Imaging Techniques", SPIE 106 X-Ray Imaging 55 (1977).

1.18 N. M. Ceglio, D. T. Atwood and E. V. George, "Zone Plate Coded Imaging of Laser Produced Plasmas", J. Appl. Phys. 48, 1566 (1977).

1.19 L. Mertz and N. O. Young, "Fresnel Transformation of Images", Proc. Int. Conf. on Opt. Instr., London 305 (1961).

1.20 H. H. Barrett, J. Nucl. Med. 13, 382 (1972).

1.21 N. M. Ceglio, "Zone Plate Coded Imaging on a Microscopic Scale", J. Appl. Phys. 48, 1563 (1977).

CHAPTER II

THEORY

2.1 The analogy between zone plates and diffraction gratings.

Consider the system in Fig. 2.1.1. A spherical wave is diffracted by a mask $A(X_o, Y_o)$. Using the Fresnel Kirchhoff integral (see Ref. [2.1.1] page 382) we can write the amplitude at any distance Z from the diffracting aperture. Assuming small angles (less than 30°) we can neglect the obliquity factor in the integral. Also, for a fixed Z the change in $1/r_1$ and $1/r_2$ over the range of integration is negligible compared to the change of the phase, so we replace these terms by the axial values $1/R_1$ and $1/R_2$ of $1/r_1$ and $1/r_2$ respectively and write them outside the integral. The amplitude $G(X_2,Y_2)$ is then:

$$G(X_2, Y_2) = \frac{iC}{\lambda R_1 R_2} \int_{Y_a}^{Y_b} \int_{X_a}^{X_b} A(X_0,Y_0)\, e^{iK(r_1+r_2)}\, dX_0 dY_0 \qquad (2.1.1)$$

where r_1 is the distance between a point on the plane (X_o, Y_o) and a point on the plane (X_1, Y_1), r_2 is the distance between a point on the plane (X_o, Y_o) and a point on the plane (X_1, Y_1), K is the wave number, and C is a constant. Expanding r_1 and r_2 in the exponent we get

$$r_1 \approx R_1 + \frac{1}{2R_1}(X_0 - X_1)^2 + \frac{1}{2R_1}(Y_0 - Y_1)^2 \qquad (2.1.2)$$

$$r_2 \approx R_2 + \frac{1}{2R_2}(X_0 - X_2)^2 + \frac{1}{2R_2}(Y_0 - Y_2)^2 \qquad (2.1.3)$$

Using planar polar coordinates in each of the three planes we have

$$X_0 = \rho a \cos\theta; \quad X_1 = H \cos\alpha; \quad X_2 = \sigma \cos\phi$$

$$Y_0 = \rho a \sin\theta; \quad Y_1 = H \sin\alpha; \quad Y_2 = \sigma \sin\phi \qquad (2.1.4)$$

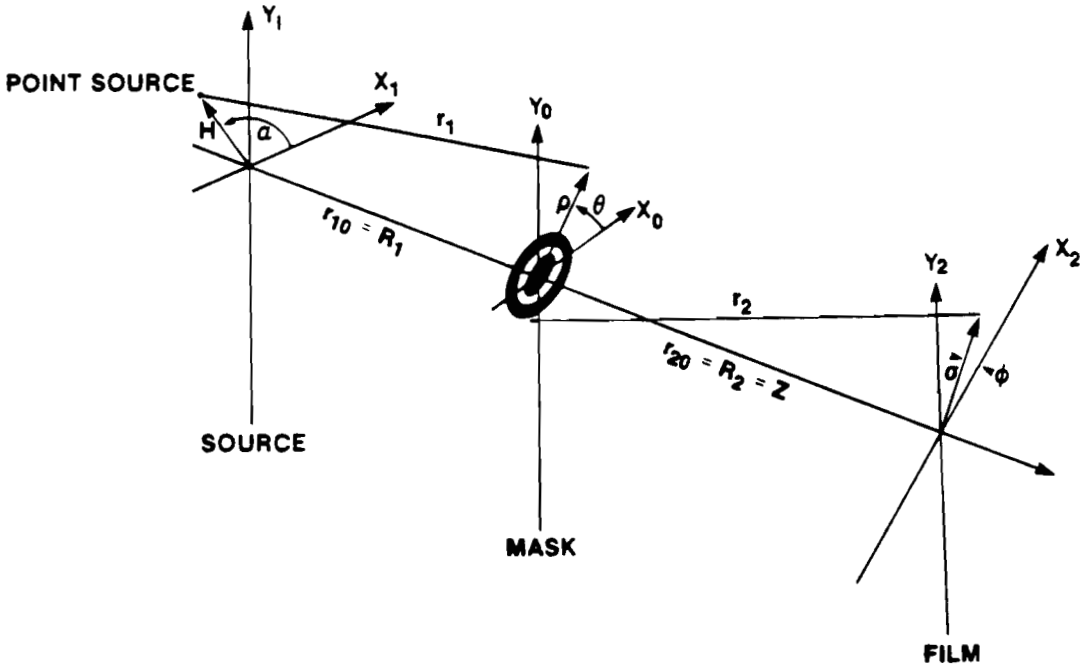

Fig. 2.1.1
Diffraction of a spherical wave through a zone plate.

$$dX_0 dY_0 = a^2 \rho d\rho d\theta; \quad u = \frac{a^2}{2\lambda}\left(\frac{1}{R_1} + \frac{1}{R_2}\right) ,$$

where $(\rho a, \theta)$, (H, α) and (σ, ϕ) are the coordinates in the mask, source and film planes respectively; a is the aperture radius and ρ is the fractional radius. Using (2.1.2), (2.1.3), (2.1.4) in (2.1.1) we get:

$$G(\sigma,\phi) = \frac{iAa^2}{\lambda R_1 R_2} e^{iK(R_1+R_2)} e^{iKH^2/2R_1} e^{iK\sigma^2/2R_2} .$$

(2.1.5)

$$\int_0^{2\pi}\int_0^1 A(\rho)\, e^{2\pi i u\rho^2}\, e^{(-iK\sigma a\rho/R_2)\cos(\theta-\phi) - (iKHa\rho/R_1)\cos(\theta-\alpha)}\, \rho d\theta d\rho .$$

Consider the terms that involve angles:

$$-K\rho a\left\{\frac{\sigma}{R_2}\cos(\theta-\phi) + \frac{H}{R_1}\cos(\theta-\alpha)\right\} = \tag{2.1.6}$$

$$= -K\rho a\left\{\cos\theta\left[\frac{H\cos\alpha}{R_1} + \frac{\sigma\cos\phi}{R_2}\right] + \sin\theta\left[\frac{H\sin\alpha}{R_1} + \frac{\sigma\sin\theta}{R_2}\right]\right\},$$

$$= -K\rho a v\cos(\theta-\chi) ,$$

where

$$\cos\chi = \left[\frac{H\cos\alpha}{R_1} + \frac{\sigma\cos\phi}{R_2}\right]/v , \tag{2.1.7}$$

$$\sin\chi = \left[\frac{H\sin\alpha}{R_2} + \frac{\sigma\sin\phi}{R_2}\right]/v ,$$

$$v^2 = (H/R_1)^2 + (\sigma/R_2)^2 + 2H\sigma/R_1R_2\cos(\phi-\alpha) .$$

Let H/R_1 be the object field angle and σ/R_2 be the image field angle. Let us change variables: $\rho^2 = t$; $\rho d\rho = \frac{1}{2}dt$.

Until now the discussion was general and could be applied to gratings as well as to zone plates. We now limit the discussion to rotationally symmetric apertures, i.e. $A(\rho)$ is rotationally symmetric.

Then $A'(\rho^2) = A(t)$. Using an identity for Bessel functions [2.12] $\frac{1}{2\pi}\int_0^{2\pi} e^{-iK\rho a\, v\cos(\theta-\chi)}\, d\theta = J_0(K\rho av)$, and considering only the integral in Eq. (2.1.5) we get:

$$G'(\sigma,\phi) = \int_0^1 A(t)\, e^{2\pi i t u}\, J_0(v\sqrt{t})\, dt \quad . \qquad (2.1.8)$$

The prime denotes that all the constants were omitted from the formula. Eq. (2.1.8) is the most general expression for the field diffracted from an axially symmetric circular aperture on which a spherical wave of radius R_1 is incident.

Consider the intensity on axis when a point source situated on axis is illuminating a zone plate. In this case $H=\sigma=0$; therefore $v=0$ and $J_0(K\rho av)=1$ and we get from (2.1.8)

$$G'(u) = \int_0^1 A(t)\, e^{2\pi i u t}\, dt \quad . \qquad (2.1.9)$$

This is exactly the Fourier transform of the aperture written in the t-domain rather than in the ρ-domain.

We thus see that the on axis intensity distribution of rotationally

symmetric, two-dimensional, apertures is completely analogous to the far field intensity distribution diffracted by a one-dimensional aperture. Therefore, any result derived in one domain can be immediately transferred to the analogous domain.

We will consider a special class of rotationally symmetric apertures: Fresnel zone plates and a few of their derivatives. The term Fresnel zone plate refers only to a special class of apertures as shown in Fig. 2.1.3. Other general apertures which have some similarities to Fresnel zone plates will simply be called zone plates.

Since we deal with apertures derived from the Fresnel zone plate, let us clarify the notation by first considering Fig. 2.1.2. A cosinusoidal zone plate may be produced by recording the interference from two coherent sources on axis. Let A_1, A_2; ϕ_1, ϕ_2; R_1, R_2 be the amplitudes, phases, and distances of sources 1 and 2, respectively, from the screen, and assume that $A_1/R_1 = A_2/R_2 = A$. Let us use the following definitions: $u = \left(\frac{1}{R_{10}} - \frac{1}{R_{20}}\right)\frac{\pi}{\lambda}$; $\Delta\phi = R_{10} - R_{20} + \phi_1 - \phi_2$; x = distance on the screen. From Fig. 2.1.1 and 2.1.2 we then have

$$I = 2A^2\left[1 + \cos\left(\frac{x^2 u}{4} + \Delta\phi\right)\right] \quad . \tag{2.1.10}$$

In Fig. 2.1.3a Eq. (2.1.10) is plotted for four different source phases. The corresponding Fresnel zone plates that are derived from them are also shown. All plots are in the $\theta = \frac{ux^2}{4}$ coordinate. Zone plates of type (c) and (d) are most commonly employed. (c) is called a positive

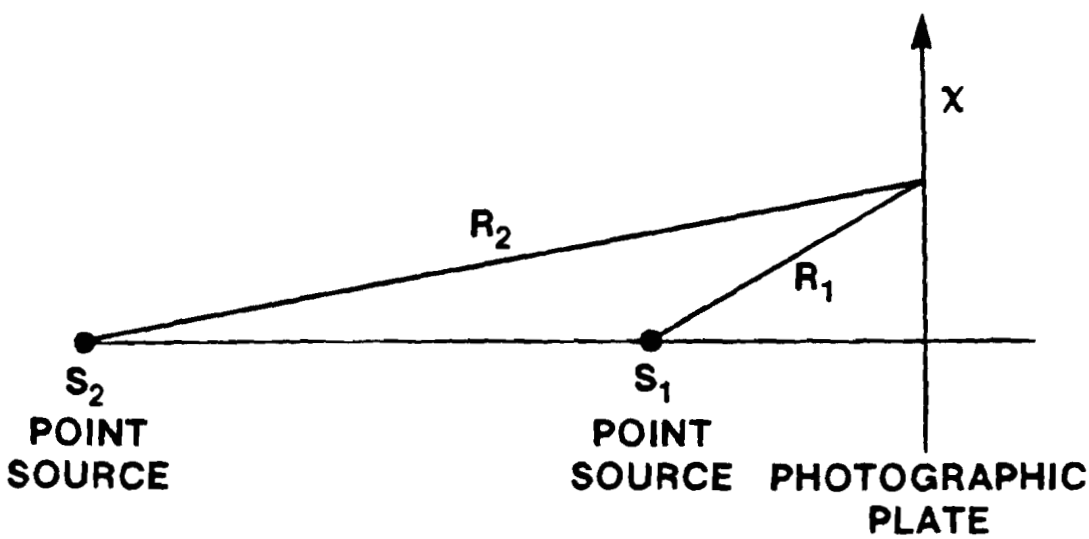

Fig. 2.1.2
Formation of a zone plate by interference of two spherical waves.

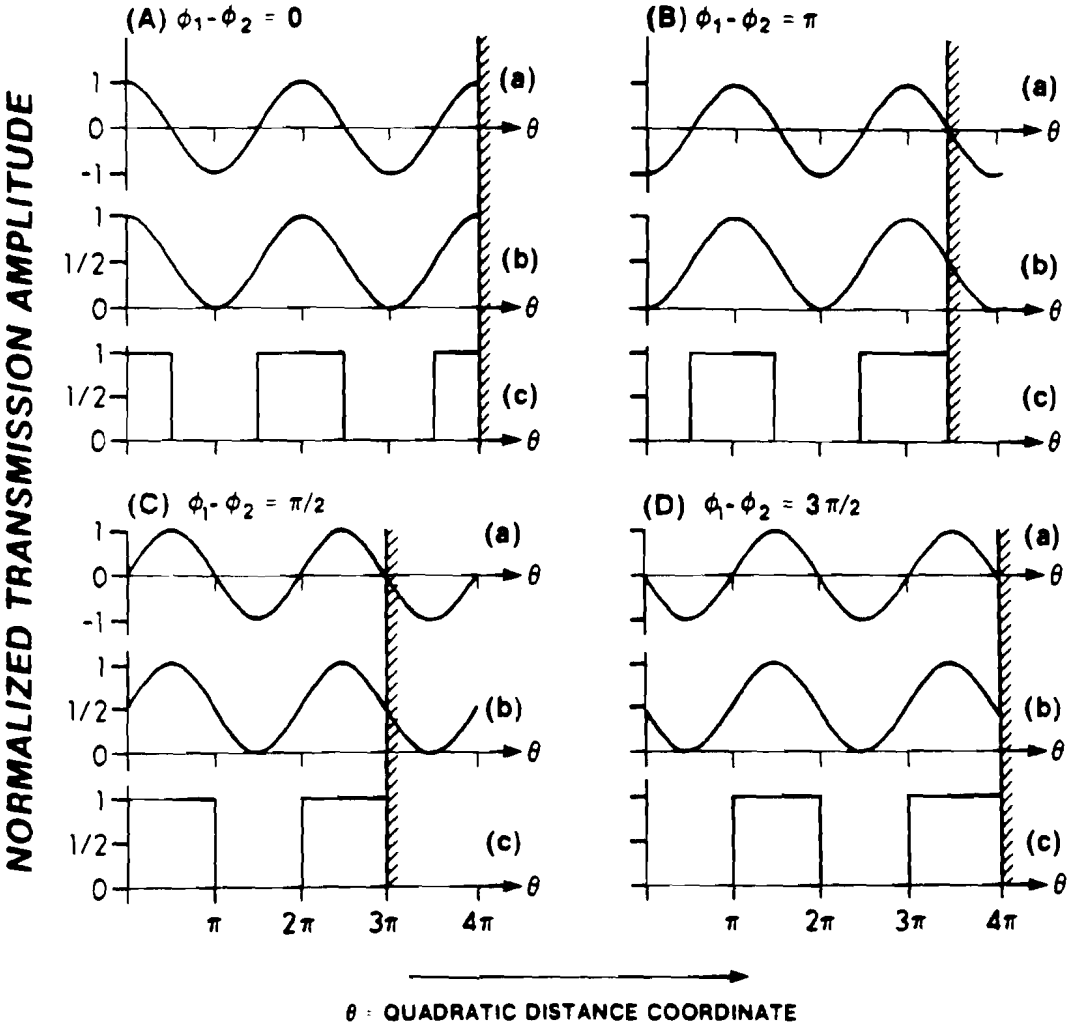

Fig. 2.1.3a
The cosinusoidal zone plates produced by interference of two spherical waves and the corresponding Fresnel zone plates drawn in θdomain. Cases A, B, C,D are phase differences $\phi_1 - \phi_2 = 0, \pi, \pi/2, 3\pi/2$ respectively. For each case (a) represents the cos part of eq. (2.1.10). (b) the intensity in eq. (2.1.10) and (c) the corresponding Fresnel zone plate. Case C is the positive Fresnel zone plate. Case D is the negative Fresnel zone plate.

zone plate and (d) is called a negative zone plate. (They differ by a phase of π.) In Fig. 2.1.3 b positive zone plates in real space are shown. From Fig. 2.1.3 a we see that positive zone plates always have an odd number of zones (transparent and opaque). The number of open zones exceeds by one the number of opaque zones. The negative zone plate has an even number of zones.

In Table 2.1.1 (1) we list the location of the zone edges (in the θ-coordinate for the four cases in Fig. 2.1.3 a. In (2) we list the boundaries of the open zone in each case. Finally we generalize in (5) these expressions in order to obtain an expression for an arbitrary zone plate width and shape. From Table 2.1.1 it is possible to write an expression from which all the four cases in Table 2.1.1 can be derived. The range of θ that belongs to the j^{th} open zone denoted by θ_j is:

$$(2j - \tfrac{1}{2})\pi + \Delta\phi \leq \theta_j \leq (2j + \tfrac{1}{2})\pi + \Delta\phi \qquad (2.1.11)$$

where $\Delta\phi = \phi_1 - \phi_2 = (0, \pi, \pi/2, 3\pi/2)$ according to Fig. 2.1.3 a. In a computer calculation of the diffracted intensity distributions from various zone plates we find it convenient to define RPEVEN, RPODD; RNEVEN, RNODD to be the radii of an even numbered or an odd numbered zone edge respectively in a positive or negative zone plate respectively, and EPS1 and EPS2 to be the fractional width of the zone plates as in Fig. 2.1.4 b. Q is the zone plate constant (i.e. $Q = 1/\sqrt{NZONE}$), and NZONE is the total number of zones. Using these definitions and Table 2.1.1 we can write the following results:

1. Positive zone plate (NZONE = odd number; open center)

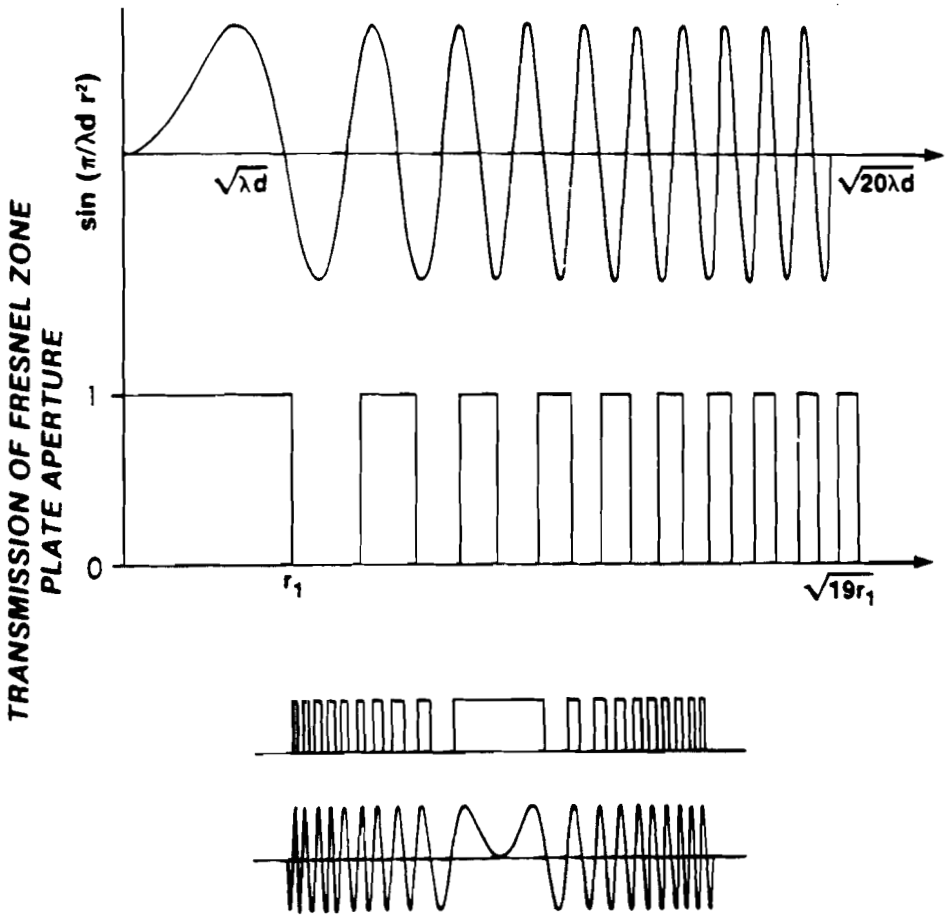

Fig. 2.1.3b
Cosinusoidal zone plates and Fresnel zone plates drawn in real space coordinate.

Table 2.1.1: Notation for Fresnel Zone Plates

Number	Zone Plate Edge Locations	Zone Plate Type (according to Fig. 2.1.3a) A	B	C	D
		$\phi_1 - \phi_2 = 0$	$\phi_1 - \phi_2 = \pi$	$\phi_1 - \phi_2 = \frac{\pi}{2}$	$\phi_1 - \phi_2 = \frac{3\pi}{2}$
	θ_0	0	$\pi/2$	0	π
	θ_1	$\pi/2$	$3\pi/2$	π	2π
(1)	θ_2	$3\pi/2$	$5\pi/2$	2π	3π
	θ_3	$5\pi/2$	$7\pi/2$	3π	4π
	θ_4	$7\pi/2$		4π	
	Open Zone Boundaries				
	$j = 0$	$0 \rightarrow \pi/2$	$\pi/2 \rightarrow 3\pi/2$	$0 \rightarrow \pi$	$\pi \rightarrow 2\pi$
(2)	$j = 1$	$3\pi/2 \rightarrow 5\pi/2$	$5\pi/2 \rightarrow 7\pi/2$	$2\pi \rightarrow 3\pi$	$3\pi \rightarrow 4\pi$
	$j = 2$	$7\pi/2 \rightarrow 8\pi/2$			
(3)	General Form for Zone Boundaries	$(2j-\frac{1}{2})\pi \rightarrow (2j+\frac{1}{2})\pi$	$(2j+\frac{1}{2})\pi \rightarrow (2j+\frac{3}{2})\pi$	$2j\pi \rightarrow (2j+1)\pi$	$(2j+1)\pi \rightarrow 2(j+1)\pi$

Table 2.1.1: Continued

Number	Comments	Zone Plate Type (according to Fig. 2.1.3a) A	B	C	D
(4)	Equivalent Form	- - -	- - -	$\frac{4j\pi}{2} \rightarrow \frac{2(2j+1)\pi}{2}$	$\frac{2(2j+1)\pi}{2} \rightarrow \frac{4(j+1)\pi}{2}$
(5)	Final Form	- - -	- - -	$\left(\frac{4j+1}{2} - \frac{1}{2}\right)\pi \rightarrow \left(\frac{4j+1}{2} + \frac{1}{2}\right)\pi$	$\left(\frac{4j+3}{2} - \frac{1}{2}\right)\pi \rightarrow \left(\frac{4j+3}{2} + \frac{1}{2}\right)\pi$
(6)	Location of Zone Centers	- - -	- - -	$\frac{(4j+1)}{2}\pi$	$\frac{(4j+3)}{2}\pi$

$$RPEVEN = [(4M+1)/2 - EPS1]^{\frac{1}{2}}Q; \quad RPODD = [(4M+1)/2 + EPS2]^{\frac{1}{2}}Q \qquad (2.1.12)$$

where $M = 0, \ldots, (NZONE-1)/2$

2. Negative zone plate (NZONE = even number; opaque center)

$$RNODD = [(4M+3)/2 - EPS1]^{\frac{1}{2}}Q; \quad RNEVEN = [(4M+3)/2 + EPS2]^{\frac{1}{2}}Q \qquad (2.1.13)$$

where EPS1, EPS2 $\leq$ 0.5 but for a Fresnel zone plate EPS1 = EPS2 = 0.5.

As an example we calculate (2.1.9) for a positive zone plate. Since the equation is in the form of a Fourier transform, we may consider the analogous case of the Fraunhofer diffraction pattern of a grating. We derive it explicitly because of misleading results in the literature 2.1.4 , [2.1.5], [2.1.6] and [2.1.7]. Denote by N the total number of zones (both clear and opaque) From (2.1.9) we have:

$$G'(u) = \int_{-\infty}^{\infty} \sum_n \delta(t - 2nq - \frac{q}{2}) * \text{Rect}[t;q]\ e^{2\pi iut}\, dt \quad . \qquad (2.1.14)$$

Using the convolution theorem and the fact that

$$\int_{-\infty}^{\infty} \text{Rect}[t;q]\ e^{2\pi iut}\, dt = \frac{\sin \pi uq}{\pi u}$$

we have:

$$G'(u) = e^{2\pi i(uq/2)} \sum_{n=0}^{(N-1)/2} e^{2\pi i 2nqu} \frac{\sin \pi uq}{\pi u} \quad , \quad (2.1.15a)$$

or

$$G'(u) = e^{\pi i Nqu} \frac{\sin[\pi uq(N+1)]}{\sin(2\pi qu)} \frac{\sin[\pi uq]}{\pi u} \quad . \quad (2.1.15b)$$

From (2.1.15 b) and (2.1.5) we get for the amplitude (neglecting the phase factors):

$$G''(u) = \frac{1}{2\lambda R_1 R_2} \frac{\pi A a^2}{} \frac{\sin[\pi qu(N+1)]}{2\cos(\pi qu)} \frac{1}{\pi u} \quad . \quad (2.1.15c)$$

Assume $R_1 \to \infty$ (collimated light); $A/R_1 \to E$ = constant. Substituting for u from (2.1.4) into (2.1.15 c) we have the remarkable result:

$$G''(u) = \frac{E}{2} \frac{\sin[\pi qu(N+1)]}{\cos(\pi qu)} \quad . \quad (2.1.16)$$

From 2.1.16 it is obvious that all the foci have the same peak on-axis intensity. The locations of the foci are found by taking the limit of (2.1.16) as $\cos(\pi qu) \to 0$, or $u \to (2\ell+1)\frac{1}{2q}$ and by using (2.1.4) for u the locations will be found later. Substituting for u we get the limit:

$$\lim_{u \to (2\ell+1)1/2q} \frac{\sin[\pi qu(N+1)]}{\cos(\pi qu)} = \frac{(N+1)}{2} (-1)^{\ell-1} \quad . \quad (2.1.17)$$

From (2.1.5) and (2.1.7) we write the total phase function using $R_1 \to \infty$ and $\sigma = 0$ as: $\phi = \frac{\pi}{2} + KR_{20} - \frac{\pi(N+1)}{2} - \pi\ell$. Hence successive odd order foci have successive phase changes of π. (Not including the phase due to distance KR_{20}.) From $\pi q u = (a\ell+1)\frac{\pi}{2}$, $u = \frac{a^2}{2\lambda R_2}$ and $q = \frac{1}{N}$ we get, denoting the order number by p, the locations of the foci:

$$R_2 = \frac{a^2}{N\lambda}\frac{1}{p} = \frac{F}{p} \qquad . \qquad (2.1.18)$$

Let us explore more specific examples of the analogy between zone plates and gratings.

2.1.1 Spread of the principal orders.

Eq. (2.1.15 b) is the formula for the on-axis intensity of a zone plate but it is also the expression of the intensity in the Fraunhofer plane of a diffraction grating. The only difference is the coordinate u. In the zone plate case, $u = a^2/2\lambda R_2$ while in the grating case, $u = (dx/2\lambda R_2)\frac{1}{q}$ where X is the distance on a transverse plane; d is the slit size width; $q = \frac{1}{N}$. For a given N the spread of the principal orders is constant in the u domain. This is true in the grating case and also in the zone plate case in u domain. However it is not true for zone plates in real domain where, as we go to higher orders, the spread on axis gets smaller. From (2.1.15 b), using the two definitions of u, we get the spread of principal orders (using small angle approximations).

For ruled gratings: $\Delta X = \frac{\lambda Z}{Nd}$

For zone plates: $\Delta R_2 = \frac{\lambda}{\frac{(N+1)}{2}} \frac{R_2^2}{qa^2}$

2.1.2 Chromatic Resolving Power.

Both gratings and zone plates can be used as spectrometers. While the dispersion in gratings occurs in transverse plane, a zone plate can be used as an axial spectrometer. In both cases the important quantity is the chromatic resolving power. From Ref. [2.1.1] p.106 (let M be the order number) we have for gratings that

$$\frac{\Delta\lambda}{\lambda} = \frac{1}{NM} \tag{2.1.19a}$$

The same calculation for a zone plate gives

$$\frac{\Delta\lambda}{\lambda} = \frac{1}{\frac{(N+2)}{2}(2\ell+1)} \tag{2.1.19b}$$

which is analogous to (2.1.19a).

2.1.3 Dispersion.

In a grating the dispersion along a one-dimensional coordinate X is given in Ref. [2.1.1]. p.106:

$$\Delta X = \frac{Z\Delta\lambda}{Nd}$$

In a zone plate the dispersion along the optical axis is:

$$\Delta R_2 = R_2^2/qa^2 \cdot \Delta\lambda/\frac{(N+1)}{2}$$

or

$$\frac{\Delta R_2}{R_2} = \frac{\Delta\lambda}{\lambda}$$

Hence, if we want to use the zone plate in the imaging mode only,

quasimonochromatic radiation must be used.

2.1.4 Illumination with a Finite Source.

Assume at first that the source is planar and perpendicular to the optical axis. Spherical waves from different points are incident on a grating at different angles and give rise to grating patterns slightly displaced with respect to each other. Note that this is true either in the Fraunhofer plane or at the image plane of the point source when a lens is used . Thus if the source is incoherent then the diffraction pattern will be a convolution of the source with the diffraction pattern produced by collimated light. The direct analog in a zone plate will be a longitudinal line source. The convolution is exact in 1/z coordinates but in z coordinates the axial spread of higher orders will shrink. A transverse source, however, will be imaged to a transverse source as with a lens.

2.1.5 The Effects of Changing the Zone Shape or the Slit Shape.

For this discussion we will work with the analogy between amplitude gratings and zone plates. In Fig. 2.1.4 a few examples of different zone plates are shown. We can describe the on-axis intensity distributions using the same procedures as before. Let $B_a(t)$ be the individual amplitude slit shape (or the zone shape in the r^2 domain). The aperture function of the grating (or the zone plate) can then be written:

$$A(t) = \sum_n \delta(t - 2nq - \frac{q}{2}) \cdot \mathrm{Rect}\left[t - \frac{qN}{2}; \frac{Nq}{2}\right] * B_a(t) \quad . \quad (2.1.20)$$

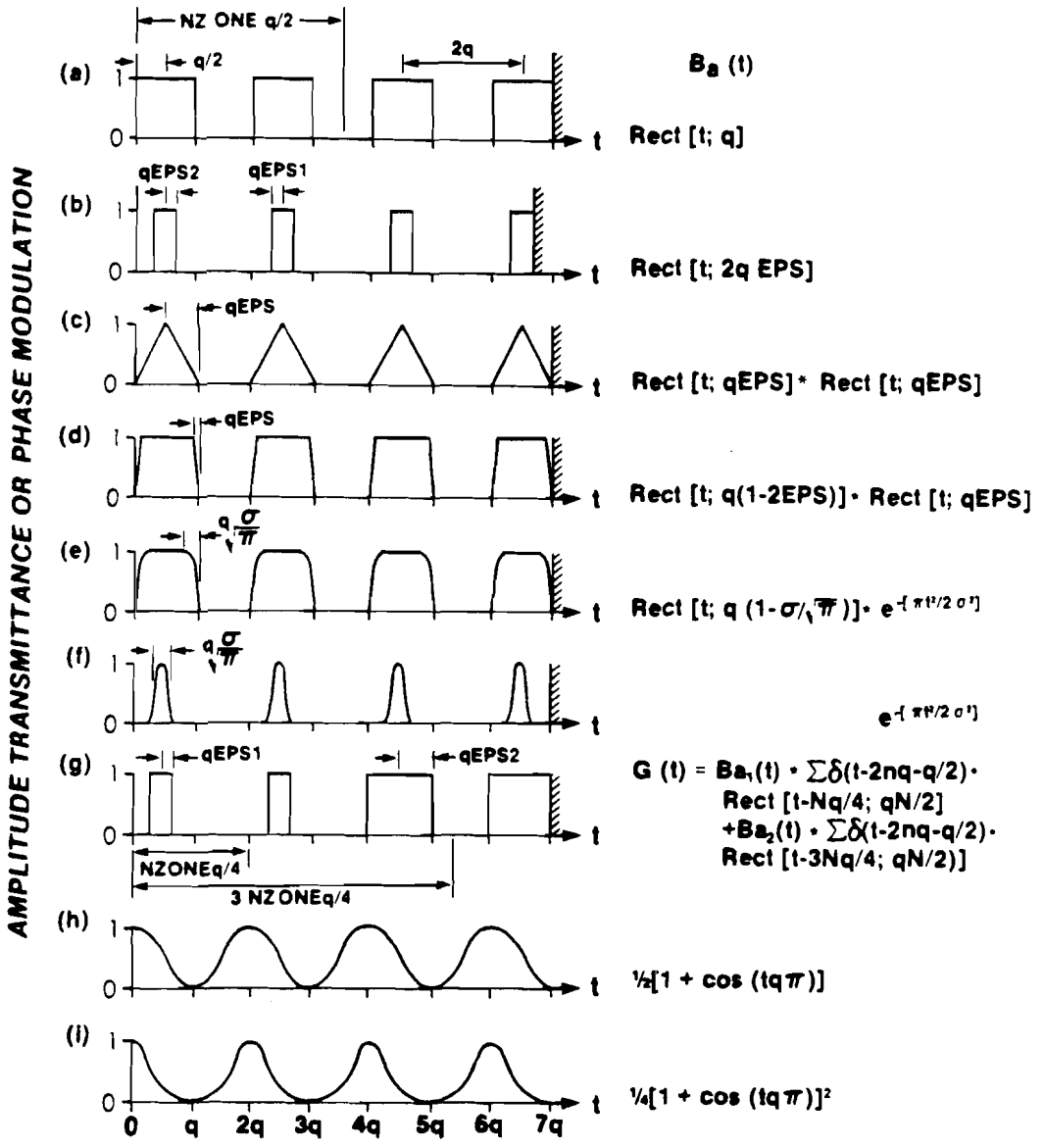

Fig. 2.1.4
Amplitude transmission or phase modulation of zone plates (t = distance square coordinate), or of amplitude or phase gratings (t = real distance coordinate). (a) Fresnel zone plate (positive), (b) zone plate with narrow zones, (c) triangular zones, (d) zone plate with slanted edges, (e) edges smoothed with a Gaussian function, (f) narrow Gaussion zones, (g) zone plate with two different zone widths, (h) cosinusoidal zone plate, (i) cosinusoidal zone plate recorded with $\gamma = 2$.

Neglecting constants and phases, the diffraction pattern is, therefore:

$$G(u) = \frac{\sin[\pi qu(N+1)]}{\sin[\pi qu]} \cdot \tilde{B}_a(u) \quad . \quad (2.1.21)$$

The $\tilde{B}_a(u)$ and the corresponding G(u) are calculated in Table 2.1.2. There are two methods of normalization. In the first we normalize the intensity of the diffraction pattern with respect to the zero order. This is a useful procedure when the energy diffracted in the zero order is measurable as in the case of amplitude zone plates illuminated with collimated light. However the zero order can be eliminated in phase gratings, and in the case of zone plates illuminated with a collimated beam, the energy in the zero order is not focussable. In these cases we normalize the diffracted intensity with respect to the first order. Examples of a few normalized expressions are given in Table 2.1.3.

2.1.6 Conclusions from the Calculations of the Diffraction Patterns for Gratings and Zone Plates (Fig. 2.1.4 and Table 2.1.2).

1. The on-axis intensity in higher orders in zone plates, depends strongly upon the shape of the individual zones.

2. It is not possible to eliminate the zero order with only an amplitude modulation in the grating. The presence of the zero order causes background problems both when imaging with zone plates and in reconstruction in pseudoholography.

3. If the zone plates have very sharp edges, as in Fig. 2.1.4.a, the peak on-axis intensity will stay the same at all odd orders. If the zones are made narrower as in Fig. 2.1.4 b even numbered foci

Table 2.1.2: Fraunhofer Diffraction Patterns of Gratings and On-Axis Amplitudes of Zone Plates (Neglecting the phase factors)

# from Fig. 2.1.4	$\tilde{B}_a(u)$	$G(u)$
4a	$\frac{\sin(\pi uq)}{\pi u}$	$\frac{iE\,\sin[\pi uq(N+1)]}{\sin[\pi uq]} \cdot \sin(\pi uq)$
4b	$\frac{\sin(\pi uq2EPS)}{\pi u}$	$\frac{iE\,\sin[\pi uq(N+1)]}{\sin[\pi uq2]} \cdot \sin(\pi uq2EPS)$
4c	$\frac{\sin^2(\pi uqEPS)}{(\pi u)^2}$	$\frac{iE\,\sin[\pi uq(N+1)]}{\sin[\pi uq2]} \cdot \frac{\sin^2(\pi uqEPS)}{\pi u}$
4d	$\frac{\sin[\pi uq(\frac{1-2EPS}{2})]}{\pi u} \cdot \frac{\sin(\pi uqEPS)}{\pi u}$	$\frac{iE\,\sin[\pi uq(N+1)]}{\sin[\pi uq2]} \cdot \sin[\pi uq(\frac{1-2EPS}{2})] \cdot \frac{\sin(\pi uqEPS)}{\pi u}$
4e	$\frac{\sin[\pi uq(1-\frac{\sigma}{\sqrt{\pi}})](\sqrt{2}\,\sigma)\exp[-2\pi\sigma^2u^2]}{\pi u}$	$\frac{iE\,\sin[\pi uq(N+1)]}{\sin[\pi uq2]} \cdot \sin[\pi uq(1-\frac{\sigma}{\sqrt{\pi}})](\sqrt{2}\,\sigma)\exp[-2\pi\sigma^2u^2]$
4f	$\sqrt{2}\,\sigma\,\exp[-2\pi\sigma^2u^2]$	$\frac{iE\,\sin[\pi uq(N+1)]}{\sin[\pi uq2]} \cdot u\sqrt{2}\,\sigma\,\exp[-2\pi\sigma^2u^2]$
4g		$\frac{iE\,\sin[\pi uq(\frac{N+1}{2})]}{\sin[\pi uq2]} \cdot ue^{i\phi}[\tilde{B}_{a_1}(u) + \tilde{B}_{a_2}(u)e^{i(\phi_2-\phi_1)}]$
4h		$iE\;u\{\delta(u) + \frac{1}{2}\delta(u-\frac{q}{2}) + \frac{1}{2}\delta(u+\frac{q}{2})\}$
4i		$iE\;u\{\frac{3}{2}\delta(u) + \delta(u-\frac{q}{2}) + \frac{1}{4}\delta(u-q) + \frac{1}{4}\delta(u+q)\}$

Table 2.1.3: Normalization for Zone Plates and Gratings

# from Fig. 2.1.4	Normalization (Grating Case) $\frac{G(u)}{G(0)}$	Normalization (Zone Plates Case) $\frac{G(u)}{G(1/2q)}$
4a	$\frac{2}{(N+1)} \frac{\sin[\pi uq(N+1)]}{\sin[\pi uq2]} \frac{\sin(\pi uq)}{(\pi uq)}$	$\frac{2}{(N+1)} \frac{\sin[\pi uq(N+1)]}{\sin[\pi uq2]} \cdot \sin(\pi uq)$
4b	$\frac{2}{(N+1)} \frac{\sin[\pi uq(N+1)]}{\sin[\pi uq2]} \frac{\sin[\pi uq2EPS]}{(\pi uq2EPS)}$	$\frac{2}{(N+1)} \frac{\sin[\pi uq(N+1)]}{\sin[\pi uq2]} \cdot \frac{\sin[\pi uq2EPS]}{\sin(\pi EPS)}$
4c	$\frac{2}{(N+1)} \frac{\sin[\pi uq(N+1)]}{\sin[\pi uq2]} \frac{\sin^2[\pi uqEPS]}{(\pi uqEPS)^2}$	$\frac{2}{(N+1)} \frac{\sin[\pi uq(N+1)]}{\sin[\pi uq2]} \cdot \frac{\sin^2[\pi uqEPS]}{\sin^2(\pi EPS)} \cdot \frac{1}{(qu2)}$
4d	$\frac{2}{(N+1)} \frac{\sin[\pi uq(N+1)]}{\sin[\pi uq2]} \frac{\sin[\pi uq(\frac{1-EPS}{2})]}{[\pi uq(\frac{1-EPS}{2})]} \cdot \frac{\sin[\pi uqEPS]}{(\pi uqEPS)}$	$\frac{2}{(N+1)} \frac{\sin[\pi uq(N+1)]}{\sin[\pi uq2]} \cdot \frac{\sin[\pi uq(\frac{1-EPS}{2})]}{\sin[\pi(\frac{1-EPS}{4})]} \cdot \frac{\sin[\pi uqEPS]}{\sin[\pi EPS]} \cdot \frac{1}{(uq2)}$
4e	$\frac{2}{(N+1)} \frac{\sin[\pi uq(N+1)]}{\sin[\pi uq2]} \frac{\sin[\pi uq(1-\frac{\sigma}{\sqrt{\pi}})]}{[\pi uq(1-\frac{\sigma}{\sqrt{\pi}})]} \cdot e^{-[2\pi\sigma^2u^2]}$	$\frac{2}{(N+1)} \frac{\sin[\pi uq(N+1)]}{\sin[\pi uq2]} \cdot \frac{\sin[\pi uq(1-\frac{\sigma}{\sqrt{\pi}})]}{\sin[\frac{\pi}{2}(1-\frac{\sigma}{\sqrt{\pi}})]} \cdot e^{[-(2\pi\sigma^2u^2 - \frac{\pi\sigma^2}{2q^2})]}$
4f	$\frac{2}{(N+1)} \frac{\sin[\pi uq(N+1)]}{\sin[\pi uq2]} e^{-[2\pi\sigma^2u^2]}$	$\frac{2}{(N+1)} \frac{\sin[\pi uq(N+1)]}{\sin[\pi uq2]} (\frac{\sigma}{q}) e^{[-(2\pi\sigma^2u^2 - \frac{\pi\sigma^2}{2q^2})]}$

appear. Some high even and odd orders may also have a peak intensity corresponding to the ideal case EPS=0.5 depending on the number EPS (see Table 2.1.2.4b).

4. Smoothing of the edges tends to decrease the efficiency at higher orders. For a triangular zone shape (Fig. 2.1.4.c, 2.1.4.d) the decrease is the worst of the examples picked. In case of a Gaussian shape, the decrease is less severe (Fig. 2.1.4.e, 2.1.4.f). There may even be an increase in on-axis intesity at higher orders as may be seen by substituting for in Table 2.1.2.4f the value 1/N where N is the number of zones.

5. Processing the original recording with $\gamma \neq 1$ changes the apparent shape of the zones. Therefore, the efficiency at higher orders depends very much on the type of processing. Processing may also cause artifacts in pseudoholography as will be discussed later on.

6. Because of the finite dynamic range of the recording medium it is preferable to use zone plates with narrow zones, (as will be seen later on) therefore a zone plate as in Fig. 2.1.4.g seems attractive. The inner zones are much narrower compared to their usual width. This, in addition, will tend to increase the light scattered into higher orders.

7. If the amplitude modulation in the grating is an exact $\cos^2$ function $A\cos^2 = A/2(1+\cos 2\ )$ then only $0, \pm 1$ orders appear and in the case of zone plates only one real focus exists.

2.1.7 Phase Gratings and Zone Plates.

In this case there are two modes of operation: (1) transmission, where changes in index of refraction cause diffraction, and (2) reflection, where the relief structure on the surface causes the diffraction. The sinusoidal phase grating was analyzed by Goodman [2.1.2].

In Fig. 2.1.4 a few other examples are listed. Only the sinusoidal example has a simple closed form solution, the others are extremely involved. Kirtz [2.1.8] has calculated a general expression for the example 2.1.4 d (where the vertical axis is now phase). His treatment includes absorption effects as well. He mentioned only zone plates but all his results apply equally well to gratings. Also, he assumes working only in transmission (the analog being transmission gratings).

However, in Ref. [2.1.9] and [2.1.10] the efficiency of reflection gratings is considered with different groove shapes. These results can be applied directly to zone plates working in the reflection mode.

Bleaching of pseudoholograms may be a useful technique to enhance higher order reconstruction. Also reconstruction in reflection should be investigated both with and without aluminum coating on the processed pseudohologram. Coating with Ag or Al will enhance the surface structure while reconstruction without a coating will take advantage of volume effects as well. Using zone plates in reflection introduces new problems such as polarization effects. These were not treated before because the usual use of zone plates was in the transmission mode on axis. This mode of operation may provide an easier way to blaze the pseudohologram to achieve high efficiency at high orders.

The main advantage of phase gratings (or zone plates) over the amplitude counterpart is the possibility of conveniently eliminating the zero order and hence increasing the signal to noise ratio, both in imaging applications as well as with the reconstruction of pseudo-holograms. As an example, consider a phase grating or zone plate of the type shown in Fig. 2.1.4 a. Calculating the $\tilde{B}_p(u)$ which corresponds to $\tilde{B}_a(u)$ in Eq. (2.1.20) and Table 2.1.1, we get:

$$\tilde{B}_p(u) = \int_{-q}^{0} e^{i\phi}\, dt + \int_{0}^{q} dt = q(e^{i\phi} + 1)$$

This will determine the efficiencies at all the orders as we have seen in section 2.1.4. The condition for $\tilde{B}_p(0)=0$ is that $\phi=\pi$. Fig. 2.1.4 a shows this blazed phase grating (when $\phi = \pi$) in which the zero order is eliminated and higher orders are more intense on-axis.

In Fig. 2.1.5 we see the condition for blazing a transmission zone plate for a specific order in analogy with blazed reflecting gratings. In practice we may control the phase modulation by the exposure in the case of reconstructing a pseudohologram. Also, by controlling the magnification of the pseudohologram we may find the right focal length that exactly matches the given modulation to obtain blazing. This technique is completely analogous to gratings and has been used so far only in the far infrared regions [2.1.11 a]. A group at Lawrence Livermore Laboratory has recently announced [2.1.11 b] its intention to blaze zone plates for the x-ray region for use in the imaging mode.

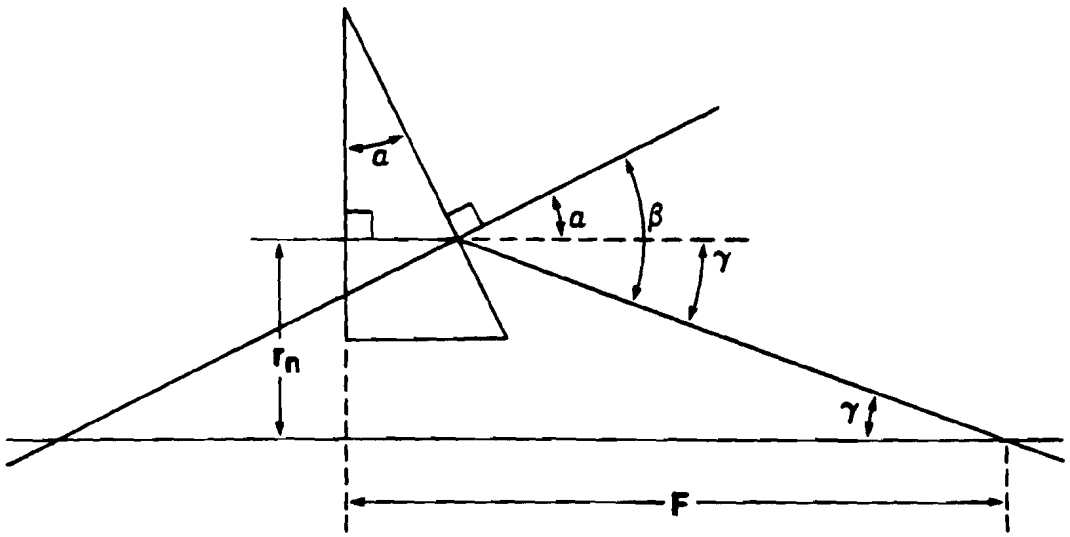

Fig. 2.1.5
Blazing of the zone plate occurs when both the diffracted and the refracted beams have the same direction, in complete analogy with diffraction gratings. r_n is the nth radius of the zone plate. F is the focal length where the zone plate is blazed. If n_2 is the refractive index of the material of which the zone plate is made, $n_2 \sin\alpha = \sin\beta$.

2.1.8 Fluxes at Higher Orders.

For the example in Fig. 2.1.4.a we have seen that the peak on-axis intensity is the same at all the odd numbered foci. At high orders we approach closer to the zone plate and have a larger cone angle of illumination. This means that incident collimated light will be focussed to a smaller Airy disc. If Ω_1 is the cone angle at the primary focus, $p\Omega_1$ is the cone angle at focus number p. The area of the Airy disc is then $\frac{S_1}{p^2}$ where S_1 is the area of the Airy disc at the primary focus. Since the peak intensities are equal but the areas are related as $1:p^2$, the number of scattered photons must also be related as $1:p^2$.

2.1.9 Scattering and Noise in Gratings and Zone Plates.

We may distinguish between two kinds of scattering which lead to speckle patterns in the reconstruction of a pseudohologram and to background noise in case of imaging an incoherent source. In the case of a pseudohologram which is recorded on film, the film grains will cause a speckle pattern when we illuminate with coherent light exactly in the same way as a ground glass produces speckle when illuminated with laser light. This can be treated as a Gaussian random process for which a fairly large literature exists [2.1.12].

The second source of scattering is the zone edges which are not ideally smooth but are really serrated apertures. Little has been done concerning the diffraction pattern of such apertures. (See a recent paper Ref. [2.1.13].) The mathematics becomes exceedingly involved because symmetry is destroyed, and the formalism employed before cannot be used.

If we consider one-dimensional gratings as shown in Fig. 2.1.6, the grain noise contribution can be seen but the serration is not easily visualized. In order to include the serration contribution to the one-dimensional model, we have to consider an ensemble of one-dimensional zone plates (or gratings) with grooves that vary randomly.

To make such a treatment we let $r_n = r_n^o + \delta_n(r_n)$; r_n is the radius of a certain zone r_n^o is the radius of an ideally smooth zone; $\delta_n(r_n)$ is a random variable. In general, if the aperture function for one member of the ensemble is $Z(t)$, and that for the ideal zone plate is $Z^o(t)$ then we may write $Z(t) = Z^o(t) + E(t)$ where $E(t)$ is a random process with spaces of random width. (In two dimensions the problem is more complicated because $r_n(\phi)$ is also a function of the angle (Fig. 2.1.7) i.e., $r_n(\phi) = r_n^o + \delta_n(r_n, \phi)$.)

Consider the one-dimensional case. $E(t)$ is illustrated in Fig. 2.1.8,c. This is a stochastic process with a few restrictions: 1. $E(t)$ can have only 2 values -1, +1. 2. The spikes have a random width lying between zero and $q/4$. 3. One edge of the function is always located at $t = nq$. In Fig. 2.1.8.d we see that this random process can be described as a series of impulses. Let t_j be the solution of the equation:

$$\sin\left\{\pi\left[\frac{1}{q}t + \phi(j,q)\right]\right\} = 0 \quad \text{or} \quad \pi\left[\frac{t_j}{q} + \phi(j,q)\right] = j\pi$$

where $j = 1,2,3,\ldots$ and where $\phi(j,q)$ is a discrete random process satis-

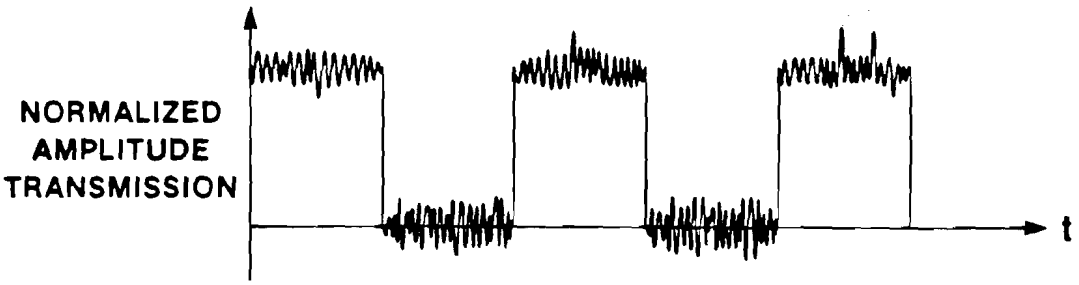

Fig. 2.1.6
Grain noise in a zone plate recorded on film or surface roughness fluctuations in a reflection diffraction grating. t is the distance square coordinate for a zone plate or the real distance coordinate for gratings.

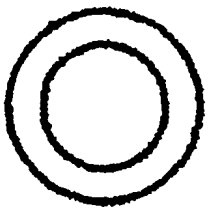

Fig. 2.1.7
A representation of a zone plate (only 2 zones) with the serration introduced in the manufacturing process.

fying $-\frac{q}{4} \leq \phi(j,q) \leq \frac{q}{4}$ and for every j, $\phi(j,q)$ is a uniformly distributed random variable in the interval $\left[\frac{q}{4}; \frac{q}{4}\right]$. Also let N(j) be another discrete random process which assumes with probability 1/2 for odd or even integral values. With these definitions the random process in Fig. 2.1.8 d can be written as:

$$E(t) = \sum_{j=1}^{N} \delta(t - t_j) \cdot \cos\left[N(j)\,\frac{\pi}{2}\right]$$

Consider the diffraction pattern of Z(t): $\tilde{Z}(u) = \tilde{Z}^{o}(u) + \tilde{E}(u)$. The serration acts to produce an additive noise. Calculating $\langle \tilde{E}(u_1)\tilde{E}(u_2)\rangle$ and $\langle |\tilde{E}(u)|^2 \rangle$ in terms of E(t) is possible by assuming stationarity. From $\langle \tilde{E}(u_1)\ \tilde{E}(u_2)\rangle$ we may also find the power spectrum [2.1.14] and hence find the characteristics of the scattering on axis for a zone plate, (and on the plane where the diffraction is observed in the case of gratings). Using a one-dimensional model means that the errors are assumed symmetric in the zone plate. This is, of course, not a fully realistic model but it still gives a feeling of what to expect.

The grain noise, on the other hand, acts as a multiplicative noise so that $Z(t) = Z^{o}(t).g(t)$. Again assuming symmetrical noise we get $\tilde{Z}(u) = \tilde{Z}^{o}(u) * \tilde{g}(u)$. The grain noise spectrum thus convolves with the noise free pattern.

In Fig. 2.1.9 a comparison between the grating and zone plate cases is shown. In the grating case, Fig. 2.1.9.a, the speckle pattern is essentially the same at all orders because the orders

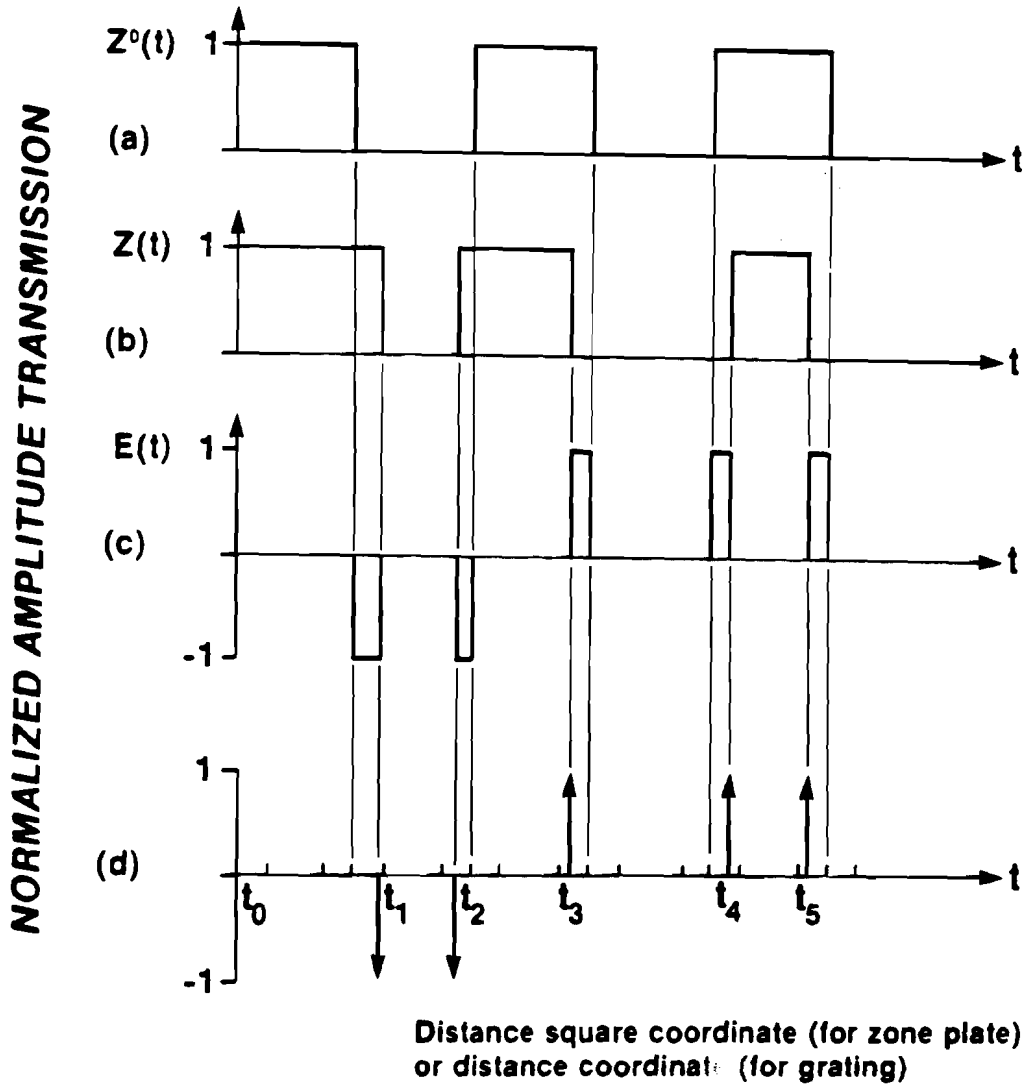

Fig. 2.1.8
Modeling the noise introduced by random flucuations in the zone radii or imperfections in the straightness of the diffraction grating grooves. (a) $Z^{\circ}(t)$ is the ideal Fresnel zone plate, (b) z(t) is the real zone plate, (c)$E(t) = Z^{\circ}(t) - Z(t)$, (d) random process that describes the deviation from an ideal zone plate.

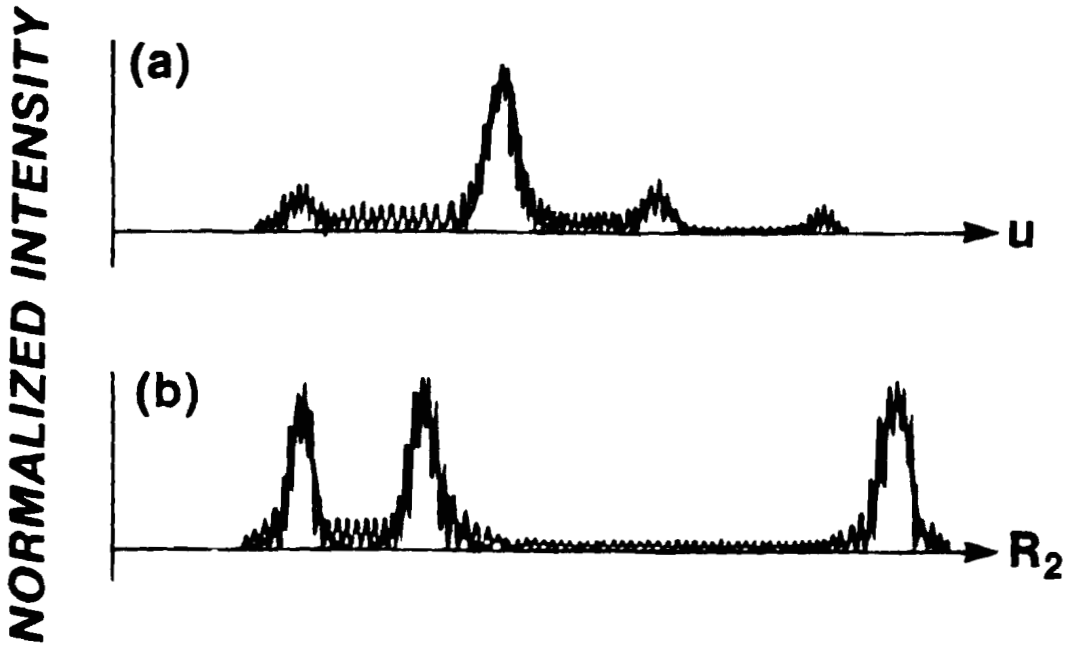

Fig. 2.1.9
Noise effects. (a) The noise convolves with the diffraction pattern in the case of gratings, (b) the noise convolves with the on axis intensity distribution in the case of zone plates.

are equally separated. But in the case of zone plates the orders are not equally spaced and the convolved pattern at higher orders must shrink. Hence the appearance of the speckle pattern changes along the axis. (This discussion does not say anything about the transverse distribution of speckle in the different orders. This will be done when Fresnel transformations are considered in a later section.) If we want to examine the fainter high orders it may be useful to employ a converging light beam rather than a collimated light beam. This can reverse the relative axial location of the foci, making the grain noise contribution less severe.

The serration contributes background noise. The only way to reduce this type of noise is to manufacture a better quality zone plate with less serration.

2.1.10 Aberrations in Zone Plates.

Third order contributions to the aberration function were calculated by Young [2.1.15]. The aberrations arise because of the error introduced in the derivation of (2.1.1), where the square root in the exponent was approximated only to first order.

The first remarkable feature about zone plates in this context is that there is no distortion term as with a regular lens since the chief ray does not deviate as it passes through the zone plate. The second interesting feature is that it is possible to correct for spherical aberration in the production process. One of the methods for manufacturing zone plates is by interfering a plane wavefront and an aspherical wavefront (or 2 spherical wavefronts). In Ref.

[1.11] a method is described, in which an aspheric wavefront is produced and interferes with another spherical wavefront so that the correction is built into the zone plate. In fact, we can always choose radii for two spherical wavefronts (i.e. you don't need an aspherical wavefront) such that by interference will produce the required correction. We thus get an optical device free of both spherical aberration and distortion. Furthermore, if we use the zone plate in the imaging mode, and if it is manufactured in the way which is discussed in an earlier section to enhance higher order efficiency, then by shifting an eye piece from order to order we can get a zooming effect without any additional element. The last two features have not yet been fully realized but it may become practical in the soft x-ray region.

Higher order reconstruction is important in the pseudoholography technique. At higher orders the F/# is smaller, hence the aberrations become more pronounced. In Ref. [2.1.15] the condition for image quality of better than $\lambda/4$ is $N^2 < 2F/\lambda$; where N is the number of zones, F is the focal length, and λ is the wavelength of the reconstructing light beam. For f=10cm, λ=5000Å, N<600 zones. In Fig. 2.1.10 we see an explanation for the fact that at a higher order p there are effectively pN zones. If we think of reconstructing at the sixth order we should not use a zone plate with more than 100 zones.

Chromatic aberration is also dependent on the number of zones. The pinhole camera - the simplest zone plate - is free of lateral color.

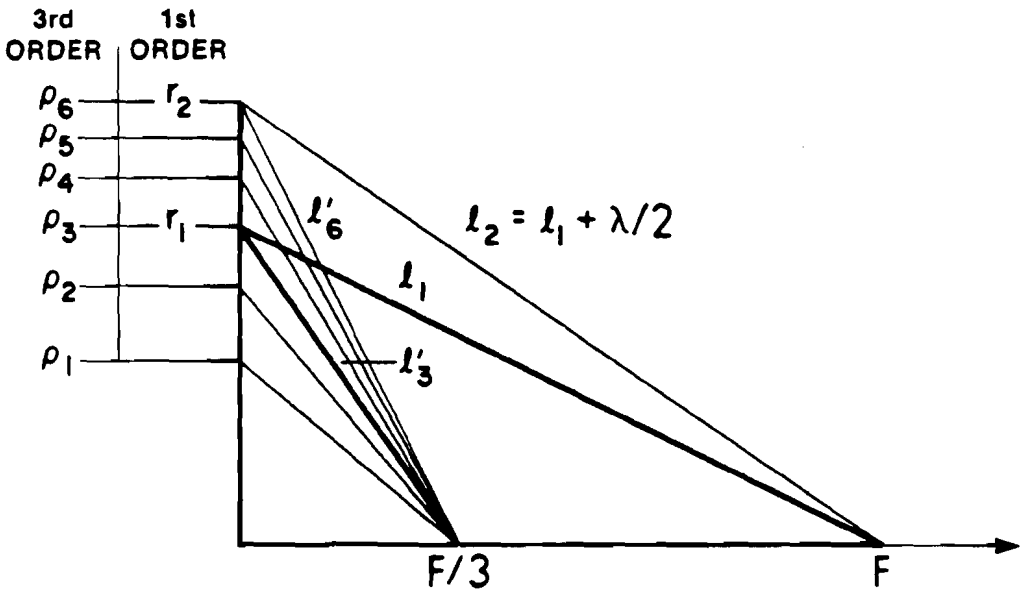

$$l'_6 = \sqrt{(F/3)^2 + r_2^2} \simeq F/3 + \frac{3}{2}\frac{r_2^2}{F} = F/3 + \frac{3}{2}\cdot 2\lambda$$

$$l'_3 = \sqrt{(F/3)^2 + r_1^2} \simeq F/3 + \frac{3}{2}\frac{r_1^2}{F} = F/3 + \frac{3}{2}\cdot \lambda$$

$$l'_6 - l'_3 = 3/2\lambda \; ; \quad l_2 - l_1 = \lambda/2$$

Fig. 2.1.10
At higher orders, the zones get narrower and the effective number of zones gets larger.

2.1.11 Computer Simulations.

In order to get a better feeling for the performance of the various zone plate designs, it is useful to plot the intensity distribution of the light at the different foci as a function of zone plate parameters such as N(the number of zones), EPS(the width of the individual zone: see Fig. 2.1.4.b) and the zone shape (see Fig. 2.1.4). Two kinds of plots are of interest to us: 1. the axial intensity distribution and 2. the transverse intensity distribution.

2.1.11.1 Axial Intensity Distribution.

2.1.11.1.1. A discussion regarding a computer program that calculates the axial intensity distribution.

The axial distribution is given by Eq. (2.1.9)

$$G'(u) = \int_0^1 A(t)\, e^{2\pi i u t}\, dt \qquad (2.1.9a)$$

If one is only interested in plotting this distribution in the u domain, then one can use the Fast Fourier Transform (FFT) algorithm to plot G'(u). This distribution is observed in the case of the Fraunhofer diffraction from a grating. However, if we are interested in the axial intensity distribution from zone plates so we have to replot G(u), scaling the coordinates in such a way as to get G(Z), where Z is proportional to 1/u. This is a subtle problem which it will be useful to discuss briefly.

We first obtain the discrete form of Eq. (2.1.9 a), the Discrete Fourier Transform (DFT):

$$G(m\Delta u) = \sum_{n=1}^{N} A(n\Delta t) \exp 2\pi i \frac{nm}{N} \cdot \Delta t \qquad (2.1.9b)$$

Eq. (2.1.9.b) is obtained using the following definitions:

$$\Delta t = \frac{TOTD}{N-1} ; \quad \Delta u = \frac{N-1}{TOTD} \frac{1}{N} \qquad (2.1.22)$$

where N is the number of samples used, m and n are integers, and TOTD is the size of the space in the input plane. (The size of the aperture itself may be only a fraction of TOTD as will be discussed later.) From Eq. (2.1.15), (2.1.9 b) and (2.1.22) we may write the intensity distribution $I(m\Delta u)$ as:

$$I(m\Delta u) = ESCALE \left| \sum_{n=1}^{N} A(n\Delta t) \exp 2\pi i \frac{nm}{N} \right|^2 \qquad (2.1.9c)$$

where $ESCALE = \left(\frac{a^2}{\lambda Z} \cdot \pi \cdot \frac{TOTD}{N-1} \right)^2$. To find Δu from Δt we use: $\Delta u = USCALE \Delta t$ where $USCALE = \left(\frac{N-1}{TOTD} \right)^2 \cdot \frac{1}{N}$. $I(m\Delta u)$ is thus calculated by the FFT algorithm and can be plotted using the scaling factors ESCALE and USCALE.

However, we would also like to plot the distribution in real space, i.e. Z space. If Z is the distance in an on axis from the zone plate and TOTDX is the extent of Z space then it is useful to define a quantity by $Z = \zeta TOTDX$. We usually choose TOTDX=F where F is the primary focal length. From Eq. (2.1.4), $u=(a^2/2\lambda Z)$ for collimated light. But $a^2=(NZONE)\lambda F$ and $Z = F$, therefore, $u = \frac{NZONE}{2} \cdot \frac{1}{\zeta}$

where NZONE is the number of zones. Let $\bar{\zeta} = \frac{1}{\zeta}$. If now we want to plot $I(m\Delta\bar{\zeta})$ we have to scale $\Delta\bar{\zeta} = USCALE(\bar{\zeta}) \cdot \Delta t$

where $$USCALE(\bar{\zeta}) = \frac{2}{NZONE} \cdot \frac{1}{N} \cdot \frac{(N-1)}{TOTD}$$

$\bar{\zeta}$ space is merely a scaled version of u space. To get the intensity distribution in terms of $Z = \zeta F = \frac{F}{\bar{\zeta}}$ we plot $I(m\Delta\bar{\zeta})$ as a function of $\frac{1}{\bar{\zeta}}$.

The interpolation of sampled data is an important problem in such calculations. As an example suppose that TOTD is the extent of the input space, and A is the width of the aperture function. The sampling interval is $\Delta = \frac{TOTD}{N-1}$ in the input space. Therefore, in the transform space the sampling interval will be $\delta = \frac{1}{TOTD}$ or $\delta = \frac{\lambda Z}{TOTD}$ cm. From this the total width of the transform space is $TBDW = \frac{N\lambda Z}{TOTD}$ (see Fig. 2.1.11 for a visualization of these quantities). If A is comparable with TOTD then the corresponding width in the Fourier domain will be very small with respect to the total spaee size N/TOTD (Fig. 2.1.11.B). To exhibit the pattern we scale down the space coordinate and interpolate between the values of $I(m\Delta\bar{\zeta})$. If the scaling factor is too large we may get erroneous results. Therefore, if we choose A to be a small fraction of TOTD then the width in the transform plane will be large compared with the total space size and we will not need to scale and interpolate. However, to do that we will need many more data points so that a compromise must be made.

One of the interpolation procedures is the polynomial inter-

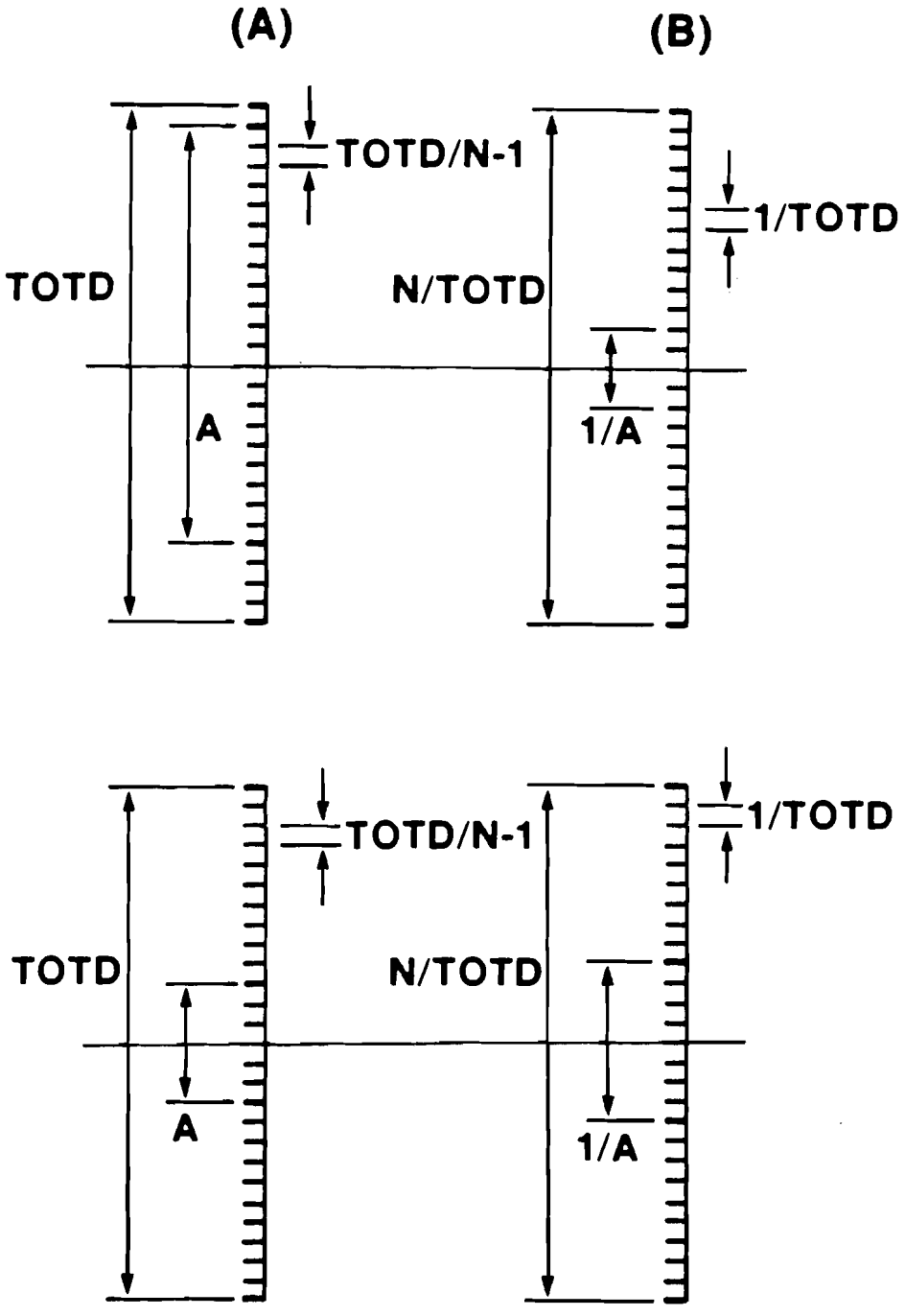

Fig. 2.1.11
Relation between the extent of the input function (A) and the extent of the output function (B) when using the FFT algorithm to compute the Fourier transform of a sampled function.

polation where we fit a polynomial through four successive data points, and then calculate from this polynomial the intermediate data points (see Ref. [2.1.17]). The main problem with this procedure is that it tends to give erroneous results when we scale the plots by a factor larger than 2. To reduce the error we may fit the polynomial through more than four data points but with greatly increased computing time.

Another procedure is described in Ref. [2.1.17]. It is based on the sampling theorem (see Ref. [2.1.14]) by which every band limited function can be fully reconstructed from an infinite series of sampled data values, provided that the sampling frequency is not less than twice its bandwidth. Here errors arise from the fact that we cannot obtain an infinite series of points. However, it turns out that if the parameters are chosen carefully this procedure may be better than the previous one for equivalent computing times.

A computer program based on the remarks mentioned above was written and is listed in Ap. 1.

2.1.11.1.2 Conclusions from the plots obtained by the computer program.

The distribution in the 1/z domain is the familiar Fraunhofer diffraction pattern of a grating and we will not plot it here. However, the distribution in the real space z is of considerable interest to us here. The different cases are summarized in Table 2.1.4. EPS1, EPS2, B1 and B2 are defined in Fig. 2.1.12. In Fig. 2.1.13 a the case of an idealized Fresnel zone plate is plotted.

Table 2.1.4: Parameters of the Different Computer Runs, Calculating the On Axis Intensity Distribution from Zone Plates

Run #	(NZONE) # of Zones	POSITIVE or NEGATIVE Zone Plates	EPS1	EPS2	B1	B2	(N) # of Points	Fig. #
1	37	POSITIVE	0.5	0.5	0.5	0.5	3645	2.1.13a
2	37	POSITIVE	0.5	0.5	0.3	0.3	3645	2.1.13b
3	37	POSITIVE	0.4	0.4	0.4	0.4	3645	2.1.14a
4	37	POSITIVE	0.4	0.4	0.3	0.3	3645	2.1.14b
5	11	POSITIVE	0.5	0.5	0.5	0.5	3645	2.1.15

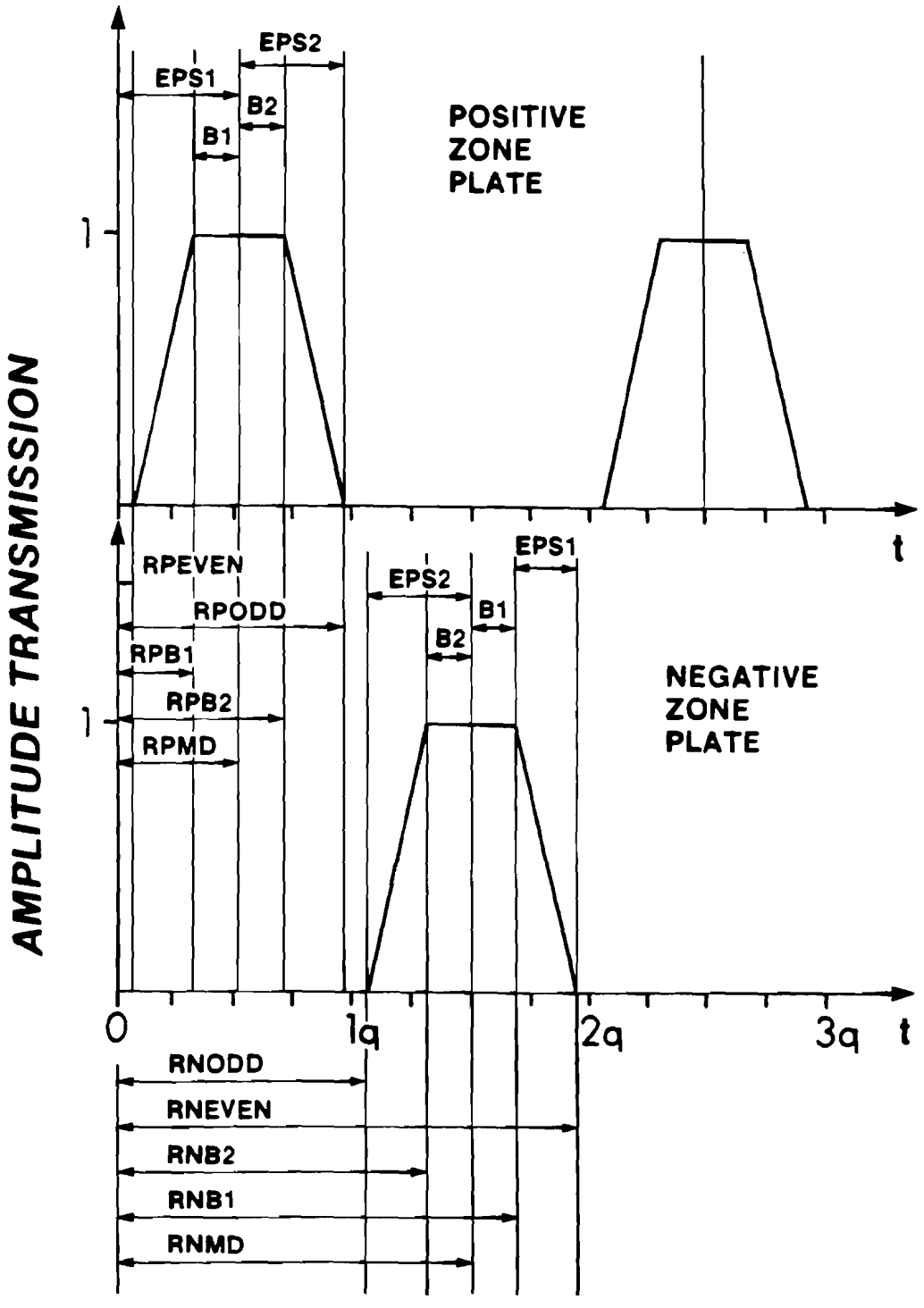

Fig. 2.1.12
Definitions of all the relevant quantities used to represent a zone plate in the computer program. (t is the square distance coordinate.)

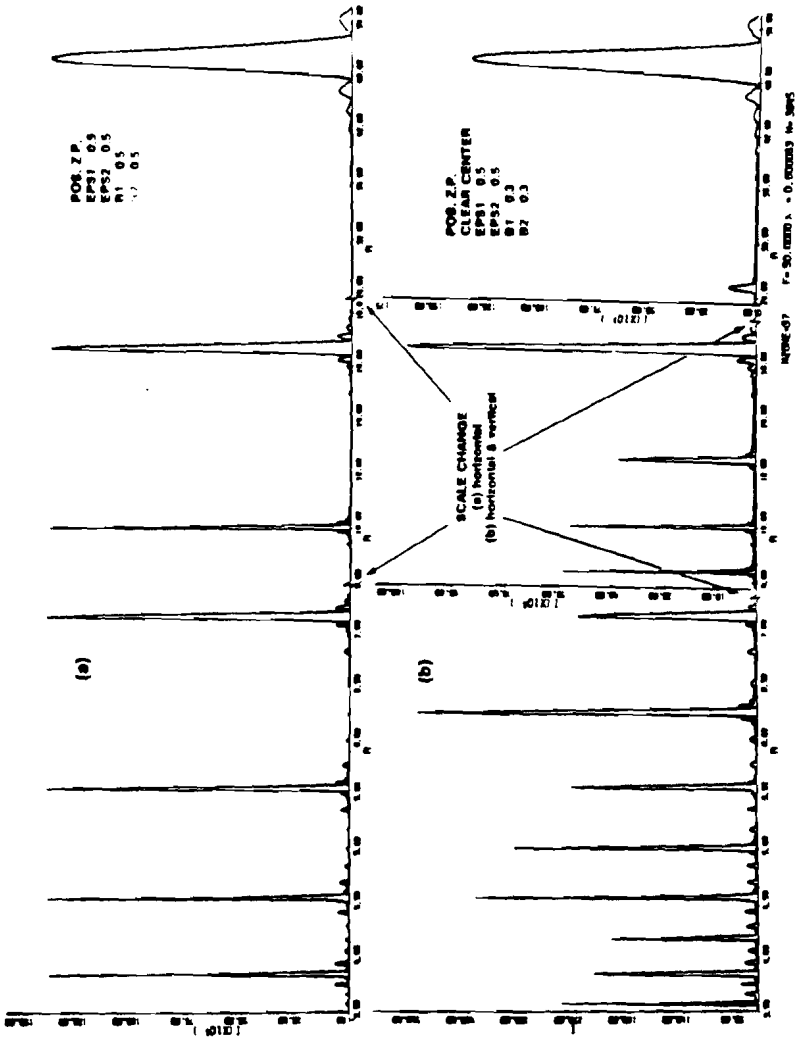

2.1.13
Axial intensity distribution of light focused by a zone plate of 37 zones. (a) Ideal Fresnel plate (EPS = 0.5), (b) modified zone plate with slanted edges (EPS = 0.5; B = 0.3).

Only odd foci appear and all have exactly the same on axis intensity as predicted by Eq. (2.1.17). In order to show the different orders the plot had to be scaled up at higher orders. The case 37 zones was depicted since this is the number of zones in the zone plate used in the x-ray experiment. In the first order the width of the spike is quite large: about 3cm. This limits seriously the tomographic capability of the system. No attempt was made to calculate higher orders than the 14th order. In Fig. 2.1.13.b the case of the same zone width but with slanted edges is plotted. Even orders appear but they are strongly attenuated. The odd orders are also attenuated. The decrease in the width at higher orders is clearly demonstrated enabling higher tomographic resolution at higher orders. Although the effect of slanted edges is to attenuate the higher orders we may still find orders with appreciable on axis intensity in this case. In Fig. 2.1.14 two cases with narrow zones are plotted. In Fig. 2.1.14 a the edges are straight, while in Fig. 2.1.14.b they are slanted. Comparing Fig. 2.1.14.b with 2.1.13.b we see that when the zones are narrower, slanted edges do not cause as much attenuation as with zones which have the ideal width of a Fresnel zone plate. This suggests that we may be able to design a zone plate where high orders have still an appreciable on axis intensity in spite of the fact that diffraction effects are present in the recording step of the pseudohologram.

In Fig. 2.1.15 the case of 11 zones is shown, to demonstrate the critical dependence of the width of the orders as function of the number of zones in the zone plate. In this case the first order

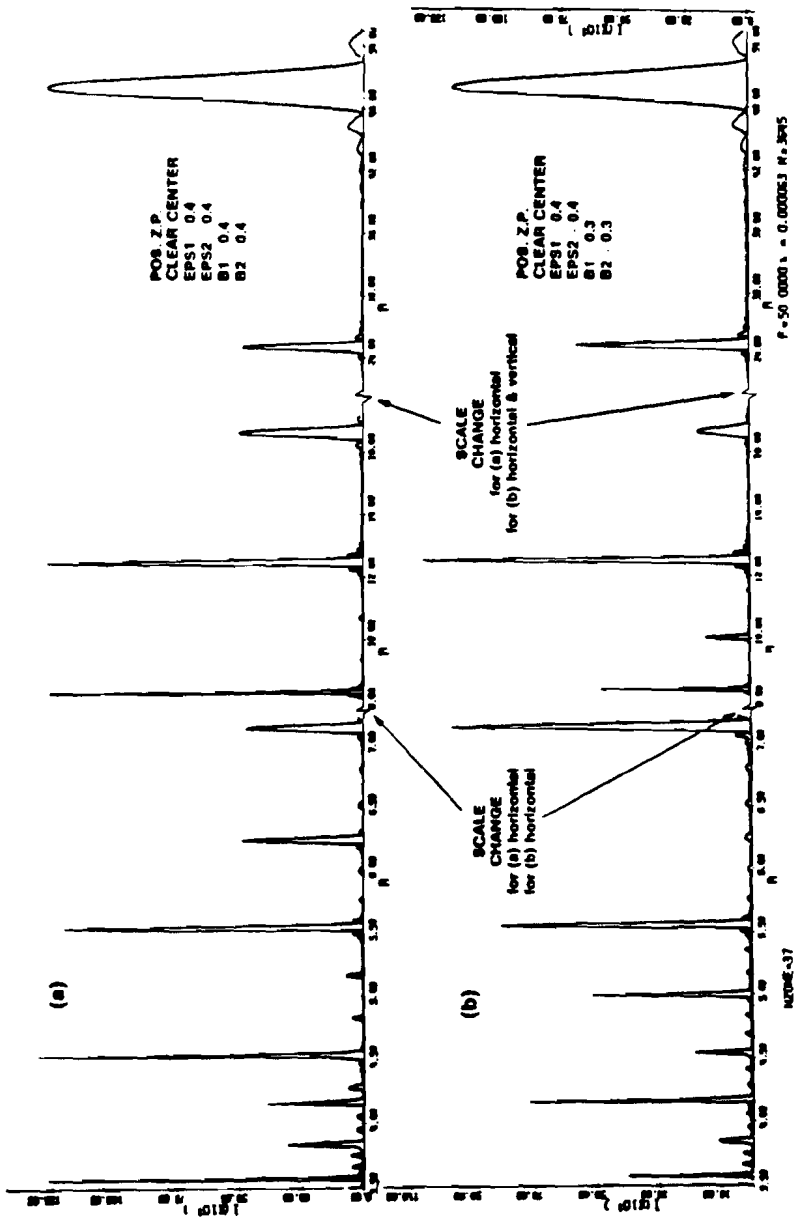

2.1.14
Axial intensity distribution of light focused by a zone plate of 37 zones. (a) Narrow and sharp zones (EPS=0.4, B=0.4). (b) Narrow zones with slanted edges (EPS=0.4, B=0.3).

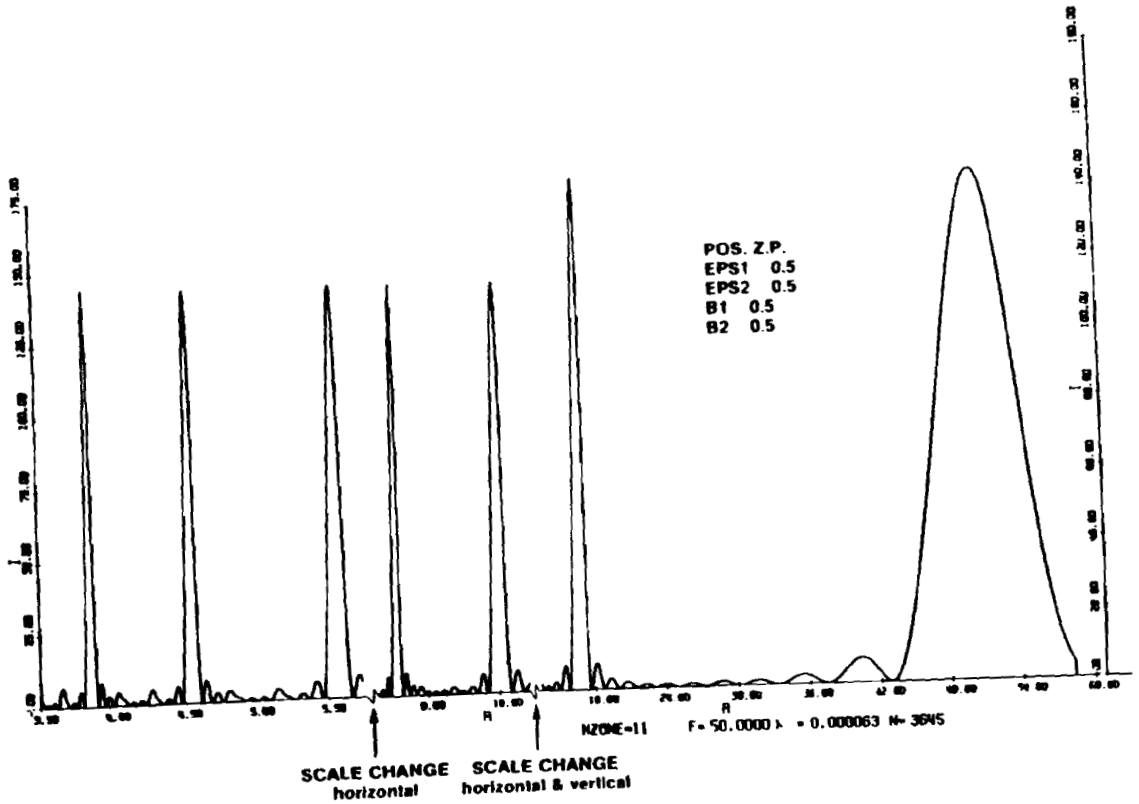

2.1.15
Axial intensity distribution of light focused by a Fresnel zone plate of 11 zones.

extends over 18cm while in Fig. 2.1.14, over 3cm.

2.1.11.2 Transverse Intensity Distribution.

For a fixed Z Eq. (2.1.1) gives the transverse intensity distribution. Using the small angle approximation (e.g. (2.1.2) and (2.1.3)), Eq. (2.1.1) can be written as a Fresnel transformation. A computer program is avaiable to calculate this integral (see Ref. [2.1.17]). This program was modified to suit our needs and used to plot the transverse intensity distribution as a function of N, EPS, and zone shape. The calculation was done for the case where a plane wave is incident on a zone plate and is brought to a series of foci.

The different cases are summarized in Table 2.1.5

2.1.11.2.1 Effect of the zone shape on the intensity distribution of the various orders.

In Fig. 2.1.16 we plot two cases: (a) the ideal Fresnel zone plate (EPS = 0.5), (b) zone plate with narrow zones. In the case (a) the even orders are very weak, about two orders of magnitude weaker than the odd orders. In theory they should be zero but since we are sampling the aperture with finite number of points, an error is introduced and the even orders are not identically zero. All the odd orders are of equal height as predicted by Eq. (2.1.17). The width reduces from about 200μm in the first order to about 20μm in the 9th order. In the case (b) even orders appear and can become quite strong. In this case some higher orders are even stronger than the first order (for example, 2nd order and fifth order). Hence,

Table 2.1.5: Parameters describing the plots in section 2.1.11.2

#	NZONE	EPS1	EPS2	B1	B2	F	N	Fig. #	POS/ NEG	Order	Dim.
1	37	0.5	0.5	0.5	0.5	150	2048	2.1.16a	POS	1-10	2
2	37	0.3	0.3	0.3	0.3	150	2048	2.1.16b	POS	1-10	2
3	11	0.5	0.5	0.5	0.5	150	2048	2.1.17a	POS	3	2
4	33	0.5	0.5	0.5	0.5	50	2048	2.1.17b	POS	1	2
5	11	0.5	0.5	0.5	0.5	50	2048	2.1.17c	POS	1	2
6	Lens	---	---	---	---	50	2048	2.1.17d	---	---	2
7	11	0.5	0.5	0.5	0.5	150	6144	2.1.18a	POS	1,3,5	1
8	37	0.5	0.5	0.5	0.5	150	6144	2.1.18b	POS	1,3,5	1
9	61	0.5	0.5	0.5	0.5	150	6144	2.1.18c	POS	1,3,5	1
10	11	0.5	0.5	0.5	0.5	150	6144	2.1.19a	NEG	1,3,5	1
11	37	0.5	0.5	0.5	0.5	150	6144	2.1.19b	NEG	1,3,5	1
12	61	0.5	0.5	0.5	0.5	150	6144	2.1.19c	NEG	1,3,5	1

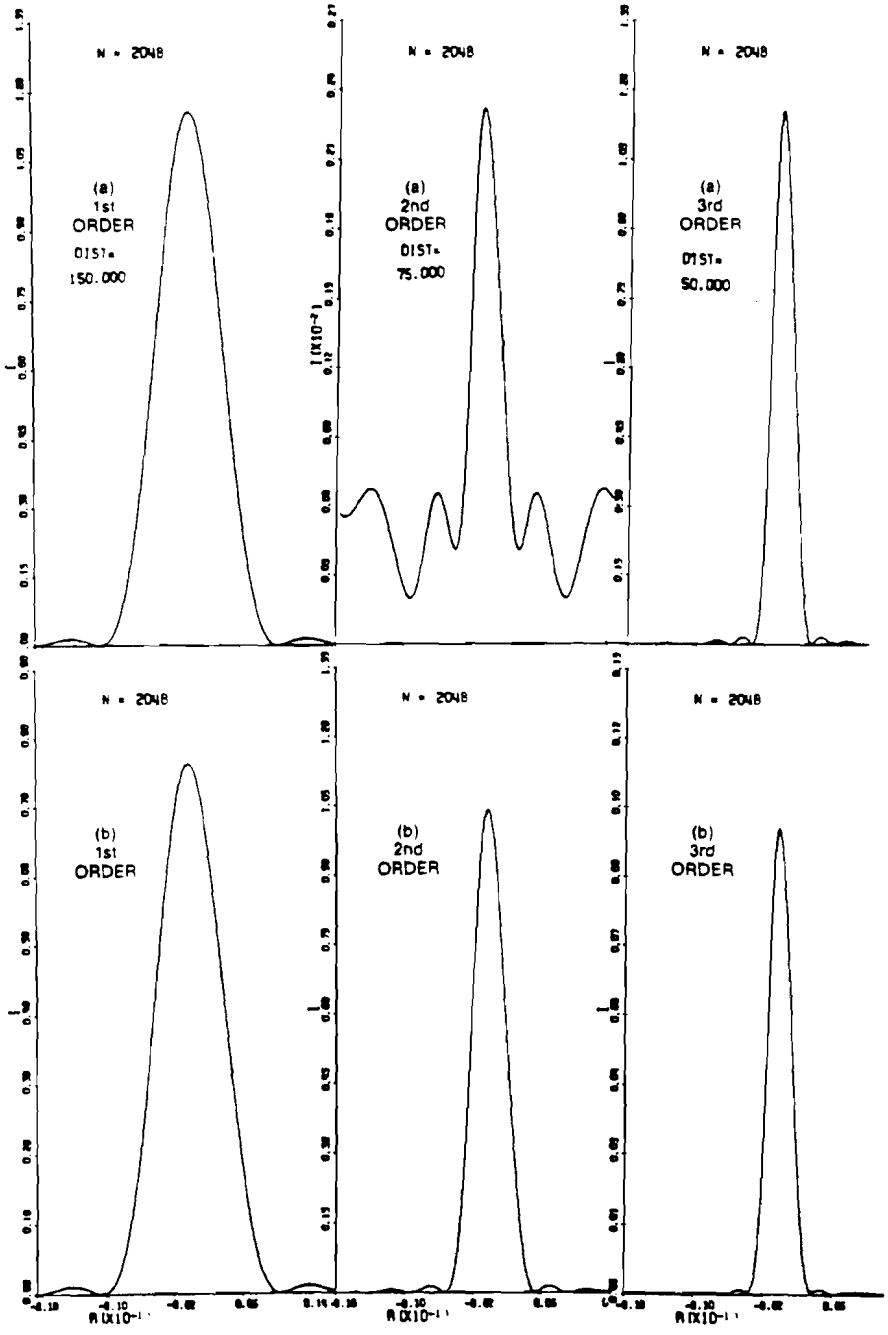

Fig. 2.1.16
Transverse intensity distribution at various orders of light focused by a zone plate. (a) Fresnel zone plate (EPS = 0.5), (b) modified zone plate (EPS = 0.3) (See Fig. 2.2.12 for notation.)

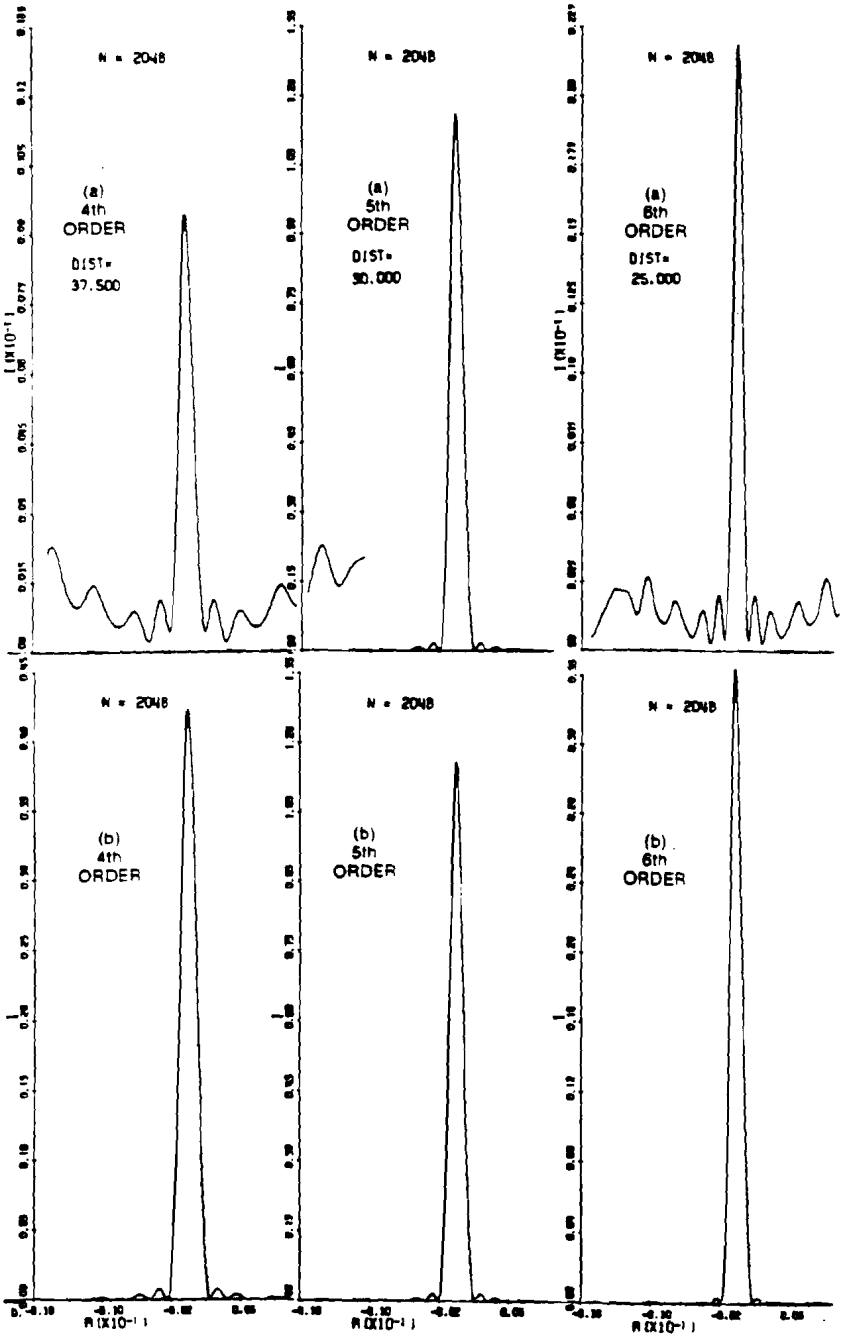

Fig. 2.1.16 (cont.)

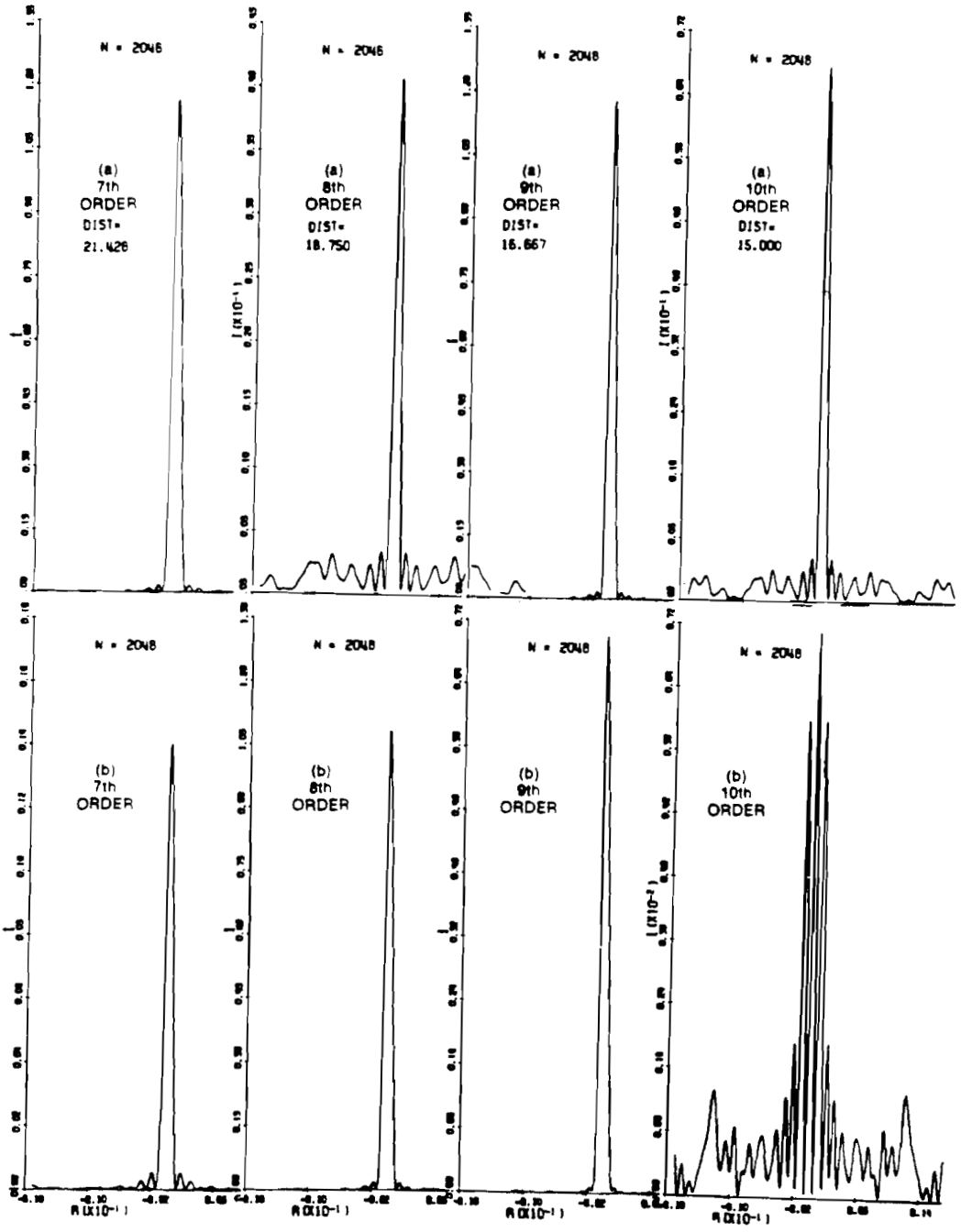

Fig. 2.1.16 (cont.)

narrowing the zones has sometimes the effect of blazing the zone plate directing more light to higher orders at the expense of lower orders.

2.1.11.2.2 The effective number of zones increases at higher orders.

In Fig. 2.1.17.a we plot the transverse intensity distribution of a zone plate, of 11 zones and 150cm focal length, at the third order. In Fig. 2.1.17.b we plot the transverse intensity distribution of a zone plate, of 33 zones and 50cm focal length, at the first order. Since the F/# is smaller in the latter case we get higher intensity but the shape of the curve and the width of the pattern are very similar. There is a little difference in the secondary lobes. In the case of 2.1.17.a the intensity of the secondary lobes does not decrease as fast as in 2.1.17.b. This causes background in imaging and in reconstruction at high orders of a pseudohologram. However, for larger number of zones this effect becomes negligible. We thus see that the effective number of zones at the third order of 2.1.17.a is the same as the number of zones at the first order of 2.1.17.b.

Also it is interesting to compare the transverse intensity distribution of a zone plate and a lens of comparable focal length and aperture. From 2.1.17.c and 2.1.17.d we conclude that the efficiency of a zone plate is approximately 12%. Also the third lobe in 2.1.17.c is higher than the second while in 2.1.17.d the intensity of the secondary lobes decreases fast as a function of the distance from the center. This again demonstrates the problem when using a zone plate with small number of zones, i.e.: the secondary lobes contribute to the background and decrease the signal to noise ratio.

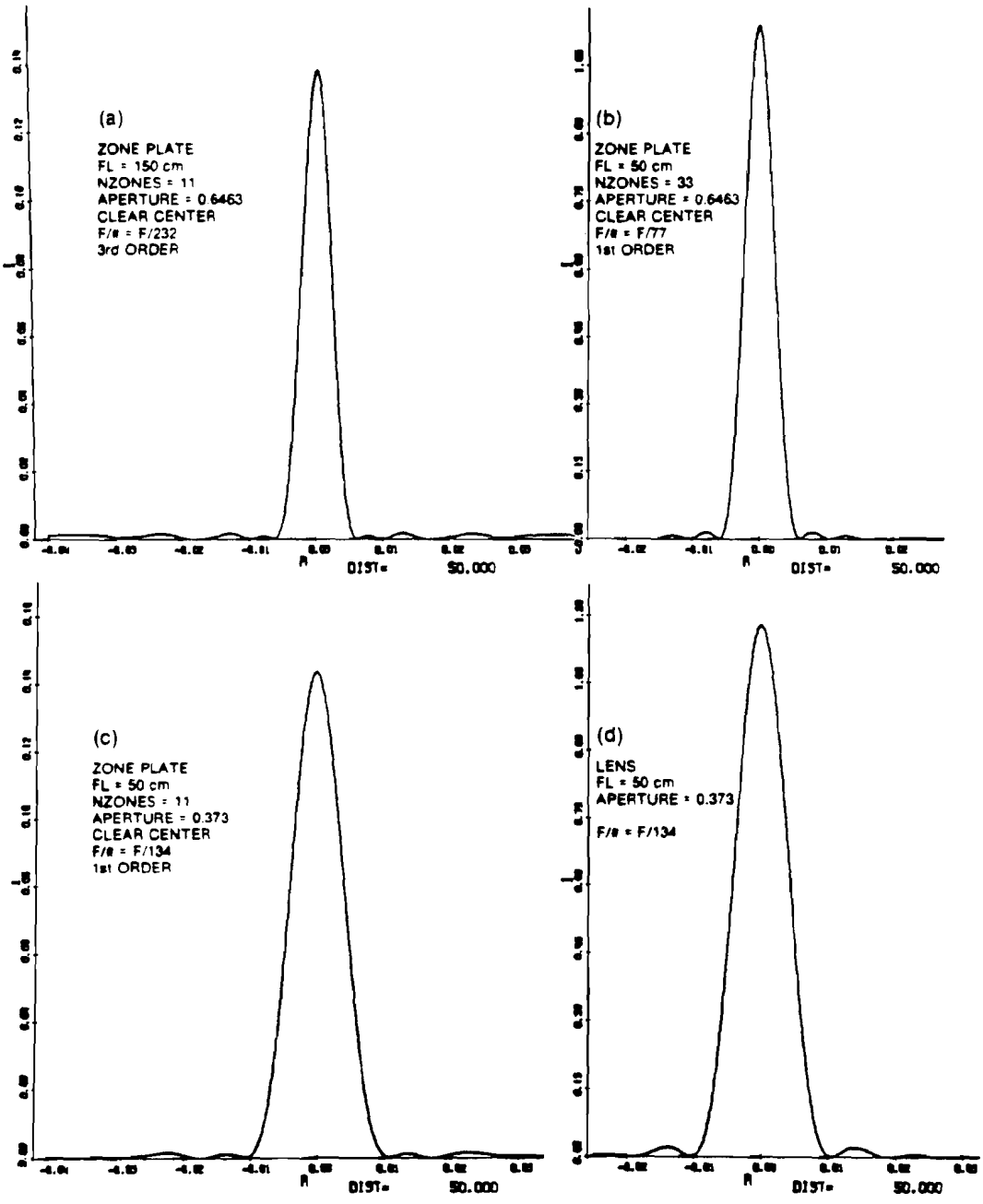

Fig. 2.1.17
Transverse intensity distributions focused by zone plates and a lens.

2.1.11.2.3 Comparison between one-dimensional and two-dimensional zone plates.

In Fig. 2.1.18 the transverse intensity distributions of light focussed by one-dimensional zone plates are shown. By comparing Fig. 2.1.18 with 2.1.16 and 2.1.17 we conclude that two-dimensional zone plate pseudoholography is much more efficient than one-dimensional zone plate pseudoholography. First of all the on axis intensity decreases at higher orders while for the two-dimensional case it does not change. And secondly, the background problem is much more severe in the one-dimensional case. In order to achieve satisfactory results, we must use a one-dimensional zone plate with at least 100 to 150 zones. In the two-dimensional case, on the other hand, 40 zones will give reasonably good reconstruction. In Fig. 2.1.19 the case of negative one-dimensional zone plate is illustrated. It can be seen that as long as the object is smaller than the innermost zone then the one-dimensional zone plate is still useful for pseudo-holography.

If higher order reconstructions are needed then the object size is further limited as can be seen in Fig. 2.1.19 at DIST = 50 or DIST = 30, which correspond to third and fifth orders respectively.

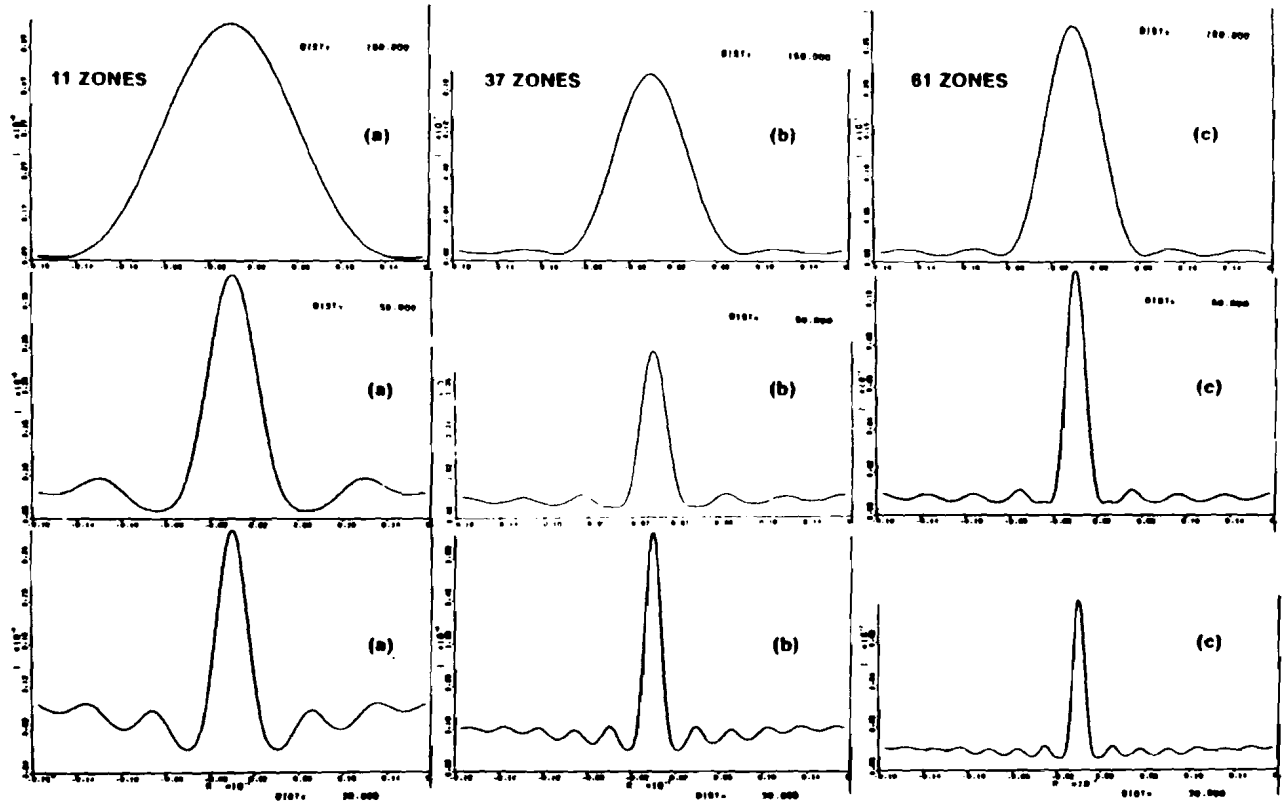

Fig. 2.1.18
Transverse intensity distributions of light focused by one dimensional positive zone plates. DIST is the distance from the zone plate in cm, 150 cm being the fron order focus. (a), (b) and (c) are 11, 37, 61 zones zone plate cases respectively.

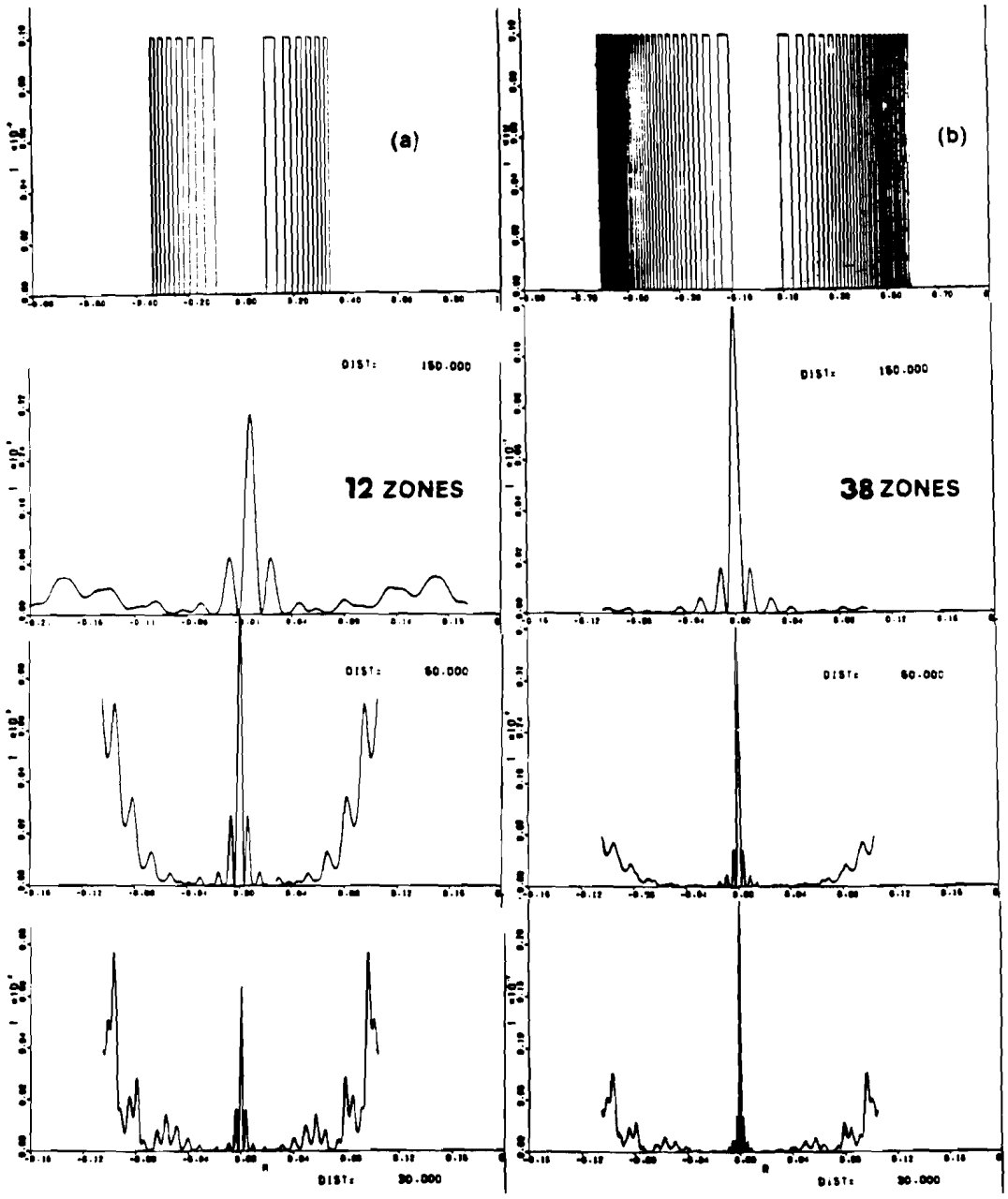

Fig. 2.1.19
Transverse intensity distributions of light focused by one dimensional negative zone plates. DIST = 150, 50, 30 correspond to the first, third and fifth order foci. (a), (b) and (c) are 12,38 and 62 zones zone plate cases respectively.

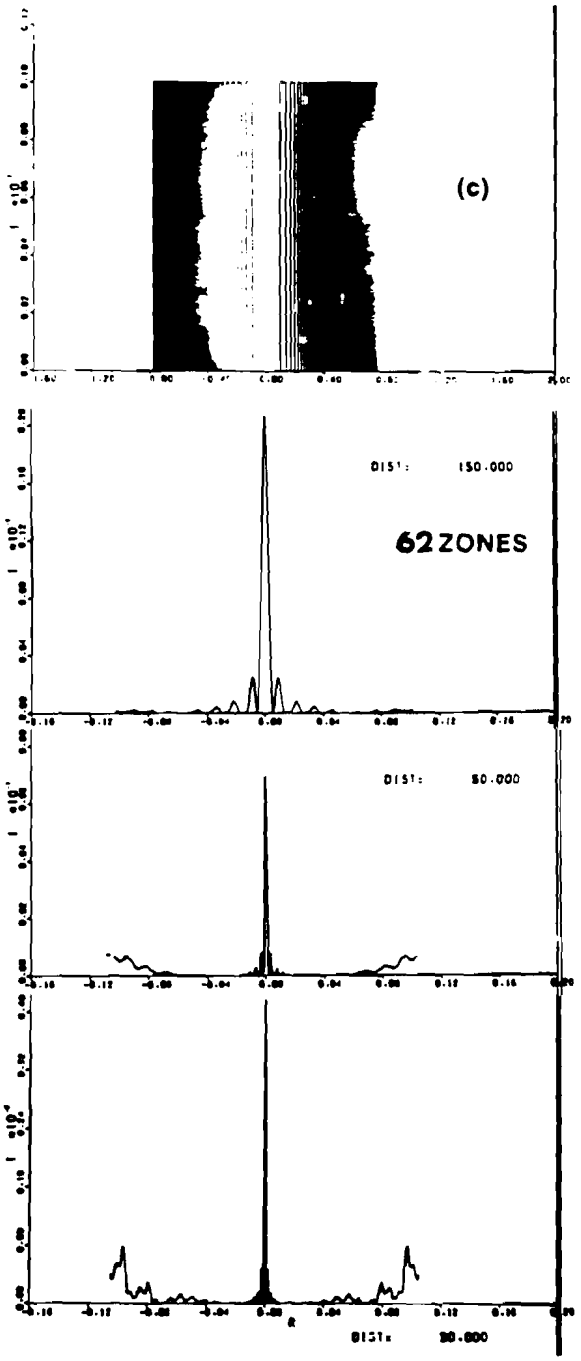

Fig. 2.1.19 (cont.)

2.1.12 REFERENCES

2.1.1 M. Born and E. Wolf, "Principles of Optics", (Pergamon press) 5th Edition.

2.1.2 J. W. Goodman, "Introduction to Fourier Optics", (McGraw-Hill) 1968, p. 12, eq. 2-14.

2.1.3 R. G. Simpson and H. H. Barrett, "Coded Aperture Imaging" in "Imaging in Diagnostic Medicine", Ed. S. Nudelman (Plenum Publishing Corp., NY).

2.1.4 Alberic Boivin, "On the Theory of Diffraction by Concentric Arrays of Ring-Shaped Apertures", J. Opt. Soc. Am. 42, 60 (1952). See discussion following Eq. 28, p. 63. The conditions for maxima $y=(2j+1)2\pi$ are given but he does not stress the fact that ω too changes in the same way.

2.1.5 Milburn Sussman, "Elementary Theory of Zone Plates", Am. J. Phys. 28, 394 (1960). See Fig. 4, p. 396.

2.1.6 Henri Arsenault, "Diffraction Theory of Fresnel Zone Plates", J. Opt. Soc. Am. 58, 1536 (1968). See Eq. 11 and the immediate conclusion that irradiance goes as $1/(2j+1)^2\pi^2$.

2.1.7 There is a series of papers discussing the efficiency of higher orders.

(a) G. S. Waldman, J. Opt. Soc. Am. 56, 215 (1966).

(b) M. H. Hormon and H. H. M. Chan, "Zone Plate Theory Based on Holography", Appl. Opt. 6, 317 (1967).

(c) Kenneth I. Clifford and Gary S. Waldman, "Comments on Zone Plate Theory Based on Holography", Appl. Opt. 6, 1115 (1967).

(d) M. Horman, "Reply to Comments on Zone Plate Theory Based on Holography", Appl. Opt. 6, 1415 (1967).

2.1.8 J. Kirtz, "Phase Zone Plates for X-Rays and the Extreme U.V.", J. Opt. Soc. Am. 64, 304 (1974).

2.1.9 L. S. Cheo, J. Shmoys and A. Hessel, "On Simultaneous Blazing of Triangular Groove Diffraction Gratings", J. Opt. Soc. Am. 67, 1686 (1978).

2.1.10 E. V. Jull, J. W. Heath, and G. R. Ebbeson, "Gratings That Diffract All Incident Energy", J. Opt. Soc. Am. 67, 557 (1977).

2.1.11a A. Walsh, "Echelette Zone Plates for Use in Far Infrared Spectrometry", J. Opt. Soc. Am. 42, 213 (1952).

2.1.11b N. M. Ceglio and H. I. Smith, "An Efficient Lensing Element for X-Rays", 8th International Conference on X-Ray Optics and 12th Annual Conference of the Microbeam Analysis, Aug. 1977, Boston, Mass. p. 202A.

2.1.12 (a) J. C. Dainty Ed., "Laser Speckle and Related Phenomena", Springer - Verlag (1975).

(b) J. C. Dainty, "The Statistics of Speckle Patterns", Progress in Optics, E. Wolf Ed., North Holland (1976).

2.1.13 N. George and G. M. Morris, " Randomly Serrated Edges, Lines, and Apertures", J. Opt. Soc. Am. 67, 1416 ThK77 (1977).

2.1.14 A. Papoulis, "Probability Random Variables and Stochastic Processes", McGrow-Hill (1965).

2.1.15 M. Young, "Zone Plates and Their Aberrations", J. Opt. Soc. Am. 62, 972 (1972).

2.1.16 J. F. James and R. S. Sternberg, "The Design of Optical Spec-

trometers", (Chapman & Hall, Ltd., London 1969) p. 64.

2.1.17 E. Krisl, PhD. Thesis, "Apodization of Coherent Optical Systems", University of Rochester, (1978).

2.1.18 D. Stigliani, Jr., R. Mittra, R.G. Semonin, "Resolving Power of a Zone Plate", J. Opt. Soc. Am. 57, 610 (1967).

2.2 Limitations and Prospects of Pseudoholography.

The technique was introduced by Merz and Young [2.2.2] to astronomy, applied to nuclear medicine by Barrett [2.2.3] and to laser produced plasmas by Ceglio [2.2.4] Although a theoretical treatment of pseudoholography has already been given (Ref. [2.2.1] and Ref. [2.2.14]) these authors overlooked the reconstructions at higher order foci. For certain x-ray imaging applications the importance of pseudoholography relies heavily on the fact that a significant increase of resolution occurs in the higher order reconstructions. It thus seems appropriate to rederive the relevant relations in pseudoholography, this time including the high orders as well.

The main limitation of this method is the fact that for an extended continuous source the signal to noise ratio in the reconstruction decreases significantly. This disadvantage is alleviated somewhat if the object is smaller than the innermost zone. Also, it has been assumed ([2.2.1], [2.2.2], [2.2.3], [2.2.4] and references therein) that the shadow casting process can be described strictly by geometrical optics. In practice the system is partially coherent and diffraction cannot generally be neglected. These effects will be included in our treatment of the propagation of the mutual intensity for describing the coded aperture shadowgraphy technique. This will allow us to discuss enhancement techniques in cases where diffraction effects contribute to the deterioration of the pseudohologram.

2.2.1 Propagation of the Mutual Intensity.

Consider a plane view of the system. The coordinates are denoted as one-dimensional quantities but they represent two-dimensional vectors in some cases (this is done to simplify the notation). The recording of the shadowgram is illustrated in Fig. 2.2.1. From geometrical considerations (based on similarity between triangles and proportional relationships), the projections of the mask onto the film from any point in the source plane gives a magnified version of the mask. This is illustrated in Fig. 2.2.2.

Let $E(\alpha)$ be the monochromatic field radiated from the point source in the plane α and let $\sqrt{M(\xi)}$ be the amplitude transmittance of the mask in the plane ξ ($M(\xi)$ being the intensity transmittance). Treating the one-dimensional drawing for simplicity, we propagate the spherical wave from the plane α to the plane ξ. After multiplying by the mask function we propagate to the plane X. Using the Fresnel Kirchhoff integral and neglecting the obliquity factor we get

$$E(\xi) = \frac{i}{\lambda} \int_{-\infty}^{\infty} E(\alpha) \frac{e^{iKr(\xi,\alpha)}}{r(\xi,\alpha)} d\alpha \qquad (2.2.1)$$

Behind the mask we have:

$$E^{+}(\xi) = E(\xi) \sqrt{M(\xi)} \qquad (2.2.2)$$

We let the field at the plane ξ propagate to the plane X. Using the Fresnel Kirchhoff integral once more and substituting for $E^{+}(\xi)$ and $E(\xi)$ from (2.2.1) we get:

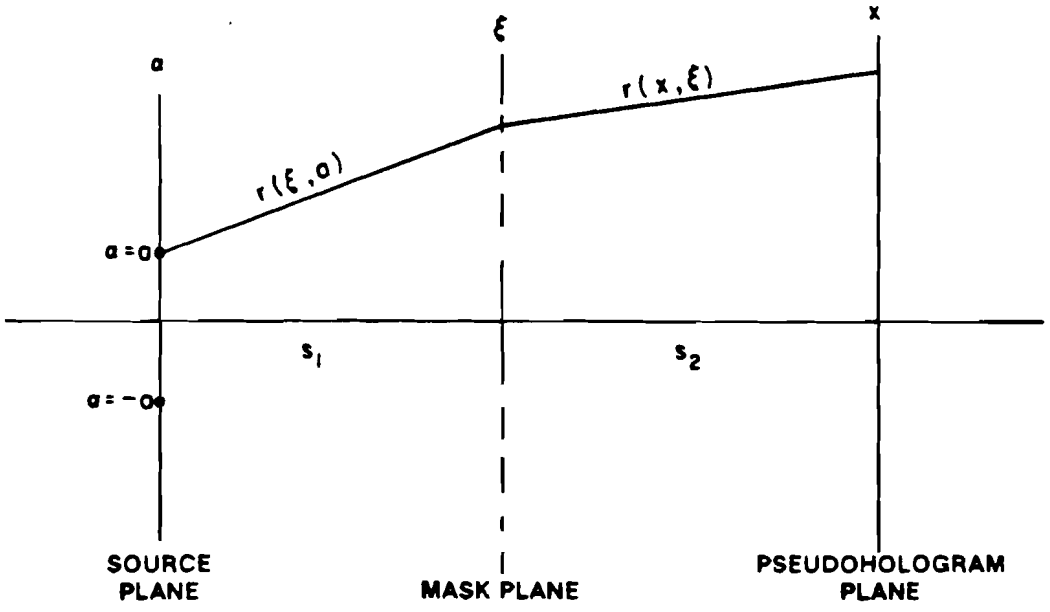

Fig. 2.2.1
The geometry for recording a pseudohologram.

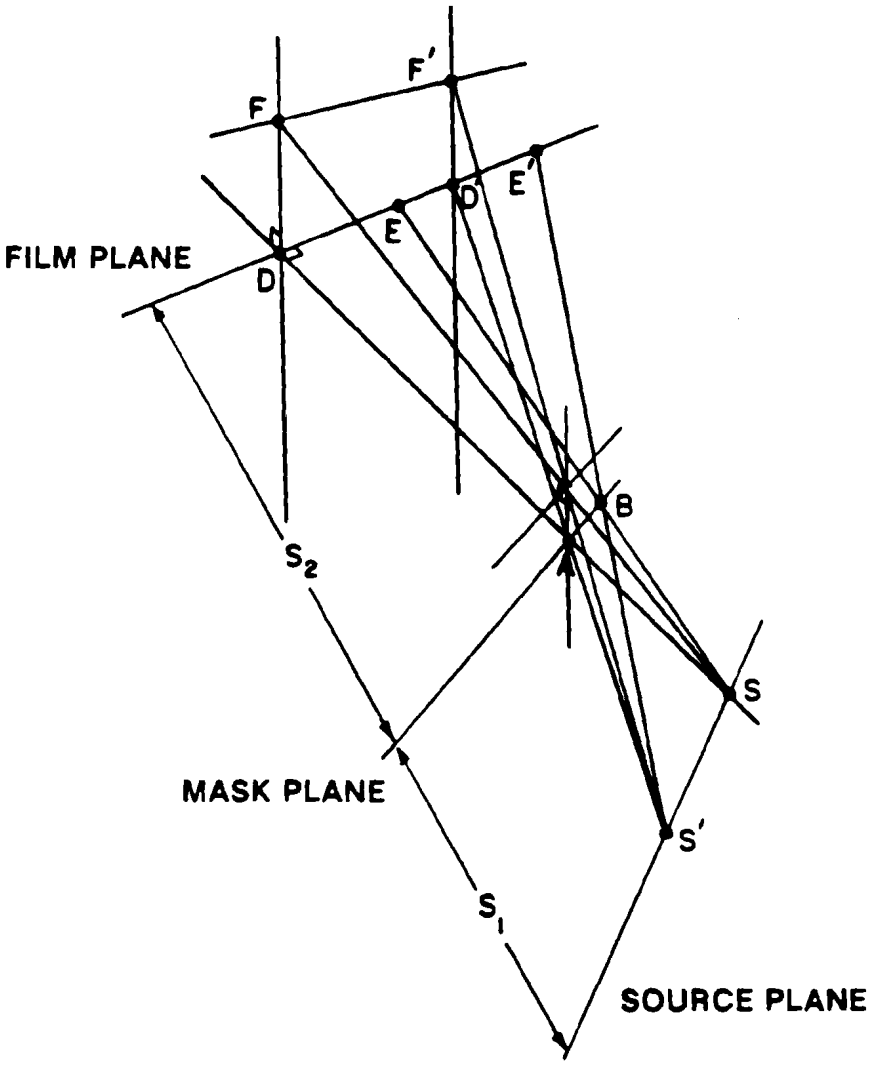

Fig. 2.2.2
Explanation of how 2 projections from two point sources S, S', of the same aperture produce the same shadows. $\Delta S'BA \sim \Delta S'E'D'$; $\Delta SBA \sim \Delta SED$ but AB is common to both cases so $\overline{DE} = \overline{D'E'}$.

$$E(X) = \frac{1}{\lambda^2} \int_{-\infty}^{\infty} E(\alpha)\ \sqrt{M(\xi)}\ \frac{e^{iK[r(\xi,\alpha) + r(\xi,X)]}}{r(\xi,\alpha) \cdot r(\xi,X)}\ d\alpha d\xi \qquad (2.2.3)$$

Let us use the following assumptions:

(1) $r(\xi,\alpha)\ r(\xi,X)$ in the denominator change slowly compared to the exponent and can be taken outside the integral, and written as S_1 and S_2 .

(2) The paraxial approximation is valid and for $r(\xi,\alpha)$ and $r(\xi,X)$ we retain only the first order term.

We then can write (2.2.3) as:

$$E(X) = c' \int_{-\infty}^{\infty} E(\alpha)\ \sqrt{M(\xi)}\ e^{iK\left[\frac{\alpha^2}{2S_1} + \frac{\xi^2}{2}\left(\frac{1}{S_1} + \frac{1}{S_2}\right) - \xi\left(\frac{\alpha}{S_1} + \frac{X}{S_2}\right)\right]}\ d\alpha d\xi \qquad (2.2.4)$$

where $c' = [\text{phase factor}]/\lambda^2 S_1 S_2$.

We are interested in the intensity in the plane X:

$$I(X) \propto \langle E(X)\ E^*(X) \rangle \qquad (2.2.5)$$

where $\langle\ \rangle$ denotes ensemble average.

(2.2.5) is a special case of the general mutual intensity function:

$$\Gamma(X_1, X_2) = \langle E(X_1)\ E^*(X_2) \rangle \qquad (2.2.6)$$

and $I(X) = \Gamma(X,X)$. Substituting for $E(X_1)$ and $E(X_2)$ from (2.2.4) into (2.2.6) we can find the rule for the propagation of the mutual intensity in terms of its value at the source

$$\Gamma(\alpha_1,\alpha_2) = \langle E(\alpha_1)\, E^*(\alpha_2)\rangle \tag{2.2.7}$$

Although in general $\Gamma(\alpha_1,\alpha_2)$ may have a finite width we will simplify the derivation by assuming:

$$\Gamma(\alpha_1,\alpha_2) = I(\alpha)\, \delta(\alpha_1 - \alpha_2) \tag{2.2.8}$$

This is a nonphysical assumption even for a black body source (where the width of the coherence function is of the order of the average wavelength of radiation emitted from this source) and it is used only to facilitate the calculation. Using (2.2.4) - (2.2.8) we can write the intensity as follows:

$$I(X) = c' \int I(\alpha) \left| \left[\int \sqrt{M(\xi)}\; e^{iK\left[\frac{1}{2}\left(\frac{1}{S_1}+\frac{1}{S_2}\right)\xi^2 - \xi\left(\frac{\alpha}{S_1}+\frac{X}{S_2}\right)\right]} d\xi \right]^2 \right| d\alpha \tag{2.2.9}$$

The quantity in the square brackets is the diffraction pattern of the mask from a point source α. We are interested in the geometrical optics limit which is expressed as the limit

$$\lambda \to 0 \quad \text{or} \quad K \to \infty \tag{2.2.10}$$

In this case the stationary phase method (Ref. [2.2.5]) can be used to evaluate (2.2.9). The phase term is:

$$\phi(\xi) = \frac{1}{2}\mu\xi^2 - \xi\left(\frac{\alpha}{S_1}+\frac{X}{S_2}\right)+ S_1+S_2 + \frac{\alpha^2}{2S_1} + \frac{X^2}{2S_2} + \ldots \qquad (2.2.11)$$

where $\mu = \left(\frac{1}{S_1} + \frac{1}{S_2}\right)$. The term in the brackets in (2.2.9) is written as:

$$I(K) = \int_a^b g(\xi)\, e^{iK\phi(\xi)}\, d\xi \qquad (2.2.12)$$

where $g(\xi) = \sqrt{M(\xi)}$ and ξ is a one-dimensional quantity. From Ref. [2.2.6] we may approximate (2.2.12) by

$$I(K) \sim \sqrt{\frac{2\pi}{K\phi''(\xi_o)}}\, g(\xi_o)\, e^{iK\phi(\xi_o)}\, e^{\pm i\frac{\pi}{4}} + \frac{1}{K}\left[\frac{g(b)}{\phi'(b)}\, e^{iK\phi(b)} - \frac{g(a)}{\phi'(a)}\, e^{iK\phi(a)}\right] + \ldots \qquad (2.2.13)$$

where $\phi'(\xi_o) = 0$; $\phi''(\xi_o) \neq 0$; $\phi'(a) \neq 0$; $\phi'(b) \neq 0$ and where $\phi'(\xi_o)$ and $\phi''(\xi_o)$ are the first and second derivatives with respect to ξ, evaluated using the leading terms in the expansion for the phase (2.2.11). We take the + sign for $\phi''(\xi_o) > 0$ and the - sign for $\phi''(\xi_o) < 0$. a and b are the boundaries of the aperture.

The first term in (2.2.13) describes the geometrical shadow while the second term denotes the contributions from diffraction. We will now evaluate the first term explicitly.

From $\phi'(\xi_o) = 0$ we get

$$\xi_o = \frac{1}{\mu}\left(\frac{\alpha}{S_1} + \frac{X}{S_2}\right) . \qquad (2.2.14)$$

Also $\phi''(\xi_o) = \mu$. Let us denote the one-dimensional intensity by I^1 and the two-dimensional intensity by I^2. From (2.2.9), (2.2.12) and (2.2.13) we have

$$I^1(X) = \frac{c'}{\lambda\mu}\int_{-\infty}^{\infty} I^1(\alpha)\, M(\xi_o)\, d\alpha \qquad (2.2.15)$$

In the two-dimensional case the constant outside the integral is $\left(\sqrt{\frac{\lambda}{\mu}}\right)^2$ and so, substituting for c' from (2.2.4), we get

$$I^2(X) = \frac{1}{\lambda^2}\left(\frac{2\pi}{K\mu}\right)^2 \frac{1}{(S_1S_2)^2}\int_{-\infty}^{\infty} I^2(\alpha)\, M(\xi_o)\, d\alpha$$

$$= \frac{1}{(S_1+S_2)^2}\int_{-\infty}^{\infty} I^2(\alpha)\, M(\xi_o)\, d\alpha \qquad (2.2.15a)$$

This is the result used in Ref. [2.2.1] p. 33.

This result is often quoted in pseudoholography: the intensity on the film plane is given by the convolution of the source function and the mask function. However, the condition $\lambda \to 0$ is usually true only for nuclear radiation, nuclear particles and very hard x-ray radiation. The x-rays emitted from laser produced plasmas are typically in the region 1 - 8Å and therefore diffraction effects may not be negligible. Let us now examine the second term in (2.2.13). To

simplify matters the calculation will be one-dimensional.

Consider the simple case of a slit on axis as in Fig. 2.2.3. The symmetry in this example allows us to get $g(a) = g(-b)$ where a, b are the slit boundaries. Also, from (2.2.11) we get:

$$\begin{aligned}
\phi(a) &= S_1 + S_2 + \frac{\mu a^2}{2} - a\left(\frac{\alpha}{S_1} + \frac{X}{S_2}\right) + \frac{\alpha^2}{2 \cdot S_1} + \frac{X^2}{2 \cdot S_2} \\
\phi(-a) &= S_1 + S_2 + \frac{\mu a^2}{2} + a\left(\frac{\alpha}{S_1} + \frac{X}{S_2}\right) + \frac{\alpha^2}{2 \cdot S_1} + \frac{X^2}{2 \cdot S_2} \\
\phi'(a) &= \mu a - \left(\frac{\alpha}{S_1} + \frac{X}{S_2}\right) \\
\phi'(-a) &= -\mu a - \left(\frac{\alpha}{S_1} + \frac{X}{S_2}\right)
\end{aligned} \tag{2.2.17}$$

Using the above approximation the second term in (2.2.13) can be written as:

$$\frac{1}{K} \frac{g(a)}{\phi'(a)} e^{iK\phi(a)} \cdot \left\{ 1 - \frac{\phi'(a)}{\phi'(-a)} e^{iK[\phi(-a) - \phi(a)]} \right\} \tag{2.2.18}$$

where $g(\xi) = \sqrt{M(\xi)}$ and the factor $1/(r(\xi,x)\, r(\xi,\alpha))$ was taken outside the integral as before. Since $\phi'(a) \neq 0$ and $\phi'(-a) \neq 0$, (2.2.18) does not hold at the boundary of the geometrical shadow. Assuming $\alpha = 0$ for simplicity and using (2.2.17) we get

$$\phi(-a) - \phi(a) = \frac{2aX}{S_2}$$

$$\frac{\phi'(a)}{\phi'(-a)} = \frac{\frac{X}{S_2} - \mu a}{\frac{X}{S_2} + \mu a} \equiv B(X) \tag{2.2.19}$$

Let us divide the discussion into the two regions in Fig. 2.2.3. Region I is the geometrical shadow region and region II is the illuminated region.

In region II, $\frac{\phi'(a)}{\phi'(-a)} << 1$ near the boundary. We thus can neglect this term. From (2.2.13) and (2.2.18) using the fact that $g(a) \sim g(\xi_o)$ near the boundary and that $\phi''(\xi_o) = \mu$, we have in region II

$$I(K) \sim g(\xi_o)\sqrt{\frac{2\pi}{K\mu}}\, e^{iK\phi(\xi_o)} \left\{ 1 + \frac{1}{\sqrt{\frac{2\pi}{K\mu}}\, K(a\mu - \frac{X}{S_2})}\, e^{iK\left[\phi(a) - \phi(\xi_o)\right]} \right\} \tag{2.2.20}$$

Using (2.2.17), $\alpha = 0$. Substituting for ξ_o from (2.2.14) and denoting $\frac{R(X)}{\sqrt{K}} = \frac{1}{\sqrt{\frac{2\pi}{K\mu}}\, K(a\mu - \frac{X}{S_2})}$, the intensity in region II near the boundary can be written from (2.2.9) as

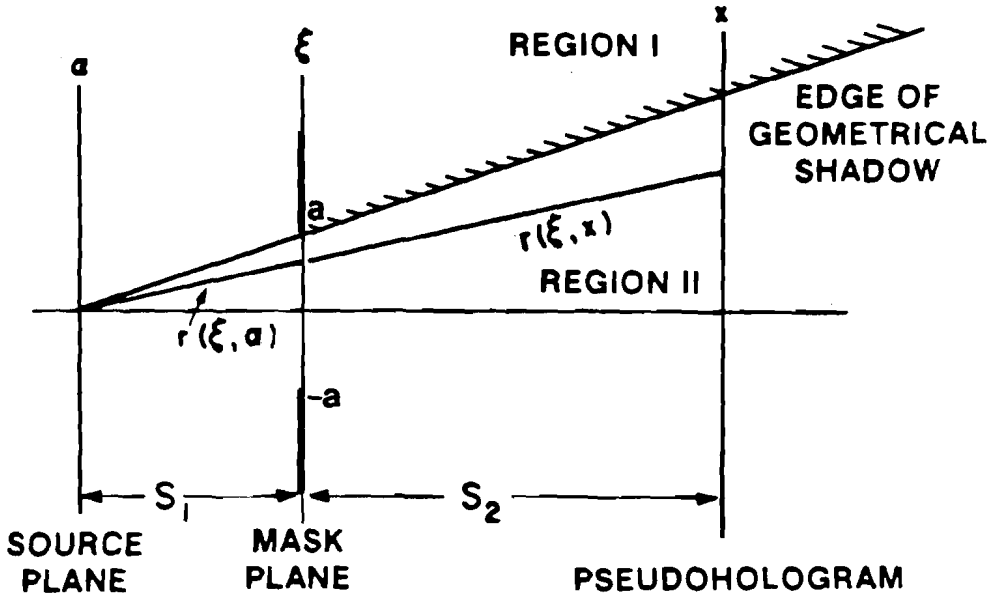

Fig. 2.2.3
Notation for stationary phase calculation of the diffraction pattern from a slit.
$r(\xi,a) = [(\xi-a)^2 + S_1^2]^{1/2}$; $r(\xi,x) = [(\xi-x)^2 + S_2^2]^{1/2}$.
In a typical experiment:
Max $\{a\} \leq 10^{-2}$cm; Max $\{a\} < 5 \times 10^{-4}$cm; $S_1 \sim 1$ cm;
$S_2 \sim 16$ cm.

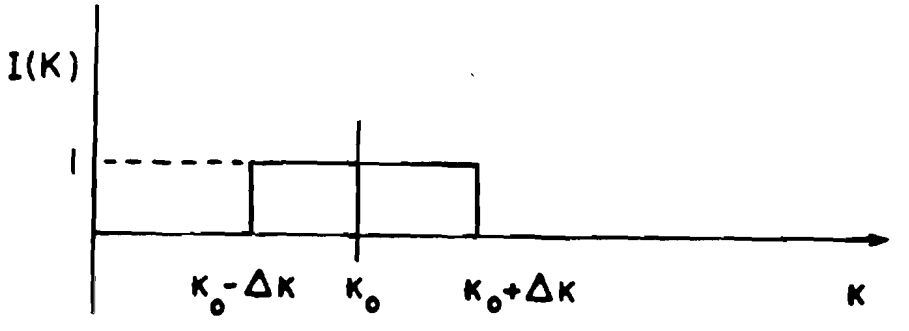

Fig. 2.2.4
An approximation for the spectrum of x-rays emitted from laser produced plasma. K = wave number, I(K) = normalized intensity distribution.

$$I(X) = c'(I(K)\, I^{*}(K)) \qquad (2.2.21)$$

$$= c''\left\{1 + \frac{R^2(X)}{K} + \frac{2R(X)}{\sqrt{K}} \cos\left[K\left(\frac{\mu a^2}{2} + \frac{X^2}{2\mu S_2^2} + \frac{aX}{S_2}\right)\right]\right\}$$

where c', c'' are constants independent of K.

In region I the first order of (2.2.13) vanishes identically and we are left with the second order terms in (2.2.18). We then have:

$$I(X) = \frac{c'''}{K}\left[1 + B^2(X) + 2B(X) \cos\left(\frac{2KaX}{S_2}\right)\right] \qquad (2.2.22)$$

The constants and the power of K used in (2.2.21) and in (2.2.22) are for the two-dimensional case although the expression (2.2.20) is for the one-dimensional case. This is a simplification that will give us some indication of the real case.

Until now only monochromatic light was assumed. In a real plasma the spectrum is very complicated and contains characteristic lines as well as a continuous spectrum. Again, to simplify we assume a spectral distribution as shown in Fig. 2.2.4. Expressions (2.2.21) and (2.2.22) must be integrated over the range $[K_0 - K, K_0 + K]$. The terms involving Cos function are difficult to integrate and to

put in closed form. While they can be written as an infinite series, they are difficult to visualize. However, from (2.2.21) and (2.2.22) we see that integrating the cos function will tend to smooth out the fluctuations so that the shadow will be smoother than the typical Fresnel diffraction pattern of a slit (as in Ref. [2.2.7] for example). Hence the shadows cast by a broadband source will approximate the mask more faithfully than those cases with monochromatic radiation.

The expressions (2.2.21) and (2.2.22) could be computed numerically. The results would give us the shape of the recorded zones and, by Fourier Transform, the efficiency at higher orders could be calculated. We might then determine which configuration would still give an appreciable efficiency at higher orders.

A second method would be to numerically propagate a spherical wave through the mask to a film plane and to compute the intensity transmittance. We would then numerically reconstruct the pseudohologram with an incident plane wave and compute the intensities at all orders. We could thus determine the configuration with which higher orders are still useful. However, as will be explained later, this is a very difficult calculation because we need to perform operations with vectors with much more than 30,000 elements. To simulate the experimental conditions we would need to simulate polychromatic radiation in the calculation. This means repeating the above procedure for different wavelengths. These procedures must be employed if an accurate criterion is needed for closing the width of the outermost zone in a given pseudoholographic configuration.

Instead, we may develop a rough rule of thumb for determining the

maximum wavelength which is useful in a given setup. From the geometry illustrated in Fig. 2.2.5 we may define a quantity Δv,

$$\Delta v = r\left[\frac{2\mu}{\lambda}\right]^{\frac{1}{2}} \tag{2.2.23}$$

where $\mu = \frac{1}{S_1} + \frac{1}{S_2}$ and r is the slit width. From Ref. [2.2.7] p. 194 $(\Delta v)^2 = 14$ is an acceptable criterion to avoid diffraction so that when $\mu = \frac{1}{S_1} + \frac{1}{S_2} \approx 1\ cm^{-1}$ we get from (2.2.23)

$$\lambda \leq \frac{r^2}{7}\ \text{Å} \tag{2.2.24}$$

where r is in μm. The criterion (2.2.24) is more stringent for reconstruction at higher orders than in the first order. For each order p, Δv must be chosen so that the reconstructed intensity at this order will be appreciably larger than the noise. For third order reconstructions $(\Delta v)^2 = 16$ seems to be acceptable by considering Ref. [2.2.7] p. 194, and so we require $\lambda \leq \frac{r^2}{8}$ Å for third order reconstruction.

2.2.2 High Order Reconstruction of a Pseudohologram.

Using the zone plate in the coded aperture mode in first order reconstruction gives a resolution comparable to that of the pinhole camera, where the pinhole diameter is approximately equal to the width of the outermost zone. It has been shown (see Ref. [2.2.14]) that for simple objects, there is a net gain in signal to noise ratio in the zone plate coded aperture mode. However, this gain is not critical for imaging laser produced plasmas because the x-ray intensity is so great that it does not represent an exposure limita-

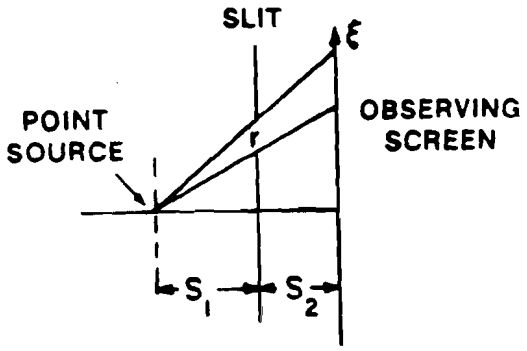

Fig. 2.2.5
Notation for Fresnel propagation calculation through a slit of width r.

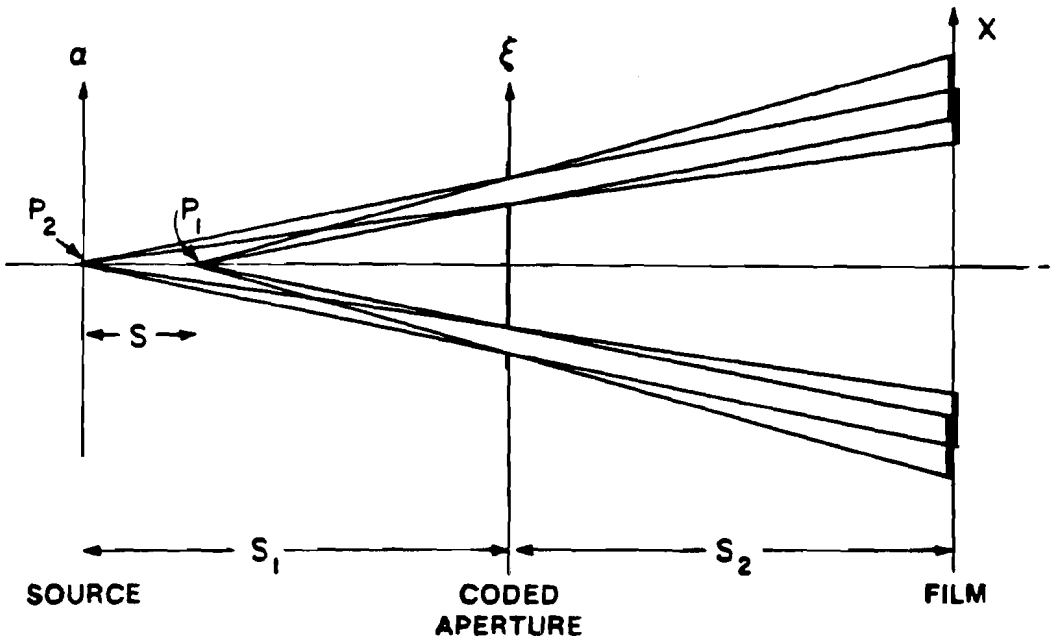

Fig. 2.2.6
Illustration of recording depth information with a coded aperture.
$I(\alpha, s)$ = intensity source distribution
$M(\xi)$ = mask function at
$I(x)$ = intensity distribution in the film plane in no. photons/area
A point closer to the coded aperture (P_1) forms a larger shadow than that from P_2.

tion in the pinhole camera. Furthermore, as will be discussed later, this net gain in pseudoholography decreases as the number of resolvable elements increases. There is a limited usefulness to the tomographic capability of pseudoholography. Finally, it is a two-step process. It thus seems that in view of the simplicity of the pinhole camera there is no point in using pseudoholography. However, we find that a strong justification for using this technique is the possibility of achieving a resolution in higher order reconstructions which is not achievable with other techniques such as the pinhole camera, zone plate imaging, or the x-ray microscope. To display this important advantage it is, therefore, necessary to rederive all the quantities previously given in Ref. [2.2.1] for first order reconstructions. This will enable us to calculate the efficiencies and the effects of noise at higher orders.

Consider the system in Fig. 2.2.6. In a real situation the problem of recording a pseudohologram is a three-dimensional problem since depth information is registered, too. To simplify the treatment, we assume a plane source. From Eq. (2.2.9) we have for the intensity at the recording film plane (here the coordinates α,ξ and X are symbolically two-dimensional)

$$I(X) = c \int_{-\infty}^{\infty} I(\alpha)\, G(\alpha + dX)\, d\alpha \qquad (2.2.25)$$

where

$$G(\alpha + dX) = \left| e^{-i\left(\frac{h}{\mu}\right)^2} \int \sqrt{M(\xi)}\, e^{iK\left(\xi + \frac{h}{\mu}\right)^2} d\xi \right|^2 \qquad (2.2.26)$$

$$h = S_1 + \frac{S_1}{S_2} X \quad \text{and} \quad d = \frac{S_1}{S_2} .$$

In the case $\lambda \to 0$, (2.2.26) is given by:

$$G(\alpha + dX) = M(\alpha + dX) \qquad (2.2.27)$$

$M(\xi)$ is the intensity transmittance of the zone plate mask. In the ξ^2 domain it is a periodic function, and therefore $G(\xi^2)$is a periodic function. We can therefore use a Fourier series to express this function. Let ξ be a normalized coordinate (i.e. $\xi = \xi'/\xi_1$ where ξ' is the unnormalized coordinate and ξ_1 is the radius of the innermost zone); we can write:

$$M(\xi^2) = \sum_{p=-\infty}^{\infty} C_p\, e^{-ip\pi\xi^2} \cdot \mathrm{Circ}\left[\xi;\xi_N\right] \qquad (2.2.28)$$

Let $\theta=\xi^2$; then

$$C_p = \int_0^{2\pi} G(\theta)\, e^{ip\pi\theta}\, d\theta \qquad (2.2.29)$$

These are the same integrals we dealt with in section 2.1, and examples are given in Table 2.1.1, and Fig. 2.1.4. We now substitute (2.2.28) in (2.2.25) using (2.2.15a) to get (for two-dimensional coordinates)

$$I(X) = \int_{-\infty}^{\infty} I(\alpha) \sum_{p=-\infty}^{\infty} C_p \, e^{-i\pi p\left[\frac{\frac{1}{\mu}\left(\frac{\alpha}{S_1}+\frac{X}{S_2}\right)}{\xi_1}\right]^2} \cdot \text{Circ}\left\{\left[\frac{1}{\mu}\left(\frac{\alpha}{S_1}+\frac{X}{S_2}\right)\right];\ \xi_N\right\} d\alpha \qquad (2.2.30)$$

where ξ_1 is the radius of the innermost zone, $\mu = \frac{1}{S_1} + \frac{1}{S_2}$,

$\text{Circ}\left\{\left[\frac{1}{\mu}\left(\frac{\alpha}{S_1}+\frac{X}{S_2}\right)\right];\ \xi_N\right\}$ is a circle of radius ξ_N, and the coordinate is $\xi = \frac{1}{\mu}\left(\frac{\alpha}{S_1}+\frac{X}{S_2}\right)$ and N is the number of zones. I(X) of (2.2.30) is recorded on the film and processed with a certain γ. (The slope of H&D curve, see Ref. [2.2.9].) The amplitude transmittance of the pseudohologram is therefore

$$T = t_o \, I(X)^{-\gamma/2} \qquad (2.2.31)$$

The reconstructed field is given by the Fresnel integral where (2.2.31) is the input function. Let X_r be in the reconstruction plane; then:

$$E(X_r) = \frac{e^{ikZ}}{i\lambda Z} \int_{-\infty}^{\infty} \left\{ \sum_{p=-\infty}^{\infty} C_p \int_{-\infty}^{\infty} I(\alpha)\, e^{-ip\pi\left(\frac{\xi_o}{\xi_1}\right)^2} \text{Circ}\left[\xi_o;\ \xi_N\right] d\alpha \right\}^{-\gamma/2} \cdot e^{\frac{ik}{2Z}(X_r - X)^2} dX \qquad (2.2.32)$$

Only the case $\gamma = -2$ will be considered here. For all the other cases

$\gamma = -2 + d$ and the expression in the large brackets in (2.2.32) can be written as a product of

$$\left[\sum_p C_p \int \ldots d\alpha\right]^{-\gamma/2} \cdot \left[\sum_p C_p \int \ldots d\alpha\right]^{-d/2}$$

Since the Fresnel transformation of products is equal to the convolution of the transforms, Eq. (2.2.32) will be written in the general case as a convolution. Rearranging (2.2.32) we can see that the terms containing X^2 will vanish if Z has the following form:

$$Zp = \frac{1}{p}\frac{\xi_1^2}{\lambda}\left(\frac{S_1 + S_2}{S_1}\right)^2 \qquad (2.2.33)$$

These are the locations of the pth order images. From (2.2.32) and (2.2.33) after algebraic manipulations we get

$$E(X_r) = \sum_{p=-\infty}^{\infty} C_p \frac{e^{iKZ}}{i\lambda Zp} \int_{-\infty}^{\infty} d\alpha\, I(\alpha)\, e^{-\frac{i\pi}{\lambda Zp}\left[-X_r^2 + \left(\frac{S_2}{S_1}\alpha\right)^2\right]} \cdot$$

$$\int_{-\infty}^{\infty} \mathrm{Circ}\left[\frac{1}{\mu}\left(\frac{\alpha}{S_1} + \frac{X}{S_2}\right);\ \xi_N\right] \cdot e^{-\frac{2\pi i}{\lambda Z}\left(X_r + \frac{S_2}{S_1}\alpha\right)X}\, dx \qquad (2.2.34)$$

changing-variables to $t = \frac{1}{\mu}\left(\frac{\alpha}{S_1} + \frac{X}{S_2}\right)$ the integration over X is recognised

as the Bessel function of order 1. Denoting the integral over X by $h(\alpha;X_r;p)$ we can thus write:

$$h(\alpha,X_r,p) = 2\pi\, e^{\frac{i\pi}{\lambda Z_p}\left(X_r+\frac{S_2}{S_1}\alpha\right)^2} \frac{J_1\left[\frac{S_2\mu\cdot 2\pi\,\xi_N}{\lambda Z_p}\left(X_r+\frac{S_2}{S_1}\alpha\right)\right]}{\frac{2\pi S_2\mu}{\lambda Z_p}\left(X_r+\frac{S_2}{S_1}\alpha\right)} \tag{2.2.35}$$

(2.2.34) can then be written as:

$$E(X_r) = \sum_{p=-\infty}^{\infty} \frac{C_p\, e^{iKZ_p}}{\lambda Z_p} \int_{-\infty}^{\infty} d\alpha\; I(\alpha)\cdot h(\alpha,X_r,p) \tag{2.2.36}$$

But $Z_p = Z_1/p$; therefore, from (2.2.35) we get the important result for the point spread function $h(\alpha,X_r,p)$ that it becomes narrower at larger values of p. (i.e. at higher orders).

It is important to note that the present discussion is useful only if the contributions from other foci can be neglected when we deal with a specific focus. Because the field is an infinite sum as is seen in (2.2.34), the expression for the point spread function in Eq. (2.2.35) is only an approximation. In a different derivation (see Ref. [2.1.18]) an expression is derived from which it is clear that the point spread function is not a Bessel function. Only in the limit $N \to \infty$ can we replace it by a Bessel function (or sinc function in case of a one-dimensional zone plate). In our experiment $N \sim 40$ and so this approximation is quite good.

2.2.3 Transverse and Axial Widths of the Point Spread Function.

It is sometimes required to demagnify the pseudohologram before reconstruction to get a convenient focal length. Let $\frac{1}{m}$ be the demagnification in Eq. (2.2.30). I(X) changes to I(mx); this will change Zp to $Z(p, m) = \frac{Zp}{m^2}$. The new expression for the point spread function including demagnification is therefore

$$h(\alpha, X_r, p, m) = \tag{2.2.37}$$

$$2\pi\, e^{\frac{i\pi \cdot pm^2}{Z_1}\left(X_r + \frac{S_2}{S_1}\alpha\right)^2} \frac{J_1\left[\frac{2\pi p m^2 \mu S_2}{\lambda Z_1}\left(\frac{X_r}{m} + \frac{S_2}{S_1}\alpha\right)\xi_N\right]}{\frac{2\pi p m^2 \mu S_2}{\lambda Z_1}\left(\frac{X_r}{m} + \frac{S_2}{S_1}\alpha\right)}$$

Using the fact that the first zero of the Bessel function is at an argument of 3.817 we get:

$$\Delta X_r = \frac{3.817}{2\pi}\frac{\lambda Z_1}{S_2}\frac{1}{pm}\frac{1}{\xi_N} \tag{2.2.37a}$$

for the transverse width when $\alpha = 0$.

For the axial width we assume $I(\alpha) = I_o\delta(\alpha)$ and $X_r = 0$ so that (2.2.32) can be rewritten as:

$$I = \left| I_o \int e^{-ip\pi \left(\frac{X}{\mu\xi_1 S_2}\right)^2} \text{Circ}\left[\left(\frac{X}{\mu S_2}\right)^2 ; \xi_N^2\right] e^{\frac{iKX^2}{2Z}} dX \right|^2$$

$$= \left| I_o \int \text{Circ}[t ; \xi_N^2] \, e^{-2\pi i t u} \, dt \right|^2 \qquad (2.2.38)$$

where $u = \frac{p}{(\xi_1 \mu S_2)^2} + \frac{1}{\lambda Z}$ and $t = x^2+y^2$. In this expression $\bar{x}=(x,y)$ is a two-dimensional quantity. From (2.2.38) we have:

$$|I| = \left| \frac{\sin(\pi u \xi_N^2)}{\pi u} \right|^2 \qquad (2.2.39)$$

The foci are again at u=0 or Z=Zp. Also $u = \frac{1}{\lambda}\left(\frac{1}{Zp} - \frac{1}{Z}\right)$ so that near the focus $\frac{1}{Zp} - \frac{1}{Z} \simeq \frac{\Delta Z}{Zp^2}$. Hence $u = \frac{\Delta Z}{\lambda Zp^2}$ and (2.2.39) can be written as:

$$|I| = \left| \frac{\sin\left[\frac{\pi}{\lambda}\left(\frac{\xi_N}{Zp}\right)^2 \Delta Z\right]}{\frac{\pi}{\lambda}\frac{\Delta Z}{Zp^2}} \right|^2 \qquad (2.2.40)$$

The depth of focus is found using the quarter wave criterion. From (2.2.40) $\frac{\pi}{\lambda}\left(\frac{N}{Zp}\right)^2 \Delta Z = \frac{\pi}{2}$ hence

$$\Delta Zp = \frac{\lambda}{2}\left(\frac{Zp}{\xi_N}\right)^2 \qquad (2.2.41)$$

If demagnification is introduced then (2.2.30) changes from I(X) to I(mX). Eq. (2.2.38) will change also yielding a new expression for u:

$$u = \frac{1}{\lambda}\left(\frac{pm^2\lambda}{(\xi_1\mu S_2)^2} - \frac{1}{Z}\right) \tag{2.2.42}$$

and finally:

$$\Delta Z(p,m) = \frac{\lambda}{2}\left(\frac{Zp}{m}\frac{1}{\xi_N}\right)^2 = \frac{\Delta Zp}{m^2} = \frac{\Delta Z}{p^2m^2} \tag{2.2.43}$$

Let ξ_N be the radius of the outermost zone; r the width of the outermost zone, N the number of zones, ξ_1 the radius of the innermost zone, and Z_1 the primary focal length. We know

$$\begin{aligned} \xi_N &= \sqrt{N}\,\xi_1 = \sqrt{NZ_1\lambda} \\ \xi_N &= 2Nr \quad \text{for} \quad N > 10 \\ Z_1 &= \frac{\xi_1^2}{\lambda} \end{aligned} \tag{2.2.44}$$

Using (2.2.44), (2.2.33) and (2.2.43) we obtain the widths of the points spread function:

$$\Delta X_r = 1.22r\left(\frac{S_1 + S_2}{S_1}\right)\frac{1}{pm} \tag{2.2.45}$$

$$\Delta Z = 0.5\,\xi_1^2\left(\frac{S_1 + S_2}{S_1}\right)^2 \cdot \frac{1}{p^2m^2N\lambda} \tag{2.2.46}$$

2.2.4 The Transverse Resolution in the Zone Plate Pseudoholographic Technique.

In the first step of the coded pseudoholography technique, which

is illustrated in Fig. 2.2.7, every luminous point in the source (i.e., in the plasma), casts a shadow of a Fresnel zone plate onto a piece of photographic film. In the second step, which is illustrated in Fig. 2.2.8, the exposure is processed, conveniently reduced, and illuminated by a coherent beam of light. A reconstructed image is produced at a series of foci, F_p.

In order to derive an expression for the definition of the two-step pseudoholographic process, consider the system described in Figs. 2.2.7 and 2.2.8. Let $T=\overline{AB}$ be the finest resolved element in the object, S_1 the distance from the object to the mask, which is a Fresnel zone plate, and S_2 the distance from the mask to the film.

In the first step the shadow of the zone plate is cast on the film by each point source, and hence produces two zone plates separated by the distance $T' = \overline{A'B'}$ on the pseudohologram. When the processed pseudohologram is reduced to yield a convenient focal length, the separation is T", as shown in Fig. 2.2.9. In the second step each zone plate focuses the reconstruction beam to a series of foci. If we choose T" to be such as to cause the corresponding reconstructed point sources to be resolved according to the Sparrow criterion, we have from Ref. [2.2.10] that

$$T'' = 1.46\lambda(1/\Omega) \qquad (2.2.47)$$

where λ is the wavelength of the reconstruction beam and Ω is the cone angle of the focussed beam at the primary focus. Let us denote by ξ_N and r the radius and the width of the outermost zone, respectively, of the original zone plate. We will denote by ξ'_N and r' the corresponding

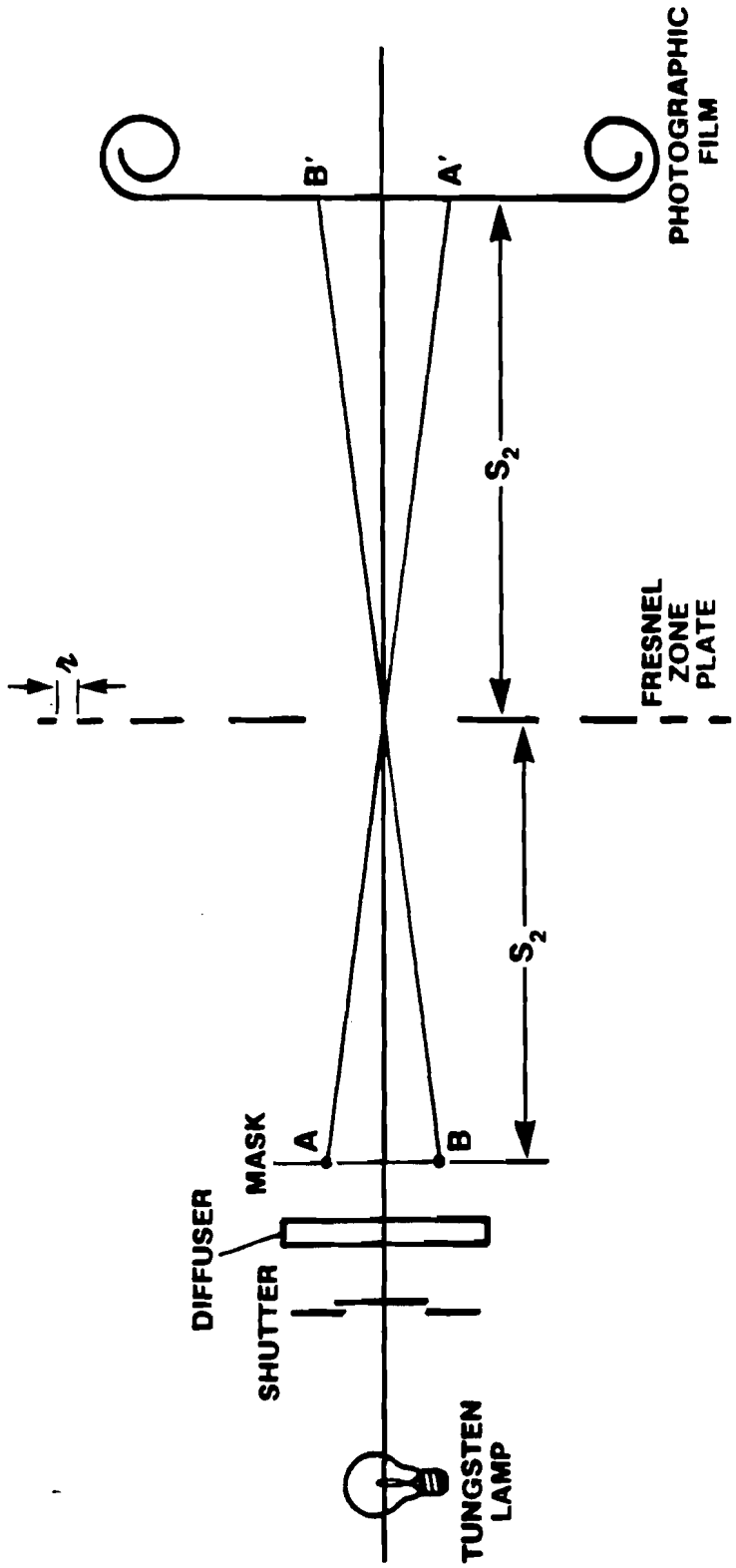

Fig. 2.2.7
The recording step of the pseudoholographic technique. r is the outermost zone. A', B' are centers of two zone plate shadows.

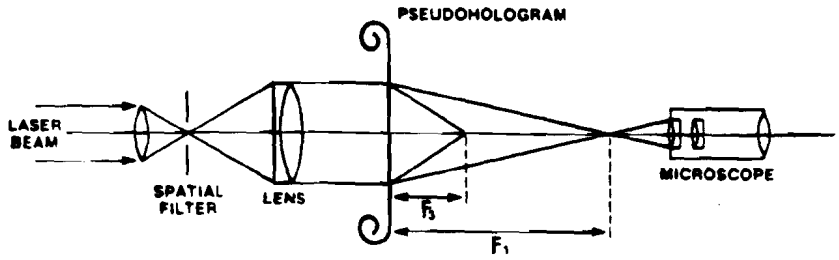

Figure 2.2.8
The reconstruction of a pseudohologram. F_1 and F_3 are the first and third order foci respectively.

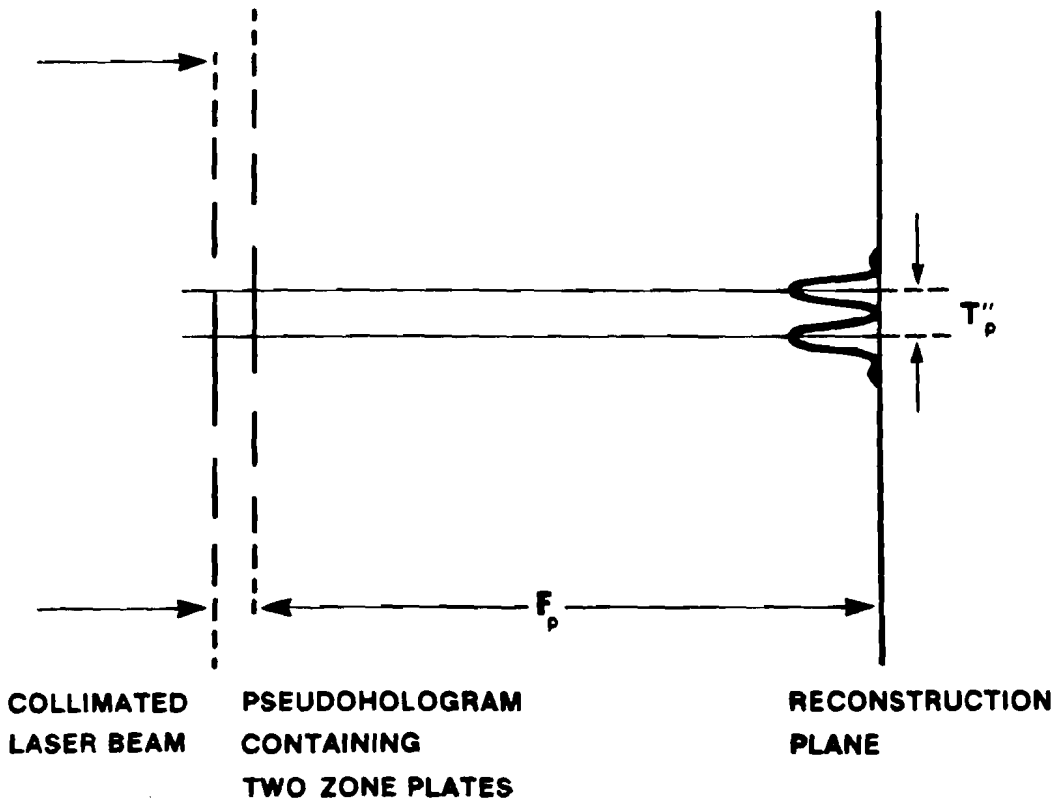

Figure 2.2.9
Explanation of the reconstruction step. Each zone plate recorded on the pseudohologram focuses the light at its own focal point.

quantities on the recorded pseudohologram, and by ξ_N'' and r'' those on the reduced pseudohologram. From (2.2.44) we have:

$$\xi_N = 2rN \tag{2.2.48}$$

Also, from geometrical considerations it can be shown that

$$\xi_N' = \xi_N \frac{(S_2 + S_1)}{S_1} \tag{2.2.49}$$

Denoting the demagnification by 1/m, then

$$\xi_N'' = \xi_N'/m \tag{2.2.50a}$$

$$T'' = T'/m \tag{2.2.50b}$$

From Figs. 2.2.7 and 2.2.9 and from Eq. (2.2.50) we get

$$T'' = T\left(\frac{S_1}{S_2}\right)\left(\frac{1}{m}\right) \tag{2.2.51}$$

Since for zone plates employed as a lens in the visible $\xi_N'' = \sqrt{NF}$, then $F = \xi_N''^2/N\lambda$ and, therefore,

$$1/\alpha = \frac{F}{2\xi_N''} = \xi_N''/2N\lambda \tag{2.2.52}$$

From Eqs. (2.2.47) - (2.2.52) we get

$$T = 1.46\lambda(1/\Omega) \cdot \frac{S_1}{S_2} m = 1.46r\left(\frac{S_1 + S_2}{S_2}\right) \tag{2.2.53}$$

From (2.2.53) we see that the demagnification, 1/m, has no effect on the transverse resolution.

Now consider the reconstruction at higher order foci. At the pth order focus,

$$F_p = (\xi''^2_N/N)\,\frac{1}{p} \qquad (2.2.54)$$

Hence

$$(1/\Omega)p = \xi''_N/2pN \qquad (2.2.55)$$

But the distance between the reconstructed points T", remains the same; only the cone angle of the reconstructed beam gets bigger. Therefore, the only quantity in (2.2.47) that changes is $1/\Omega$, Hence:

$$T_p = \frac{1.46r}{p} \cdot \frac{S_1 + S_2}{S_2} \qquad (2.2.56)$$

This remarkable result means that by going to higher orders the definition improves significantly. The geometry can be arranged so that $S_2 >> S_1$, and so with a practical value for r of about 3μm we get:

$$T_1 = 1.46 \cdot 3 = 4.38\mu m$$

$$T_2 = \frac{1.46 \cdot 3}{3} = 1.46\mu m$$

$$T_3 = 1.46 \cdot \frac{3}{5} = 0.87\mu m$$

2.2.5 Tomographic Resolution in the Zone Plate Pseudoholographic Technique.

From Fig. 2.2.10 we obtain the following relationships:

$$\Delta\xi_N = \frac{S_1}{S_2} S \qquad (2.2.57a)$$

$$S = L \operatorname{tg}\theta \qquad (2.2.57b)$$

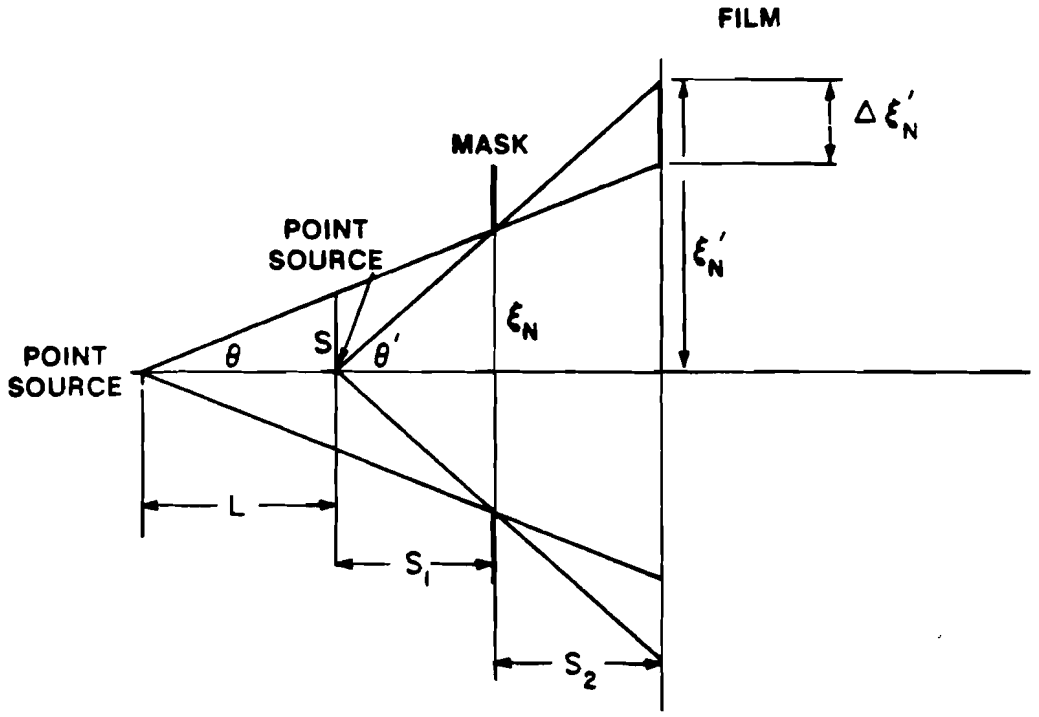

Fig. 2.2.10
Derivation of the tomographic resolution of the pseudoholographic technique.

$$tg\theta = \xi_N/(S_1 + L) \sim \xi_N/S_1 \qquad (2.2.57c)$$

For zone plates: $$Fp = F/p = \xi_1''^2/p\lambda = \xi_1'^2/m^2 p\lambda \qquad (2.2.57d)$$

Therefore $$\Delta Fp = \frac{\Delta F}{p} = \frac{2\xi_1' \Delta\xi_1'}{m^2 p\lambda} \qquad (2.2.57e)$$

From Eq. (2.2.46) $$\Delta Fp = \frac{0.5}{p^2 m^2 N\lambda} \xi_1^2 \left(\frac{S_1 + S_2}{S_1}\right)^2 \qquad (2.2.57f)$$

From Fig. 2.2.10 $$\xi_1' = \frac{S_1 + S_2}{S_1} \xi_1 \qquad (2.2.57g)$$

By equating (2.2.57e) and (2.2.57f) and from (2.2.48) we get:

$$L = \frac{0.5}{Np} \frac{S_1}{S_2} (S_1 + S_2) \qquad (2.2.58)$$

The tomographic resolution increases with the number of zones and with the order number.

2.2.6 Efficiency of Reconstructions at Higher Orders.

From Eq. (2.2.34) and (2.2.15a) the factor that determines the efficiency at the different orders is

$$\frac{Cp}{\lambda Zp} = \frac{1}{(S_1 + S_2)^2 \lambda Zp} \int_0^{2\pi} M(\theta)\, e^{i\pi p\theta}\, d\theta \qquad (2.2.59)$$

We have already seen a few examples for $M(\theta)$ in the previous section in Fig. 2.1.4. For the case of Fig. 2.1.4a $C'_p = \tilde{B}_a(u) = \frac{\text{Sin } \pi uq}{\pi u}$.

Substituting for $\pi uq = \frac{\pi}{2}(2p + 1)$ we get

$$\frac{C_p}{\lambda Z_p} = \frac{1}{(S_1 + S_2)^2 \lambda Z_p} \frac{(-1)^{p+1}}{[(2p+1)/2q]}$$

But $Z_p = \frac{Z_1}{(2p+1)}$ so that

$$\frac{C_p}{\lambda Z_p} = \frac{1}{(S_1 + S_2)^2} \frac{2q}{Z_1} \quad \text{independent of p!} \qquad (2.2.60)$$

Hence the efficiencies are equal in all orders in this case. However, as has been shown in section 2.1.8, the flux at higher orders goes as $1/p^2$.

The efficiency in higher orders is very sensitive to changes in the zone shape. In Fig. 2.1.4 there are examples where the efficiency at various order is not given by Eq. (2.2.60).

2.2.7 The Effects of Zone Width on the Effective Dynamic Range.

In Fig. 2.2.11 the effect of narrowing the zones is demonstrated. In Fig. 2.2.11 A and B, cosinusoidal zones allow only for a small number of zone systems to be recorded before the film is completely darkened. In Fig. 2.2.11 C and D narrow zones allow for a much larger number of zone systems to be recorded. Hence by narrowing the zones the effective dynamic range (or the number of point sources which can be recorded) increases. In order to be more quantitative it is useful to define a quantity C, the contrast, which is the standard deviation of the intensity fluctuations on the recording divided by the average intensity. Also it is useful to compare C_{coh} for a usual hologram made with a reference beam

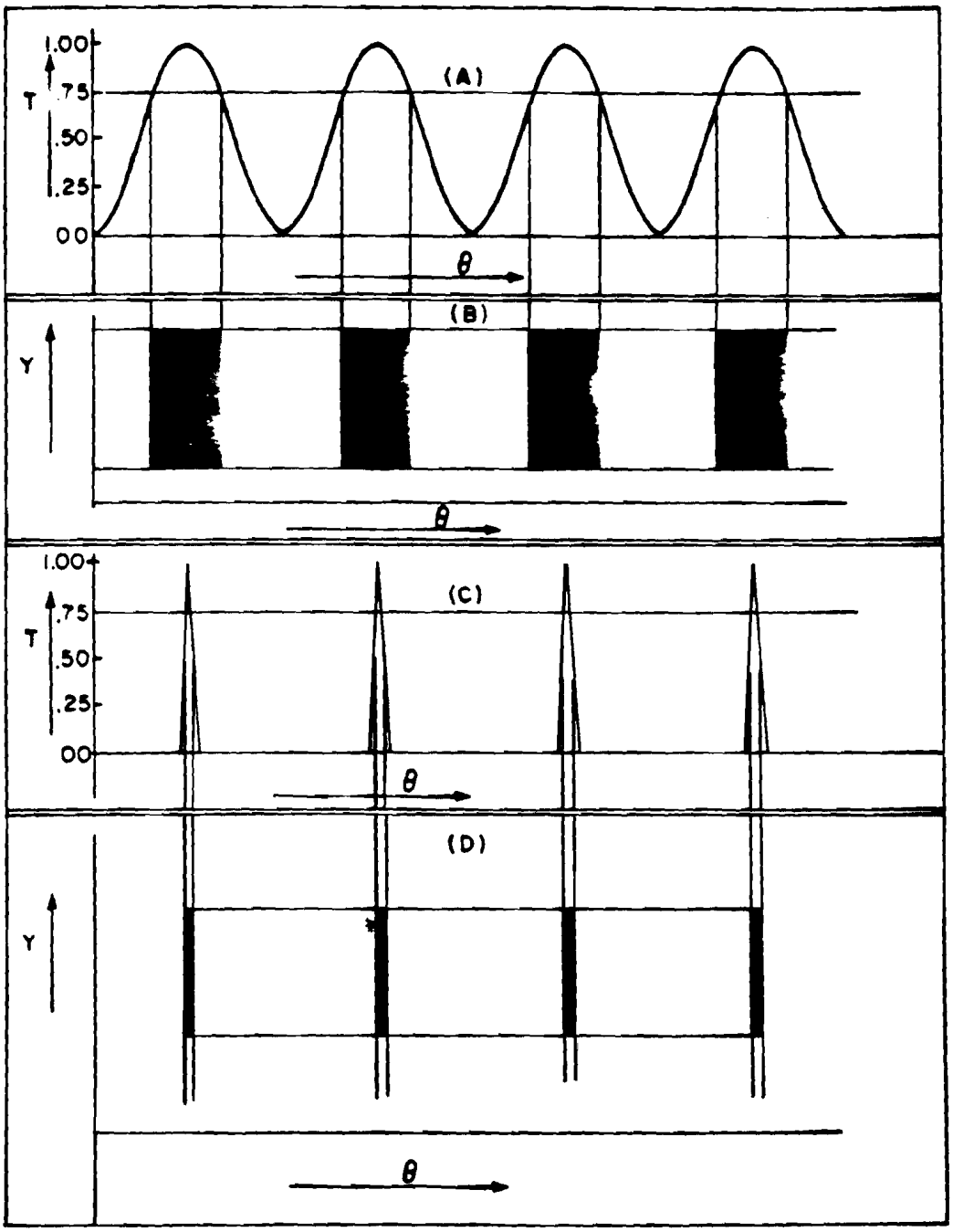

Fig. 2.2.11
(A) $\cos^2\theta$ fringes, θ = quadratic distance coordinates, T = transmission, (B) Y = distance perpendicular to the 1-D zone plate; black stripes on a high contrast processed film, (C) narrow fringes, (D) narrow stripes on the processed film.

interfering with the light scattered from the object, and C_{inc} for the pseudohologram.

Let I_{inc} and I_{coh} be the intensity distributions on the pseudohologram and on the usual hologram respectively. Let a_i and ϕ_i be the amplitude and the phase, respectively, of the field at the hologram due to the point i. It is reasonable to assume:

1. I_{inc} and I_{coh} are stationary and ergodic random processes as a function of space coordinates.
2. a_i and ϕ_j; a_i and a_j; ϕ_i and ϕ_j are uncorrelated for all $i \neq j$. a_i are Gaussian distributed random variables with zero mean.

It is then possible to show that

$$C_{coh} = 1/\sqrt{2}$$

$$C_{inc} = 1/\sqrt{N}$$

where N is the number of points to be recorded. We thus see that in the usual holography the signal to noise ratio is independent of the number of object points. Therefore, holograms of continuous objects can successfully be recorded. The signal to noise ratio in pseudoholography on the other hand is limited very strongly by N, the limiting number being approximately 200 (see Ref. [2.2.12]). Therefore discrete objects will yield a better pseudohologram than continuous objects.

Suppose, instead of having cosine shadows, we have very sharp shadows of the form of Fabry-Perot fringes associated with each point. It is possible to show in this case (for a one-dimensional calculation) (Ref. [2.2.13]) that